Advances in plasmon ruler assembly reveal complex dynamics between conformational states of HSP90

Dissertation
zur Erlangung des Grades
"Doktor der Naturwissenschaften"
im Promotionsfach Chemie

am Fachbereich Chemie, Pharmazie und Geowissenschaften
der Johannes Gutenberg-Universität
in Mainz

Bastian Ernst Michael Flietel
geb. in Wiesbaden 24. Juli 1994

Mainz, den 15. Februar 2024

D77

1. Berichterstatter: [redacted]
2. Berichterstatter: [redacted]
Tag der mündlichen Prüfung: 5. April 2024

Eidesstattliche Erklärung

Die vorliegende Arbeit wurde im Zeitraum von September 2019 bis Februar 2024 in der ‚Nanaobiotechnology Group' von Prof. Dr. Carsten Sönnichsen am Department Chemie der Johannes Gutenberg-Universität Mainz durchgeführt. Ich versichere, dass ich die vorliegende Arbeit selbstständig und ohne fremde Hilfe verfasst, andere als die angegeben Quellen nicht benutzt und die den Quellen wörtlich und inhaltlich entnommenen Stellen als solche kenntlich gemacht habe. Ich versichere, dass ich diese Dissertation bisher weder im In- noch im Ausland schriftlich oder in elektronischer Form als Prüfungsarbeit einer Gutachter*in vorgelegt habe.

_____

Bastian Flietel

Jeder Umweg erhöht die Ortskenntnis.

Unbekannt

Abstract

Plasmon rulers can be used to record dynamic processes of bio-molecules over long time scales. A plasmon ruler consist of two noble metal nanoparticles and show exponential scaling of their resonance wavelength and scattering intensity with the distance between both particles. This enables the measurement of small distance changes between the particles. Nanoparticles do not suffer from bleaching or blinking and therefore allow for theoretically infinitely long measurements. The potential of this technique has been demonstrated by recording the conformational changes of the HSP90 protein over $24\,\mathrm{h}$. The long experimental time revealed a previously unknown long decay time and showed that the HSP90 protein can remain in one conformation for hours at a time. This raised new questions, as the recorded time series showed signs of ergodicity breaking on the $24\,\mathrm{h}$ time scale. However, the yield of plasmon rulers and time consuming synthesis did not allow further studies of the raised questions.
Here, I show the advancements made in use of plasmon rulers for the recording of protein dynamics on a single molecule level by increasing the yield and simplifying the synthesis.
I showed that the solid phase synthesis of plasmon rulers in a flowcell only yields singular plasmon rulers, which is too low for systematic improvements. The required glass passivation for this methods provided challenges, which I addressed by testing different reaction protocols. However, none of those methods met the constraints for the experiments with plasmon rulers. To overcome these challenges, I have developed a batch synthesis method which results in an order of magnitude higher plasmon rulers without the need for a passivated glass surface. I show that HSP90 does not only fluctuate between the known two states, but sometimes also between three or more distinct states. My evaluation of the dwell times for the known two states expands the model of decay channels by two decay channels.
This thesis highlights the strength of plasmon rulers in probing of protein conformations over a high dynamic range and sample size and expands the knowledge of HSP90 conformations and decay channels.

ABSTRACT

Zusammenfassung

Mit Plasmonenlinealen lassen sich dynamische Prozesse von einzelnen Biomolekülen untersuchen. Ein Plasmonenlineal besteht aus zwei Edelmetall-Nanopartikeln und zeigt eine exponentielle Skalierung ihrer Resonanzwellenlänge und Streuintensität mit dem Abstand zwischen den Partikeln. Dies ermöglicht die Messung von kleinen Abstandsänderungen zwischen den Teilchen. Da die Nanopartikel nicht ausbleichen, ermöglichen sie theoretisch unendlich lange Messungen. Das Potenzial dieser Technik wurde durch die Aufzeichnung der Konformationsänderungen des HSP90-Proteins über 24 Stunden demonstriert. Die lange Versuchsdauer enthüllte bisher unbekannte lange Abklingzeit sowie, dass das HSP90-Protein stundenlang in einer Konformation bleiben kann. Dies warf neue Fragen auf, da die aufgezeichneten Zeitreihen Anzeichen eines Ergodizitätsbruchs auf der $24\,\mathrm{h}$-Zeitskala zeigten. Die Ausbeute an Plasmonenlinealen und die zeitaufwendige Synthese erlaubten jedoch keine weiteren Untersuchungen der aufgeworfenen Fragen.
Hier zeige ich die Fortschritte bei der Verwendung von Plasmonlinealen für die Aufzeichnung der Proteindynamik durch Erhöhung der Ausbeute und Vereinfachung der Synthese.
Ich zeige, dass die Festphasensynthese von Plasmonenlinealen in einer Flusszelle nur einzelne Plasmonenlineale ergibt, was für systematische Verbesserungen zu gering ist. Die erforderliche Glaspassivierung stellte eine Herausforderung dar, die ich durch das Testen verschiedener Reaktionsprotokolle angegangen bin. Keine dieser Methoden erfüllte jedoch die Anforderungen für die Experimente mit Plasmonlinealen. Um diese Herausforderungen zu überwinden, habe ich eine Batch-Synthesemethode entwickelt, die ohne eine passivierte Glasoberfläche zu einer um eine Größenordnung höheren Anzahl von Plasmonlinealen führt. Ich zeige, dass HSP90 nicht nur zwischen den bekannten zwei Zuständen fluktuiert, sondern manchmal auch zwischen drei oder mehr. Meine Auswertung der Verweilzeiten erweitert das Modell der Zerfallskanäle um zwei Zerfallskanäle. Diese Arbeit zeigt die Stärke von Plasmonlinealen bei der Untersuchung von Proteinkonformationen über einen hohen dynamischen Bereich und mit großen Probenumfang und erweitert das Wissen über HSP90-Konformationen und Zerfallskanäle.

Contents

CONTENTS

List of Figures

LIST OF FIGURES

List of Tables

Chapter 1

Introduction

Proteins show a wide range of functions in organisms. In DNA replication, the protein DNA-polymerease catalyzes the synthesis of new DNA strands and DNA-helixase unwinds the double helix to enable reading and replicating of the DNA [1]. Ion pump regulate the transfer of ions across a membrane in cells [2]. Other proteins generate mechanical force like, for example, myosin, which "walks" along actin strands [3, 4]. Light harvesting complexes in plants consist of multiple proteins to absorb light and transfer the absorbed energy for the use in photosynthesis. All these functions are vital for the organism and require the protein to undergo dynamic changes in its structure to fulfill its task. The structure of proteins is accessible by X-ray crystallography and cryo-electron microscopy but those techniques deliver a static image [5]. Observing protein dynamics experimentally is challenging. Techniques like NMR spectroscopy are able to map the chemical environment of each atom in a protein and therefore differentiate between different conformations. However this method operates not on a single molecule level and averages over the ensemble of many proteins in the sample. This gives detailed information over the relative population of each state but not on the sequence of states [6, 7].

Several techniques have emerged to access the dynamics of single proteins at room temperature: Förster Resonance Energy Transfer (FRET), single molecule force spectroscopy (atomic force microscopy, magnetic and optical tweezers), electrical nanopores and plasmon rulers[1]. All these techniques are able to resolve protein dynamics over different orders of magnitude in time.

In 2018, our group has used plasmon rulers to investigate the dynamics of the yeast HSP90 protein and found previously unknown, long dwell times, not accessible by other techniques [8]. However, the reported yield of functional plasmon rulers was too low to gather data for further investigations of protein dynamics on long timescales. Therefore, I worked on

[1] A protein connected by two nanoparticles

improvements of the plasmon ruler technique regarding reliability of the synthesis and yield of plasmon rulers.

In chapter one, I present an overview over competing single molecule techniques for the investigation of protein dynamics.

Chapter two gives an introduction on the theory of plasmon creation and plasmonic coupling for plasmon ruler experiments and gives an overview over the state of the art.

In chapter three, I show theoretical considerations for the synthesis of plasmon rulers for the investigation of single protein dynamics. I discuss different reaction strategies: a synthesis in the microfluidic flowcell, where one particle is fixated on the surface (solid phase synthesis) and a batch synthesis where both particles are freely diffusing. For both cases I show different possibilities of reactivity for the used particles with the resulting advantages and challenges. For both, solid phase and batch synthesis I show an estimation of reaction times to form plasmon rulers.

Chapter four shows the results of repeating the solid phase synthesis protocol used in the publication from our group [8]. I explain encountered challenges and tested improvements to the protocol and explain the resulting research topics.

In chapter five I explain the surface passivation that is needed in the solid phase synthesis. I compare reported passivation protocols from the literature and present reported challenges in the silanization of glass. For the use in plasmon ruler experiments I define three constraints which have to be met for a passivated surface to be usable in further experiments, and compare three different procedures for silanization. However, none of the investigated procedures meets all formulated constraints.

Chapter six covers the experimental results from a new batch synthesis for HSP90 plasmon ruler that I developed. I explain the reaction protocol and its advantages. The yield of single protein plasmon rulers reached a maximum of 10% (calculated relative to all particles in the field of view), but varies between experiments. The resulting time series show more than the expected two states known from previous experiments, as well as additional decay channels.

In chapter seven I explain the software I developed and improved for the investigation of large amounts of HSP90 time series from plasmon ruler experiments.

Chapter eight summarizes the results of my thesis and gives an outlook on ongoing challenges for the use of single protein plasmon rulers.

1.1 Single molecule techniques have different limitations

The dynamic processes of proteins happen over a multitude of time scales depending on the process and movement involved [3, 9–13]. While collective domain movements in proteins[2] are slower compared to side chain rotation, even a single process can happen over long timescales until completed (refer to figure 1.1 for an overview over timescales for different dynamic processes).

Because of the different timescales and distances on which the dynamics of proteins happen different single molecule techniques have been developed for their investigation. These techniques include Förster resonance energy transfer (FRET), different force microscopy techniques like optical tweezers, nanopores and plasmon rulers. In this thesis I worked with plasmon rulers because of the long continuous observation time they enable. The following chapter briefly introduced each technique and compares advantages and disadvantages of each technique.

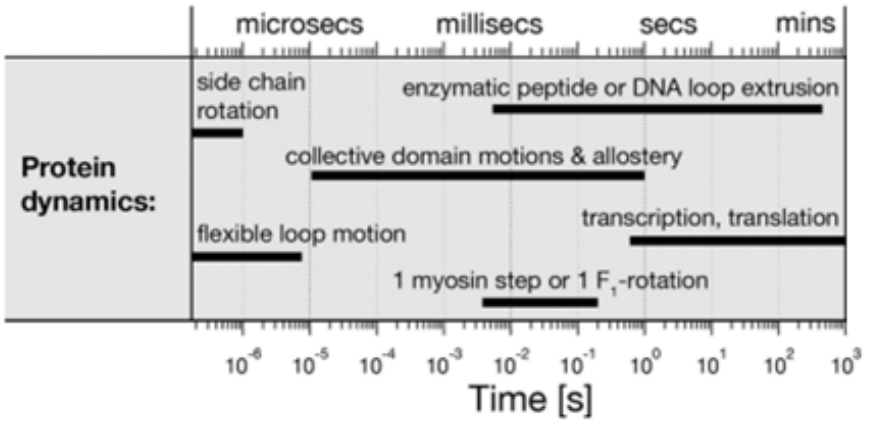

Figure 1.1: Examples of protein dynamics [9–11] controlling function [3, 12, 13] occurring in the microsecond to minutes range. Adapted with permission from [7]

1.1.1 Förster resonance energy transfer

Förster resonance energy transfer (FRET) uses (at least) two fluorescent dyes to investigate conformational changes in proteins. Labeling proteins with fluorescent dyes requires purification steps but can be done with nearly

[2] Protein domains are stable subunits of proteins.

100% efficiency per dye. Using a confocal microscope, the molecule is illuminated by a laser with the excitation wavelength of the donor dye. The fluorescent light is split using a dichroitic mirror into the fluorescence of donor and acceptor [7, 14, 15].

If the dyes are far apart only fluorescence of the donor is recorded (see figure 1.2 green line in graph). Once the protein changes its conformation the dyes get moved closer together and an non-radiative energy transfer can happen. The transferred energy is emitted by the donor and seen as fluorescence (figure 1.2 red line in graph). The ratio between donor and aceptor fluorescence is called FRET efficiency. This efficiency of the energy transfer depends on the distance and orientation of the dyes to each other, which decays with r^{-6} and therefore makes FRET highly sensitive to distance changes. On the other hand, it limits the observation range to approximately $10\,\mathrm{nm}$ between the dyes [16]. Because fluorescent dyes undergo bleaching during the experiment it is required either to measure with a longer waiting time between data points or sacrificing total experimental duration [17]. Both cases limit the accessible timescale of protein and require the recording and averaging over multiple single proteins for a complete picture of conformational states of the protein. Lastly, the signal to noise ratio in FRET experiments is generally low because of the low signal produced by single fluorescent dyes [17].

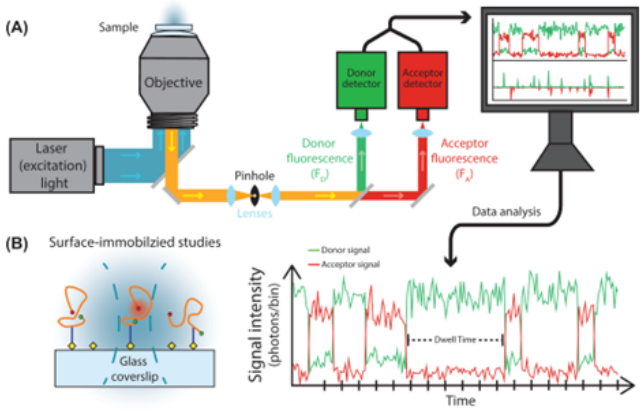

Figure 1.2: A) Schematic overview of a single molecule confocal fluorescence microscope. Path of incident light in teal, combined signal of the sample in yellow and donor and acceptor in green and red. B) Left: Schematic of surface-immobilized FRET experiments. Red dot is the acceptor which lights up when the donor (green dot) is close enough for energy transfer.Right: Schematic of donor- (green) and acceptor signal (red) over time. Horizontal dashed line corresponds to individual dwell time of one conformation. Reprinted with permission from [18]

1.1.2 Force spectroscopy

Force spectroscopy encompasses three different techniques: atomic force microscopy (AFM), magnetic tweezers and optical tweezers. In all three techniques, the probe molecule is fixated between a probe and a fixed point. For optical tweezers, both probe and fixed point are dielectric beads, that are trapped in the focus of a laser (refer to figure 1.3 a). Magnetic tweezers fixate the molecule between a surface and a magnetic bead (figure 1.3 right). In AFM the protein is fixated between a surface and the tip of the cantilever. The extension or dynamics of the molecule is derived from the position of the probe relative to the surface or fixed bead [14]. Because of the applied force to the molecule, these techniques do not operated under equilibrium conditions.

Optical tweezers can operate with particles ranging from nanometer to micrometer size and measure the three dimensional displacement of the trapped particles with an accuracy in the sub-nanometer regime at a sub-millisecond time resolution [14]. The drawback of optical tweezers is potential heating of the probe and surrounding medium due to the laser. This can influence for example enzymatic activity, change the local viscosity and might cause convections that in turn affect the measurement. Additionally, optical trapping is not selective. Any dielectric particle can be trapped by the laser, which requires low concentrations and highly purified samples to exclude sources of interference [14].

For magnetic tweezers, the displacement is traced by video which makes this technique less error prone in inhomogeneous environments like cells where the optical traction of optical tweezers would not work properly [14]. On the other hand, the video based tracking has a limited bandwidth and limits the direct measurement of very fast and small displacements. Drift is another challenge in all force spectroscopy techniques. A increase in temperature of $1\,^{\circ}\mathrm{C}$ can cause an expansion of more than one hundred nanometers. Since the distance changes in protein dynamics are in the range of nanometers, drift caused by small temperature fluctuations can cause artifacts or hinder total experimental time. [14]

1.1.3 Nanopores

Nanopores are, as the name suggests, nanometer sized holes within a membrane which can't be permeated by the analyte. Depending on the experiment and type of nanopore the diameter ranges from sub-nanometer to multiples of tens of nanometers (see figure 1.4 a). There are two types of nanopores: the biological and solid state nanopore. The biological nanopore is a protein in a lipid membrane like in an ion channel of a cell for example, while the solid state nanopore is a hole inside an insulating membrane. Once a voltage is applied between both sides of the membrane an ionic current flows through the pore. If an analyte moves through the pore it partially blocks the ionic current which is read out as a change in the ionic

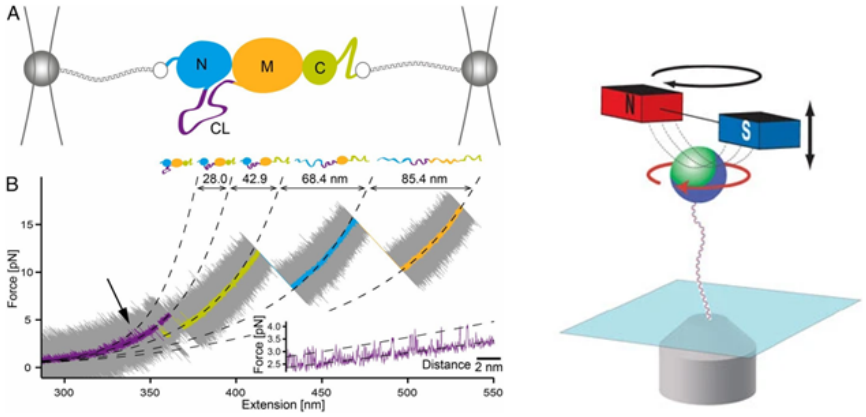

Figure 1.3: a) Schematic overview over experimental setup of optical tweezer experiment with HSP90 (not to scale, N-terminal domain blue, middle domain yellow, C-terminal domain green). Monomeric HSP was linked to two spheres which are trapped by lasers to measure and apply force to the molecule. b) A typical force–extension trace at constant velocity (here, 10 nm/s) shows the successive unfolding of HSP90's three domains as large peaks c) Cartoon depicting the layout of magnetic tweezers based on permanent magnets. A super-paramagnetic bead (green) is attached to the surface of the trapping chamber by a single molecule of DNA. A pair of small permanent magnets (red and blue) above the trapping chamber produces a magnetic field gradient (dashed lines) along the axial direction, which results in a force on the bead directed up toward the magnets. The force is controlled by moving the magnets in the axial direction (bidirectional arrow). Rotation of the magnets (black circular arrow) produces rotation of the magnetic bead (red circular arrow) with a one-to-one correspondence. A microscope objective (gray) images the bead onto a CCD camera for real-time position tracking. *Reproduced with permission from Springer Nature from [14]* .

.

current. How large the change is depends on the size and orientation of the analyte inside the nanopore. The dwell time (time spent in the nanopore) is given by the duration of the change in ionic current (see figure 1.4 c).

Nanopores offer a method to study single molecule dynamics without the need for labeling (e.g. attaching a fluorophor) of the analyte because the molecule freely diffuses in and out of the nanopore. This on the other hand offers no information about the orientation of the molecule inside the pore. Therefore additional experiments with changes in cofactors or nucleotides are necessary to match observed dynamics with functional states of a protein [7].

Because of the free diffusion, the observation time for each event is

limited by the time the protein remains inside the nanopore. For longer observation times on a single protein one needs to introduce a binding site to fixate the protein inside the pore. While this increases the time of investigation it also counteracts the label free claim for nanopores.

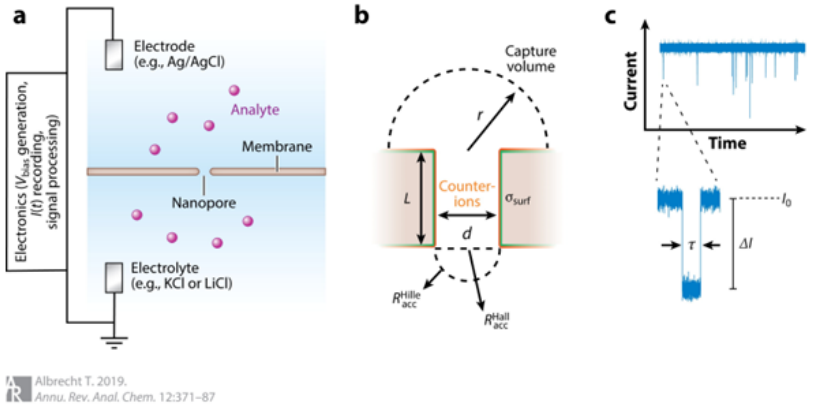

Figure 1.4: a) Basic design of a nanopore sensor. The nanopore allows for the transport of liquid, ions, and analyte (purple spheres) between the compartments. b) Close-up of the pore region, here with cylindrical geometry with diameter d and length L indicated. The charge of membrane surface (green) is balanced by counterions in solution (orange). Above the pore: hemispherical capture volume of radius r; below the pore: integration limits for R_{acc}^{Hille} and R_{acc}^{Hall}. c) Illustration of an I(t) trace, obtained at constant V_{bias}. Downward spikes correspond to translocation events. (Inset) Some key parameters, including the event duration τ, amplitude ΔI, and open-pore current I_0. Reprinted with permission from [19].

1.1.4 Plasmon Ruler

Plasmon rulers consist of two noble metal nanoparticles with a distance of less than the particle diameter. In this distance regime the resonance wavelength and scattering intensity scale exponentially with the distance between the nanoparticles and can therefore be used for distance measurements [20, 21] (for more details see chapter 2). Since these nanoparticles do not undergo bleaching the experimental time is in theory unlimited and due to the high intensity of the scattered light the signal to noise ratio is an order of magnitude larger than in FRET experiments which was shown by the recording of the conformational changes of HSP90 over $24\,\mathrm{h}$ by Laura Tüting and Weixiang Ye in our group [8, 22]. Disadvantages for plasmon rulers are large particles compared to the protein. The bigger the particle, the larger the distance that can be investigated. To work in a force free

environment where no external force is applied to the protein, the particle size has to be adapted to the experimental conditions. The balance between attractive and repulsive forces between nanoparticles is influenced by their size and the concentration of salt around them. Larger particles and higher salt concentrations cause attractive forces to dominate at larger distances between the particles and therefore lower the minimal working distance of plasmon rulers. The synthesis of plasmon rulers is an other challenge. Since functionalized nanoparticles have more than one binding site, they can't be used in the same access like for example fluorecent dyes. This could cause multiple binding events which counteracts the single molecule experiment (for more details on considerations for the synthesis of plasmon rulers see chapter 3. Lastly plasmon rulers require linking of the protein to a functionalized nanoparticle as direct contact of proteins with the surface of the nanoparticles can lead to denaturation and would make the recording of dynamics impossible [23].

1.2 Conclusion

The different methods have different advantages and disadvantages. Depending on the movement and dynamic range to be investigated in single proteins each presented technique has advantages and disadvantages (see figure 1.5).

FRET is limited in the signal to noise ratio and duration of the measurements. But the known position of the labels allows for direct information gathering over a certain reaction coordinate.

Force spectroscopy does not operate under equilibrium conditions because of the applied force. On the other hand, it enables forced denaturation (and observation of the refolding) and optical tweezers can track movement in three dimensions with the downside of potential photodamage and probe heating due to the used laser.

Nanopores can determine different protein conformations without labeling of the protein by the change in ion current through the pore that is partially blocked by the protein. In turn the observation of an event can't directly be linked to a conformation or conformational change of the protein because of the random orientation in the pore.

Plasmon rulers can in theory infinitely observe protein dynamics with a large signal to noise ratio enabling the observation of dynamics of a large dynamic range. The preparation of those plasmon rulers is on the other hand complicated and less controlled than linking fluorescent dyes to a protein because the nanoparticles can have more than one binding site. This is because of the needed functionalization of particles to avoid denaturation on direct contact of the protein with the particle surface.

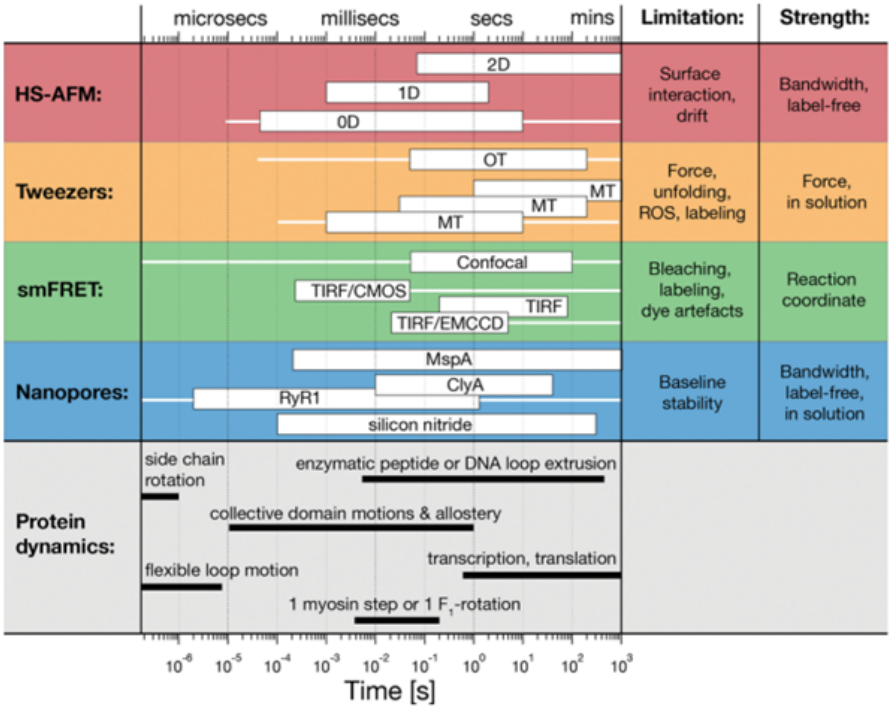

Figure 1.5: Single molecule techniques cover different timescales. White boxes represent experiments reported in the literature, thin white lines indicate the technical detector bandwidth: High-speed AFM (HS-AFM) in 2D imaging mode, 1D line scans, or 0D 'on-spot' detection, as indicated [24]. Optical (OT) [12, 25] and magnetic tweezers (MT) [26–30] probing protein function (not unfolding, ROS: reactive oxygen species). Surface immobilized smFRET in confocal [31], or TIRF mode with CMOS [32] or EMCCD [7] detectors. Protein [33–35] and solid-state nanopores. Examples of protein dynamics [9–11] controlling function [3, 12, 13] occurring in the microsecond to minutes range. Faster dynamics, as well as ensemble studies and mechanical unfolding experiments are not considered in this figure. Reprinted with permission from [7]

.

Chapter 2

Plasmon Theory

When light meets a noble metal nanoparticle the conduction band electrons are excited to harmonic oscillation with the electric field of the electromagnetic wave (figure 2.1 a). The positively charged cores remain in place as an approximation (quasi static approximation), acting as a restoring force to the displaces electrons. The collective oscillation of the conduction band electrons is called "plasmon" and the nanoparticles with those properties "plasmonic nanoparticles". For each particle a specific resonance wavelength exists at which the absorption and scattering of light reach its maximum. The resonance wavelength is influenced by the material of the nanoparticle, its size and shape as well as its environment.

For experiments on a single particle level, darkfield microscopy is commonly used. Figure 2.1 b) shows a sketch of a darkfield microscope. The incident light is shaped by the darkfield condensor in a hollow cone and is not collected by the objective. Because light is scattered by the nanoparticles in all directions, the scattered light is collected by the objective and can be viewed by eye or camera. The result are bright spots on a dark background.

2.1 Non bleaching single particles as sensors

If a polarizable object comes close to a plasmonic nanoparticle the object gets polarized by the electric field around the particle. Since the polarization is opposite to the field around the particle, the electric field around the nanoparticle gets weakened (see figure 2.1 c). Therefore the restoring force needed is lower and the resonance wavelength get shifted to lower energies meaning higher wavelengths (called red shift). Because of this environmental sensitivity plasmonic nanoparticles have been used for different sensing applications. Examples are the determination of affinity constants [36], in vivo sensing [37]

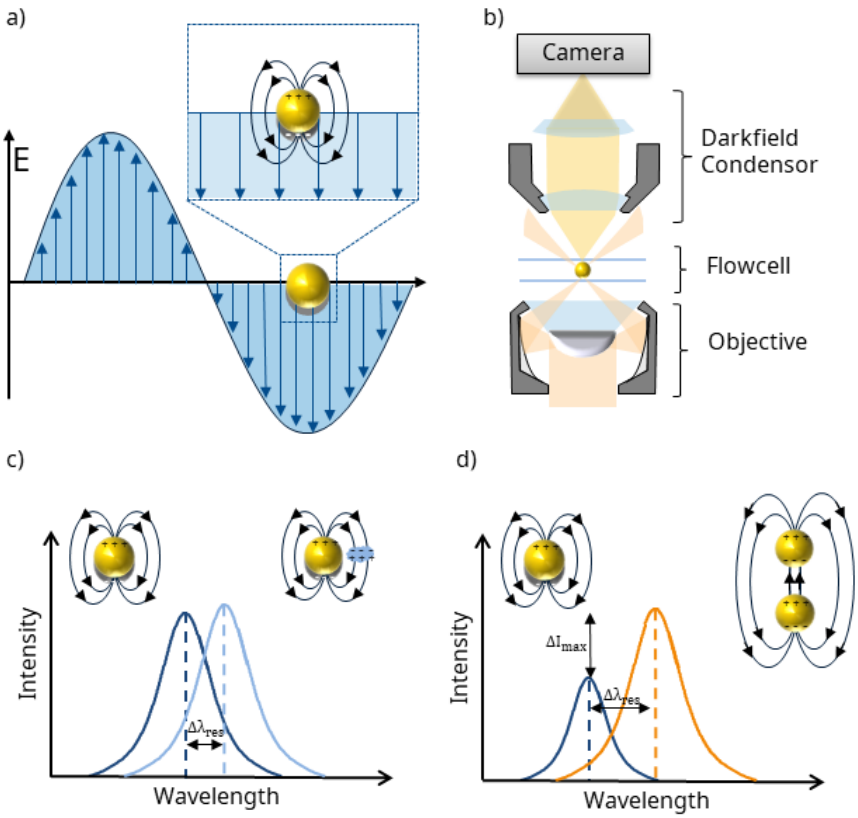

Figure 2.1: a) Schematic creation of a particle plasmon. On interaction with the electrical field (blue) the conduction band electrons (grey) of the nanoparticle are displaces, resulting in charge separation. b) Sketch of the light path in the darkfield microscope. The incident light (orange) is focused in a hollow cone on the probe. The scattered light is collected by the objective and directed to the camera while the incident light is not. Components not to scale. c) Resonance wavelength changes with environment of the nanoparticle. Sketch of plasmonic nanoparticle interaction with polarizable objects in its close environment. The electric field around the nano particle polarizes the object (blue cloud), causing a damping of the field d) Sketch of plasmon hybridization When two plasmonic nanoparticles come close to each other the scattering intensity increases and the resonance wavelength shifts towards higher values (orange) compared to singular nanoparticles (blue)

2.2 Coupling of plasmons is distance dependent

If the object in proximity is another plasmonic nanoparticle and the distance is small enough (smaller than the diameter of the nanoparticles) the dipoles of the particles couple (see figure 2.1 d). With decreasing distance between the particles the resonance wavelength red shifts and the scattering intensity increases [38, 39] The distance dependency of the plasmon coupling has been studied with lithographic discs of different sizes and distances [40]. Figure 2.2 a) shows the relative change in the resonance wavelength against the distance of the discs normalized to the disc diameter. The exponential scaling applies for all tested sized of the discs. Similarly the scaling was probes for spherical nanoparticles [38]. The distance was controlled by different length of complementary DNA stands and showed an exponential scaling behaviour (see figure 2.2 b).

2.3 Signal can be read out spectraly or using a single wavelength

The readout of the signal typically is done by recording the scattering spectrum of the plasmon rulers and monitoring changes in the resonance position [21, 22, 41, 42]. This can be done on a single particle level or over a full field of view by using hyper spectral imaging[1] [43]. This enables the recording of multiple hundred single particle spectra at the same time. Using the spectral information of the resonance wavelength limits the use of plasmon rulers in fast dynamic processes, because the time resolution is limited by the number of data points needed in the recording of the scattering spectrum.

The use of a single wavelength for the determination of spectral changes in the plasmon resonance was shown in our group by Sirin Celiksoy [44]. Figure 2.2 c) shows a sketch of the measurement principle for the recording of HSP90 plasmon ruler signals. Upon changing its conformation and therefor the distance between the particles the plasmon resonance changes. The red shift upon lowering the distance between the particles results in an maximum change in scattering intensity when looking at the spectral position of the resonance plus half of the full width at half maximum (FWHM) $\lambda_{res} + \frac{1}{2}FWHM$.

[1] In hyper spectral imaging a series of images is taken, each at a single wavelength of illumination. If the location of the nanoparticles is known, the scattering spectrum can be calculated from the intensities of the particle in each image.

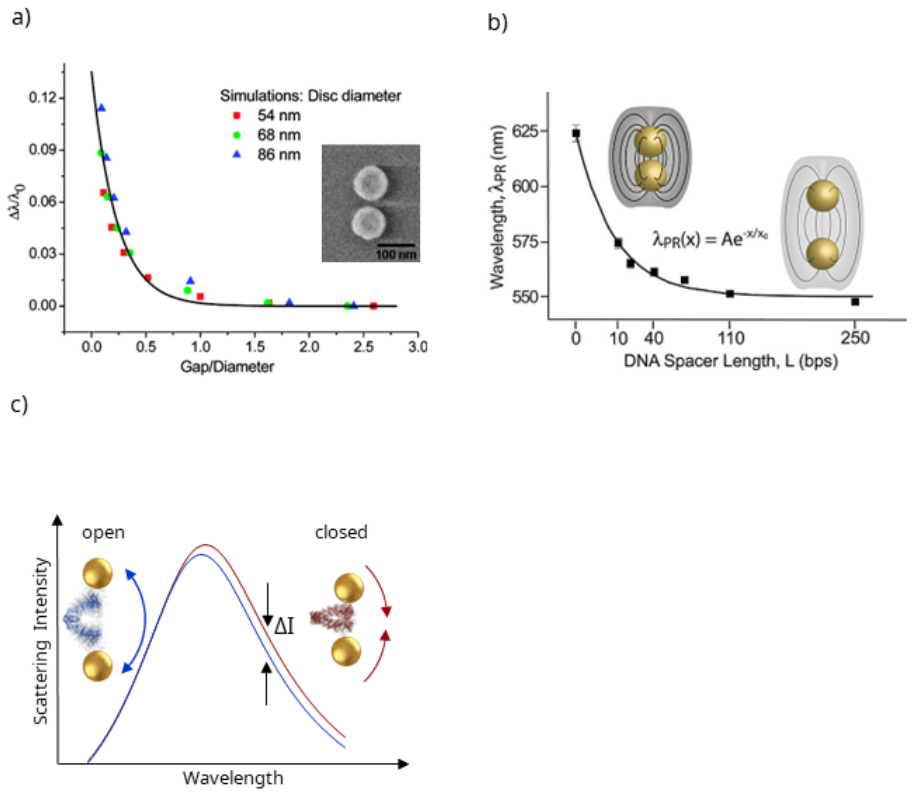

Figure 2.2: a) Exponential scaling of relative resonance shift with distance of two nano disks. Colors and symbols indicate different disk diameter, inset shows an example SEM image of the disks. *Reprinted and adapted with permission from [40]. Copyright 2024 American Chemical Society*. b) Resonance of nanosphere dimers against the length of the used DNA spacers, showing exponential scaling with distance like the disks in a) *Reprinted and adapted with permission from [38]. Copyright 2024 American Chemical Society*. c) Sketch of the intensity change with opening and closing the HSP90 protein. Resonance position and total intensity for two spheres connected by HSP90. Switching from open (blue) to closed (red) conformation causes small shift of resonance toward longer wavelength and increase in intensity. Because the intensity increase is asymmetrical, the intensity change at ca. λ_{res} + 0.5 full width at halt maximum (FWHM) can be measured as a signal for distance changes. Figure c was reproduces with permission from [8].

2.4 Plasmon rulers in sensing applications

The photostability and versatile functionalizaton have resulted in the use of plasmonic nanoparticles and plasmon rulers in multiple sensing applications. Especially the large increase in scattering intensity upon dimerization is used for the detection of dynamic processes or analyte concentration.

2.4.1 Strong signal upon dimerization used for signal

Jun et. al. used plasmon rulers to investigate enzyme activation in live cell. They bound multiple nanoparticles around one core particle and monitored the cleavage of the linker molecule by the protein caspase-3[2]. With each cleavage, one less particle is bound which resulted in a blue shift of the resonance wavelength and lower scattering intensity. The long observation time of plasmonic nanoparticles allowed for the continuous monitoring of the protein activity and observing early-stage caspase-3 activation, which was not possibly by other single molecule methods. [42]

The distance dependency of the resonance wavelength and scattering intensity was used by *Nan et. al.* to fabricate a micro array chip for the detection of SARS-CoV-2 variants. For this device they printed antigens on a gold coated microscopy slide. They then incubated this slide with the sample of virus variants, washed the slides and covered the surface with gold nano particles. In places where the antigen bound the corresponding antibody, the distance of the nanoparticle to the gold surface is larger than in spots where no antibody was bound. This results in visible differences between the spots and allowed for a visuals detection of different variants by eye. [45]

Yadav et. al. used gold nanospheres in shape-memory polymer films to monitor structural changes of the polymer during stretching. They found that stretching the doped polymer film resulted in changes in the optical properties along the stretching direction which resulted from distance changes between the gold nanoparticles. Investigation of the polarization dependency allowed for structural insight on the nanoscale of the polymer during stretching and recovery to the original shape. [46]

Plasmon rulers were used by *Wang et. al.* to investigate the dimerization of single receptors on a cell membrane. They used a three component system which consist of monomer a, monomer b and a funtionalized gold nanoparticle. Monomer a is functionalized with a single stranded DNA that carries a nanoparticle that serves as the recognition element. Monomer b modified with a single stranded DNA to assist the DNA hybridization. The nanoparticle is functionalized with a complementary single stranded DNA

[2] Caspases are a family of proteins which play a role in the programmed cell death.

and induces the dimerization of the membrane proteins by DNA hybridization. The long observation time of gold nanoparticles allowed tracking of the diffusion of the membrane protein and monitoring the dimerization process. [47]

2.4.2 Distance changes used as signal

The long observation time and distance dependency was used by our group by Laura Tüting and Weixiang Ye to investigate the dynamics of the protein HSP90 [8, 48]. HSP90 changes its conformation between an open and a closed conformation in a scissor motion at room temperature without the additional energy from ATP hydrolysis. The plasmon ruler was constructed by binding one particle to a functionalized glass surface via biotin-streptavidin in a microfluidic cell. Then each component is flushed in for the reaction one at a time to suppress side reaction and ensure single protein plasmon rulers (see figure 2.3 a). With the changes is the conformation of the HSP90 protein, the distance between the gold nanoparticles is changed. Due to the exponential scaling of the coupling of the plasmons this causes a change of ca. 10% in the scattering intensity (see figure 2.1 c and figure 2.3 c). Their experiments shows that HSP90 can remain in one conformation for minutes and sometimes hours (figure 2.3 b) which was not known before.
These newly found long dwell times expanded the model which previously used two decay channels to describe the transitions to three decay channels.

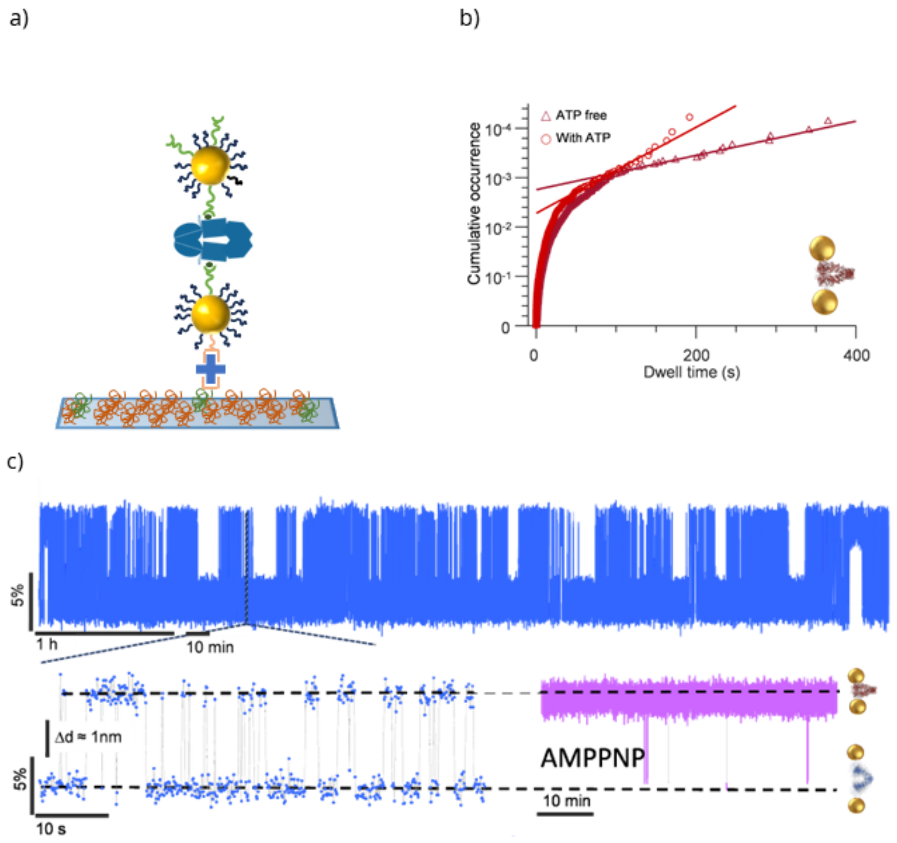

Figure 2.3: Plasmon rulers for single molecule dynamics. A: Sketch of the HSP90 plasmon ruler on a functionalized surface. The plasmon ruler is bound to the surface via biotin-streptavidin (plus). Both particles are functionalized to bind to HSP90 (blue). The distance between the nanoparticles changes due to the conformational changes of the HSP90. B: Cumulative histogram of the dwell times of HSP90 in the closed conformation. The higher the y value in this plot the rarer the dwell time. The occurrence of the long dwell times was influenced by the addition of ATP. C: example time series of a HSP90 plasmon ruler, which shows the typical fluctuation between two states. The fluctuation stopped after the addition of AMP-PNP which locks HSP90 in the closed conformation (pink).This figure was adapted with permission from from [8], Copyright 2024 American Chemical Society.

Chapter 3

Synthesis design: flowcell vs batch

Forming constructs of exactly two nanoparticles connected by a single molecule (in this thesis referred to as "plasmon ruler") requires a balance in reactivity of the two reaction partners. If both are low in their reactivity, it will require long reaction times to form the connection. On the other side too high reactivity can lead to the formation of multiple bonds either between the two nanoparticles or to more than one particle. To control the reaction, single molecule plasmon rulers have been prepared in a solid phase synthesis [20, 38] akin to the Merrifield synthesis for peptides [49]. The reactant is bound to a solid phase and after each reaction step purified by flushing out unreacted species. This procedure allows for complete purification after each reaction step and therefore disfavours side reactions caused by residues of reactants. An alternative to the solid phase synthesis is the synthesis of plasmon rulers in solution (in this chapter referred to as batch synthesis). In this method the dimers are freely diffusing and have to be hindered to further reacts after two particles have formed a dimers. Xiong et. al. [50] and Steinigeweg et. al. [51] have encapsulated their formed dimers within a silica shell to prevent the reaction with further particles. However, this does not allow the movement of the particles and therefore prevents the recording of dynamic processes.

In this chapter I discuss advantages and disadvantages for both synthesis methods, solid phase synthesis and batch synthesis, as well as resulting challenges for the experimental setup and evaluation plasmon rulers. I present theoretical estimations on which functionalization of the nanoparticles has the highest chance for successfully forming dimer, together with an estimation for the average reaction time needed.

3.1 Solid phase synthesis of plasmon rulers

Solid phase synthesis The solid phase synthesis of plasmonic dimers works by linking one particle (preferably covalently) to the surface in a microfluidic cell. For the covalent binding of particles to the glass surface, the surface has to be functionalized prior to the plasmon ruler synthesis. The nanoparticles have to be functionalize so that one particle can bind to the surface and to the molecule that is to be investigated. The second particle has to be functionalized in a way that it binds to the molecule on the first particle but not to the surface.

In the nanobiotech group Laura Tüting [48] developed a solid state synthesis of plasmon rulers to investigate the HSP90 protein (refer to chapter 2 for more details on the previous work on plasmon rulers). She used the following generalized procedure:

- bind first particle to the surface via biotin-streptavidin
- flush unbound particles away with buffer
- flush in Succinimidyl-trans-4-(N-Maleimidylmethyl)cyclohexan-1-carboxylat (SMCC) to activate the nanoparticles for reaction with the protein
- flush unreacted SMCC away with buffer
- flush in HSP90
- flush unreacted HSP90 away with buffer
- flush in SMCC to activate the protein for reaction with the next particle
- flush unreacted SMCC away with buffer
- flush in particel for dimerization
- flush unreacted particles away

The full reaction protocoll can be found in the appendix and figure 2.3 a shows a sketch of the plasmon ruler. A key factor is that the medium surrounding the nanoparticle can be exchanged without removing the nanoparticle. This enables a stepwise reaction where a molecule that shall react with the nanoparticle (or molecules on the nanoparticle) is flushed in, incubated for certain time to complete the reaction and then flushed out. This leaves a purified nanoparticle on the surface, ready for the next reaction step.

Advantages of this method are that each step in the reaction can be monitored in the microscope. The change in resonance wavelength can be determined for every step, unspecifically adsorbed particles tracked, and deposited dirt identified. Flushing away unused reactants in each step

allows for a purification with close to no residues, largely suppressing side reactions. This makes later data evaluation easier, because unexpected signals can be potentially attributed to errors in one reaction step. Since one particle is fixated aggregation only occurs when the reactivity of the partners is too high or the reaction time is high enough that multiple reactions occur.

On the other side this reaction path requires a fixation of nanoparticles on the surface and a passivation against the deposition of particles in the dimerization step. The needed functionalization of the surface provides additional challenges (refer to chapter 5). The amount of particles on the surface needs to be low enough that each particle can be identified as a single particle, which also influences the reaction speed. As an example: The area visible in a darkfield microscope using a 40 times magnifying objective is approximately $4.4\,\mathrm{mm}^2$. Assuming a nanoparticle takes up a circular area on the surface with the same radius of the nanoparticle, placing one thousand particles on the surface for measurement (which is a typical number in experiments in our group) these particles take up a total of $1.9 \cdot 10^{-6}\mathrm{mm}^2$, which is equivalent to 0.004% of the total surface, thus making the vast majority of the hits to the surface not result in reaction.

3.2 Batch synthesis

In a reaction in solution both particles have to functionalized to be reactive towards the biomolecule, are mixed together with the biomolecule and left for reaction. After the reaction is finished the mixture can either be purified or used as a mixture for the experiments. Two cases can be made; one where both particles are identical and one where the particles are functionalized with different reactive groups. This would require the biomolecule to also have two different binding site. I will focus on the symmetrical reaction with identical nanoparticles, since the HSP90 protein I investigate has two identical bindig sites.

Advantages of this reaction path are the higher usable concentrations which leads to more contacts with other reactants and therefore to higher reaction speeds. There is also no need to passivate the surface, as the resulting mixture can be diluted to not saturate the microscopy surface.

Like in the solid phase synthesis, the nanoparticles need to be purified before the reaction with the biomolecule as residues of liker molecules can cause byproducts and thus reducing the yield of plasmon rulers. Here however, the nanoparticle are not bound to a substrate and are commonly purified by centrifugation. The purification by centrifugation won't reach the purity achieved in solid phase synthesis, which mean residues of reactants (e.g. residues of the particle functionalization or liker molecules) will remain in the particle solution and are carried over in the reaction mixture.

Potential side reactions can happen and lead to aggregation and side products making the final reaction product less predictable. This in turn complicates the interpretation of the recorded signals. This could be overcome by separating the formed dimers from the reaction mixture. Possible techniques for this are density gradient centrifugation [52], high performance liquid chromatography (HPLC) [53] and gel electrophoresis [54]. The challenge is however that the protein I want to use must retain its function after the purification. Gel electrophoresis with agarose gels uses buffer conditions with pH of 8 and causes heating of the gel during the procedure, which might denature the protein. Density gradient centrifugation could be done at room temperature with the same buffer used for preparing the sample and should be investigated in future research. The potential for purification of the resulting dimers would allow for experiments with only the wanted dimer constructs as long as the molecule to investigate remains functional after the purification.

Since the particles are not bound to a surface during the reaction, particles that have bound HSP90 but not another particle (incomplete reaction) can adhere with the protein to the surface (figure 3.1 left). Secondly if a particle has bound two proteins, it can also bind with the protein to the surface and both proteins undergo conformational change (figure 3.1 middle). The resulting distance change to the surface will also change the scattering intensity because the glass has a refractive index of ca. 1.5. The closer the particle moves towards the glass the higher is the resulting red shift of the resonance wavelength as explained in chapter 2. Additionally, if no passivation of the glass surface is used, both particles can bind to the surface and hinder the protein movement (figure 3.1 right). All of these scenarios make the interpretation of yield of the reaction and the experimentally recorded data more complicated compared to a solid phase synthesis.

3.3 Reactivity of nanoparticles is controlled by the number of reactive PEG molecules

Regardless of the dimer formation strategy the reactivity of the nanoparticles used is defined by the number of available functional groups on the particle. The functional groups are introduced to the particle by functionalizing with thiol-PEGs. The thiol groups bind to the gold surface and PEGs are available with different endgroups for further reactions. For the experiments with HSP90 amino groups were used to link the particles and the protein via SMCC (refer to chapter 2). A functional group on the particle can be inactive when it is not pointing outwards from the particle and is "stuck" inside the PEG coil.

The coverage density (and percentage of "active" groups) of PEGs deposited on the nanoparticle depends on the time of incubation and sur-

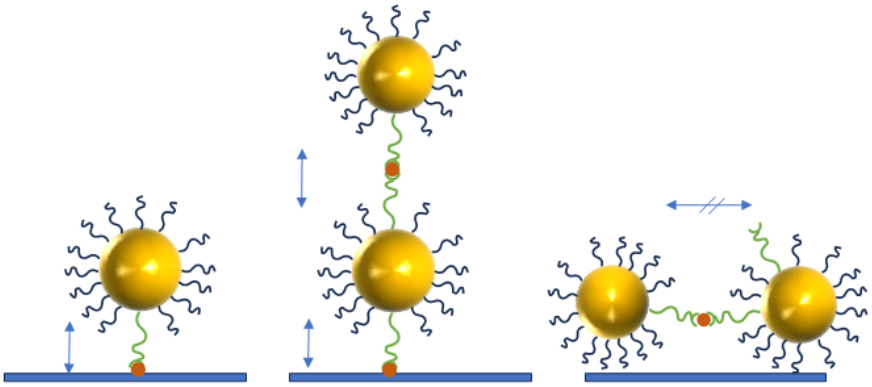

Figure 3.1: Sketches for different scenarios that can occur with batch synthesis. Blue arrows indicate distance changes. Left: Particle with HSP90 (orange dot) has not reacted with another particle and bound with HSP90 to the glass surface. The conformational change of HSP90 alters the distance of the particle to the surface. Middle: Plasmon ruler formed but the particle on the surface carries a second unreacted HSP that bound to the surface. The formed plasmon ruler is moved against the surface and the particles simultaniously against each other by HSP90. Right: A correctly formed plasmon ruler bound with both particles to the surface, hindering the conformational change of HSP90.

factent[1] that was used during the nanoparticle synthesis and is exchanged during PEGylation with thiol-PEG. For the synthesis of gold nanospheres (here referred to as gold nanoparticles) Cetrimonium chloride (CTAC) is used. In the functionaliztion of those particles with SH-PEG-NH_2 approximately 50% of those amino groups are reactive toward other molecules after the functionalization as the other half of the amino groups is stuck in the PEG coil [55].

To control the dimer formation so that exactly two particles react with one biomolecule, the functionalization of the particles has to be tuned to suppress reaction with subsequent particles and linking via multiple biomolecules. One way to controll the reaction is to use a low amount of bindig sites (ideally one) on the nanoparticles (for further discussions on reaction controll see the next section). If a mixture of PEGs (reactive and unreactive) is used to introduce different functionalities, on average the nanoparticles will have the same ratio of PEGs on its surface as was used in the mixture. But on an individual level the number of PEGs for each type are determined by the random process of binding the PEG chains. If it is assumed that each binding event is independent of the previous ones, this process is described by Poisson statistics:

[1] Substances used to stabilize the particles formed in the synthesis of the nanoparticles.

$$P_\lambda(k) = \frac{\lambda^k}{k!} e^{-\lambda} \tag{3.1}$$

P gives the propability to encounter a particle with k PEG as a given type with an average number of PEGs λ over the whole sample.

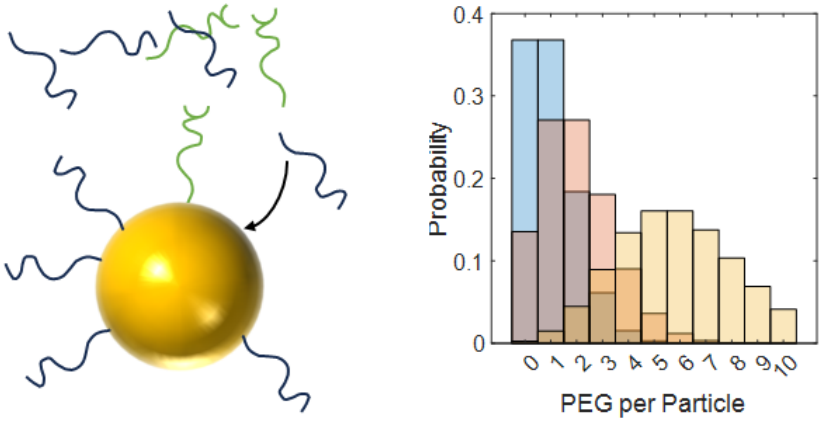

Figure 3.2: Left: Sketch of polyethylene glycoles (PEGs) with different functional groups attaching to a gold nanoparticle in a random manner. Right: Probability to encounter a particle with a certain number of PEGs with a functional group x for different averages (λ) described by poission distribution. Blue for an average of one PEG with the functional group x per particle, orange for two and yellow for six on average.

This means that for an average of one amino PEG molecule per particles , 38% of all particles actually have exactly one, while another 38% have none and ca. 18% have two (see Figure 3.2 blue bars) For higher averages the distribution broadens and changes shape to a Gaussian distribution (see Figure 3.2 yellow bars). In the synthesis of plasmon rulers this results in less control over the possibilities of formed products and reduces the predictability of yield and reaction time. To exclude the possibility of multiple binding events, one needs to separate the nanoparticles from the sample according to the number of functional groups. This could be done for example with HPLC [53].

3.4 Flowcell synthesis: challenges in design

For a solid state synthesis there are two differently functionalized particles that need to be used. One particle is functionalized with groups to anchor the particle to the surface and with groups to form the connection to the other, free particle. This free particle also needs a type of group to form the

connection to the anchored particle but should not contain the anchoring group, so it can't bind to the surface as well. For the different possible amounts of functional groups to connect the particles there are three cases that will be discussed in the following.

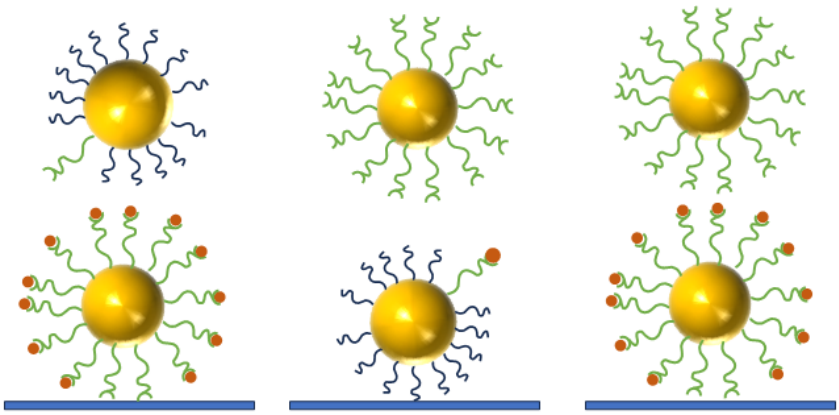

Figure 3.3: Left: Particle on the surface is fully reactive and saturated with HSP90 (orange dots). The free particle has minimal (one group) reactivity. Middle: The particle on the surface has minimal reactivity and carries only one HSP90, the free particle has maximum reactivity. Right: Example for equal reactivity where both particle are covered in reactive groups. Binding groups to the glass are not shown for visual clarity.

Case one: the particle anchored to the surface has a high reactivity and the free particle has a low reactivity (see left on figure 3.3). To have the maximum reactivity on the anchored particle the number of anchoring groups should be reduced to a minimum, which might slow binding to the surface, but the anchored particle is reactive at all sides. The challenge here is that the second particle has a small amount of binding sites. Laura Tüting calculated the time spent in a reaction shell that matches the distance to form a covalent bond to be $10^{-10}\mathrm{s}$ in her thesis [48]. The rotational diffusion time is calculated by $\tau_{rot} = d^3 \cdot \frac{\eta\pi}{6k_bT}$ which for a particle with a diameter d of $48\,\mathrm{nm}$ and with the dynamic viscosity $\eta_{water} = 0.89\,\mathrm{Pa\,s}$ at room temperate gives $\tau_{rot} = 1.4 \cdot 10^{-5}s$. This is five orders of magnitude slower than the time spent in the needed distance to form a covalent bond. Therefore it can't be assumed that the free particles rotate fast so that each encounter in the reaction shell leads to the formation of a covalent bond. The reaction time for this case might therefore be slow as multiple hits are needed to form the particle dimers.

Case two: The anchored particle has a low amount of groups to link to the free particle and the free particle has a full coverage with groups to form

the bond (see middle on figure 3.3). A positive aspect compared to case one is that, since the anchored particle carries a low number of proteins, the chance for bridging particles with multiple proteins is low. Also the rotational diffusion of the free particle does not matter (as much) for the reaction. So the majority of hits between an anchored particle and a free particle should form a dimer, as long as the free particle hits the anchored particle where the reactive group is located. Since the particle with the low amount of binding sites is fixed, it can't rotate. Therefore the orientation determines if a reaction happens or can't happen. If for example the binding site is not reachable, this particle can never form a dimer. This means for this second case the reaction time to form dimers is lower compared to case one, but the yield is also lower as not all particles can form dimers depending on its orientation on the surface.

Case three: Both particles have the same reactivity which can be divided into the subcases of a) both have low reactivity and b) both having high reactivity (see right on figure 3.3). If both particles have low reactivity the chance that a bond is formed between the particles is low and the time it takes will be long. The particle on the surface has to be oriented so that the HSP90 binding site is pointing away from the surface, otherwise no reaction can happen. Then the free particle has to be oriented so that one binding site faces toward the HSP90 when hitting that particle. Both factors combined make a reaction unlikely and this combination unfavorable. If both particle are highly reactive, the particle on the glass will be carrying multiple HSP90 like in the scenario on the right in figure 3.3. Since the free particle has also multiple binding sites the particles can be connected by multiple HSP90 which is unwanted. Also one particle on the glass could bind multiple free particles which again is unwanted since the resulting signal is not resulting from a single protein. Therefore case three should not be followed.

Since one particle is fixed on the surface and another particle has to hit this particle for a reaction, the estimation of encounters over a given time period *t* can be done with equations used for the adsorption of particles to a surface [56, 57].

$$M(t) = \sqrt{\frac{D}{\pi}}(2C\sqrt{t} - \int_0^t \frac{\Phi(z)}{\sqrt{t-z}}\,dz) \tag{3.2}$$

Here *D* is the diffusion coefficient, *C* the bulk concentration, Φ the subsurface concentration, *z* the integration variable and *M* gives the number of adsorbed molecules or particles. To get the numbers of particles adsorbed to other particles on the glass surface, I multiplied with the area taken by the nanoparticles on the glass A_{np}. The right integral is a term for the desorbtion from the surface. Since I am only interested in the amount of hits between the particles, which should result in a permanent binding, I set the term for desorbtion equal to zero (red labeled particle does not desorb while hits to the surface are disregarded as seen in figure 3.4). The number

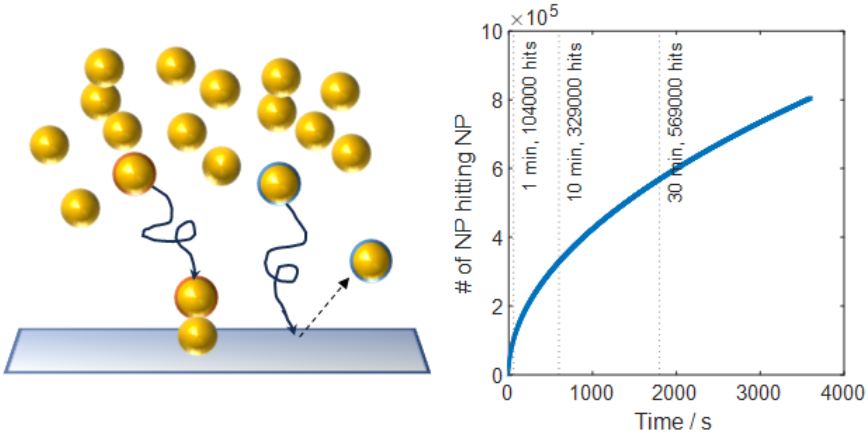

Figure 3.4: a) Estimation of flowcell reaction as diffusion to surface: Free diffusing particles can only adsorp to a fraction of the whole surface as part of the reaction with a particle on the surface (red labeled particle). All other hits with the surface don't lead to adsorption (blue labeled particle) b) Hits of nanoparticles on other (immobilized) nanoparticles on the flowcell surface over one hour for a initial particle concentration of $0.083\,\mathrm{nmol\,L^{-1}}$. Dotted lines indicate times of 1 minute, 10 minutes and 30 minutes.

of particles adsorbed to the particles on the surface was the following:

$$M_{np}(t) = \sqrt{\frac{D}{\pi}} 2C\sqrt{t} \cdot A_{np} \tag{3.3}$$

I calculated how many particles hit the fraction of the surface that is covered with 1000 particles in the field of view for a concentration of $0.083\,\mathrm{nmol\,L^{-1}}$ for the free diffusion particles (this is the stock concentration of the used nanoparticles in this thesis) according to equation 3.3. After one minute the particles on the surface will have encountered a combined ten thousand hits with particles from the solution, so on average ten contacts per particle, which increases to approximately 600 contacts for each particle on the surface after 30 minutes (see figure 3.4.

Since the amount of hits needed to form a bond between the particle on the surface and the free particle is dependent on the orientation of both particles and time needed for the reaction when the hit occurs, the total amount of hits needed is unknown.

3.5 Batch synthesis challenges in reaction design

For the formation of nanoparticle dimers by free diffusion in solution two different scenarios are possible.
Case one: Particles have different reactivity with one having reacted with HSP90 (and purified afterwards) before mixing with the second particle. This is possible since HSP90 is smaller by an order of magnitude and therefore diffuses one order of magnitude faster in solution than the nanoparticles. It can therefore be assumed that all HSP90 has reached and reacted with a nanoparticle before nanoparticles encounter each other through diffusion. To reduce the amount of unproductive (meaning not forming a dimer) hits between the particles, one particle should be highly reactive and one of low reactivity to reduce binding of more than two particles as explained for case one in the previous section (refer to figure 3.5 left top).

The advantage of this path is that the binding of HSP90 to the particle is done in a separate step and can be tracked by for example gel electrophoresis or resonance change. The disadvantage is that an additional step of purification is needed. Since the purification is done by centrifugation, removing supernatant, the used excess of protein to react with the particle will never be fully removed, only be diluted. This residue of protein (and other reaction components from prior steps) could cause side reactions in the following dimerization reaction.

Case two: Both particle have the same reactivity and are mixed with HSP90. Here it is only possible to use a low amount of HSP90 as otherwise a full coverage of the particles with HSP90 would happen as explained above. Therefore particles with a high reactivity have to be used to ensure fast dimerization reactions after HSP90 has bound to the particle (refer to figure 3.5 left bottom).

The probability to encounter a particle with a certain number of HSP90 proteins is also given by Poisson statistics, as it is assumed that each binding event is not influence by previous ones. There, the distribution of protein number on the particles can be experimentally influenced by the ratio of particles to proteins. For the formation of an "ideal" plasmon ruler a particle with exactly one and with exactly zero HSP90 react with each other. The probability of these particle to encounter each other is given by their probability to exist in solution. I therefore calculated the Poisson equation 3.1 to calculate the product $P_\lambda(k=0) \cdot P_\lambda(k=1)$ with λ being the ration of number of particle to number of HSP90 molecules in solution. The resulting product gives the yield of "ideal" dimers relative to the total amount of particles in solution, which reaches a maximum of 18% for a ratio of two particles per HSP90. Figure 3.5 shows the plot for the yield of "ideal" dimers agains the ratio of HSP90 to particles.

For the estimation of the reaction time in a batch synthesis I used the

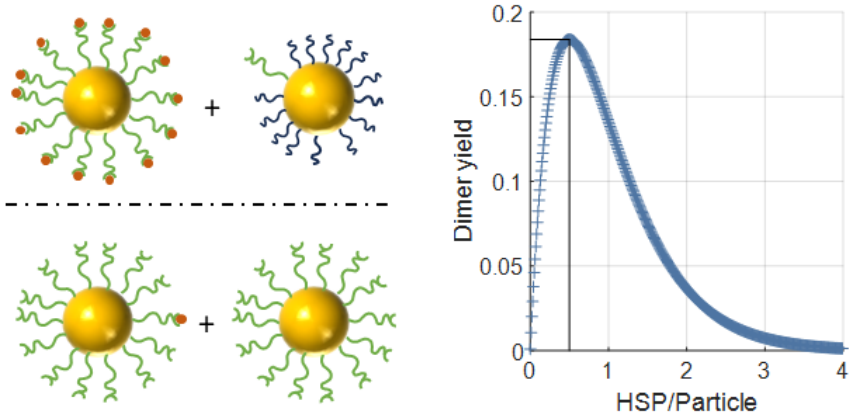

Figure 3.5: Left: Two different reaction strategies for batch synthesis of plasmon rulers. One path uses differently functionalized particles (top) where one is fully covered with HSP90 (orange dots) and the reaction partner has only one binding site. Alternatively both particles are equally reactive and HSP is present in low amounts. Right: Calculated dimer yield depending on ratio of HSP90 to particle for "ideal" dimers constructed from a particle with one HSP90 and one without HSP90 from Poisson equation (eq. 3.1)

equations from Grebenkov et. al. [58] for the diffusion of a molecule to a stationary target in cells. Their work focused on the diffusion limited reaction times in cells, where nanomolar concentrations of a signal molecule are present and diffuse to a target. Due to the similar concentrations used in plasmon ruler synthesis, I used their equation for mean reaction time (equation 3.5) to estimate the average reaction time needed to form plasmon rules. In the case of the plasmon ruler synthesis, both particles are freely diffusing, which likely causes an underestimation of the mean reaction time, since the equation assumes a stationary target.
For the diffusion of one particle three diffusion paths are considered: direct diffusion (equation 3.4) to the target, random walk diffusion with a reaction on the first hit, and random walk diffusion where multiple hits are needed for a reaction (equation 3.5) (refer to figure 3.6 left)

$$t_{direct} \approx \frac{(r_0 - r_{np})^2}{6D} \tag{3.4}$$

$$t_{mean} = \frac{(r_0 - r_{np})(2R^3 - r_{np}r_0(r + r_{np})}{6Dr_0r_{np}} + \frac{R^3 - r_{np}^3}{3\kappa r_{np}^3} \tag{3.5}$$

R is the radius of a spherical volume around the target which here is equal to the starting distance r_0 of the nanoparticle away from the target. Both are calculated from the average distance between two particles from the concentration of particles in solution. r_{np} is the radius of the nanoparticle,

D the diffusion coefficient of the nanoparticle and κ a coefficient for the reactivity of the target with $\kappa = \infty$ for perfect reactivity. If each hit leads to a reaction the last term of the sum in equation 3.5 is zero.

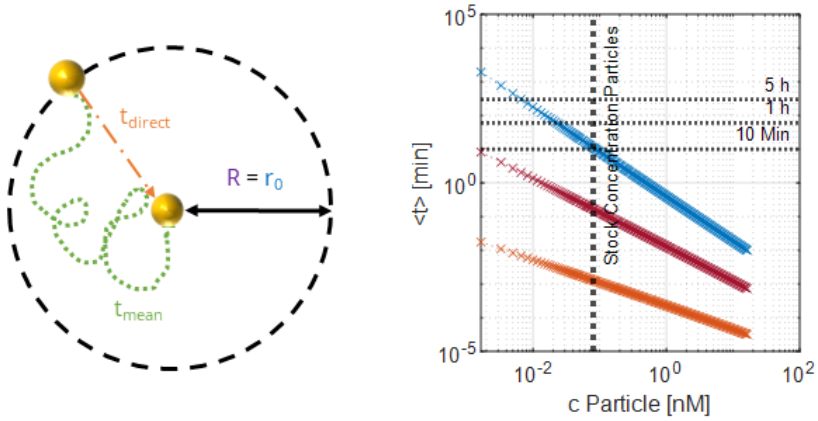

Figure 3.6: Left: Sketch of different paths for a freely diffusing particle towards another (stationary) particle. Right: Average reaction time for different pathways depending on particle concentration. Orange for direct diffusion path to the target, red for random walk diffusion with direct reaction on hit, and blue for random walk diffusion without reaction on first contact.

For the calculation of reaction times I used the same particle size and concentration as for the solid phase synthesis. For the degree of reactivity I used the general degree of imperfect reaction $\kappa/R = 1$ as given by the authors of [58]. This resulted in an average reaction time for the formation of plasmon ruler of $10\,\mathrm{min}$ (figure 3.5 right). If a perfect reactivity is assumed, the mean reaction time decreases by about two orders in magnitude to approximately $6\,\mathrm{s}$. That the reaction between both particles does not happen with each hit is likely, since on average every second particle carries one HSP90 for an optimal dimer yield. The majority of encounters will not result in a binding of the particles.

Since the actual degree of imperfection for the reaction (κ) is unknown, the above calculation is only a rough approximation for the reaction time, and the real average reaction time could be higher than estimated.

3.6 Conclusion

In this chapter I presented an overview over the advantages and challenges of forming plasmon rulers in a solid phase synthesis and in a batch synthesis.

The advantage of a solid phase synthesis is the monitoring of the particles during the reaction steps. This makes it possible to identify error sources like particles detaching or aggregating during the synthesis as well as finding correctly formed plasmon rulers by the changes in resonance wavelength and scattering intensity. The binding of the particle to the surface and stepwise reaction allows for complete purification of the reactant in each step which reduces side products. The main disadvantage is the requirement for a passivated surface, that can only bind a low amount (typically few hundred to a thousand) particles covalently.
In a batch synthesis this passivation is not needed, because the reaction is done outside of the flowcell and the resulting plasmon rulers can be deposited in dilution to not saturate the surface. This come with the loss of control over each reaction step, as the same degree of purification can't be reached by purifying the nanoparticle via centrifugation. Other methods like HPLC or gel electrophoresis can purify nanoparticle to a higher degree but might damage the protein. The advantage of a batch synthesis is the higher usable concentration and therefore lower reaction time. Potential separation of the formed plasmon rulers from the unreacted particles and aggregated of more than two particles might be done by density gradient centrifugation in the future.

For both synthesis methods I discussed the influence of different particle reactivities on the reaction regarding expected reaction times, yield of plasmon rulers and potential side products.
In a solid phase synthesis it is advised to have particles of different reactivity. If both particles are of the same high reactivity either side products or binding via multiple molecules is likely to occur. On the other side, the probability of forming a bond when both particle are low in reactivity (e.g. both have only one binding site) is very low and therefore the reaction time is long. Both reaction strategies with asymmetric reactivity are possible but with different challenges, which were discussed. I estimated the number of contacts from the free diffusing particles with the fixated particles on the surface during the plasmon ruler formation to be approximately 600 contacts per particle on the surface after 30 minutes of reaction.
For a batch synthesis of plasmon rulers I discussed the difference in reaction constraints depending on particle reactivity and limiting steps. For the case of controlling the reaction via the ration of HSP90 to particles I calculated the yield of "ideal" plasmon ruler. The highest theoretical yield was reached at a ratio of two particles per HSP90 and amounted to 18% plasmon rulers. An estimation of the mean reaction time was done by calculating the mean reaction time of a particle to a stationary target. It was assumed that not each contact of two particles results in the formation of a plasmon ruler because of the low amount of HSP90 that is present to form the connection. The average reaction time was calculated to be $10\,\mathrm{min}$, which might be a low estimation since both reaction partners are diffusing and the number of contacts needed to form a plasmon ruler is unknown.

Chapter 4

Plasmon ruler synthesis in flowcell has too low yield

Plasmon rulers have been used by the 'Nanobiotech' group to investigate the dynamics of the HSP90 protein. These studies revealed that the protein can remain much longer in a conformation than it was accessible by other methods. This raised questions regarding the ergodicity on the $24\,\mathrm{h}$ time scale, as the population of open and closed conformation did not converge for different proteins. [8, 48]
In this chapter, I present the results of the experiments conducted to improve the yield of plasmon rulers. First, I investigated the variations between individual experiments and establish a baseline yield for the synthesis method. I found that with the given protocol one sixth of the total experiments started contains functional plasmon rulers. In total we found 5 time series that show the expected behaviour of HSP90 over 21 experiments. This yield is too low for small changes in the number of plasmon rulers to be attributed to changes made in the reaction conditions. Over those experiments insufficient surface passivation was identified to be the largest source of failure. In one third of the experiments no time series were recorded because the surface was saturated with unspecifically bound particles.
Due to the low yield of functional plasmon rulers in previous experiments, Alena Kuzmina, in her master thesis [59], used particles with a higher ratio of reactive groups to enhance the formation of plasmon rulers. These particles showed the formation of aggregates of more than two nanoparticles in her experiments, but also a slight increase in success rate, as one-fourth of her experiments showed functional plasmon rulers. To reduce the number of binding sited and reduce the probability of reactions with more than one particle, I reduces the reactivity of the particle fixed on the surface. This eliminated the formation of aggregates but also did not result in formed plasmon rulers.

Although the targeted improvements in yield could not be achieved, I learned that the current level of surface passivation is not high enough. Further investigations of the surface passivation are shown in chapter 5.

In this chapter I collaborated with Alena Kuzmina who conducted the experiments of section 4.2 and parts of the experiments of section 4.1 during her master thesis. She came up with the strategy to use 11-mercaptoundecanoic acid (MUA) as an intermediate functionalization and optimized the reaction for our use case. All figures and evaluation of experiments were done by me.

4.1 Insufficient passivation is the most frequent failure source

For the investigation of protein dynamics over multiple hours Laura Tüting developed a solid state synthesis protocol in our group [48]. Her synthesis protocol involved the fixation of one particle on a passivated glass surface via biotin-streptavidin and a step by step build up of the plasmon ruler (see chapter 3 for a general reaction procedure and the appendix for a detailed reaction protocol). This reaction protocol enabled the recording of time series of conformational dynamics of the HSP90 protein over $24\,\mathrm{h}$ [8]. The long continuous recording revealed previously unknown long dwell times on the minute and hour timescales and raised questions whether HSP90 dynamics are ergodic[1] as on the $24\,\mathrm{h}$ timescale the recorded time series did not converge to a common population probability of the open closed conformation (see Figure 4.1 b).

Since the protocol yielded only a small amount[2] of functional plasmon rulers, further investigations, for example of memory effects in protein dynamics, require an improvement in the synthesis (see Figure 4.1 a). However, the authors did not report on the variance of the reaction between different experiments, which is an important metric to judge if changes in the synthesis had an impact on the yield of plasmon rulers. Therefore, I investigated the synthesis protocol of HSP90 plasmon rulers from Laura Tüting for repeatability and variance in the protocol before changing the reaction conditions.

We carried out 23 individual experiments (see Fig. 4.2 a) and found that half

[1] A system is "ergodic" if the average over an large amount of sample is identical with the average over a long time for a single sample. In the case of HSP90 this would mean that on a long enough timescale the protein occupies all possible states in a random manner. If enough individual HSP90 molecules are observed over shorter time spans, the population probability of each visited state should be the same as over a long time span for a single molecule.

[2] No absolute numbers were given on the yield of plasmon rulers in the publication

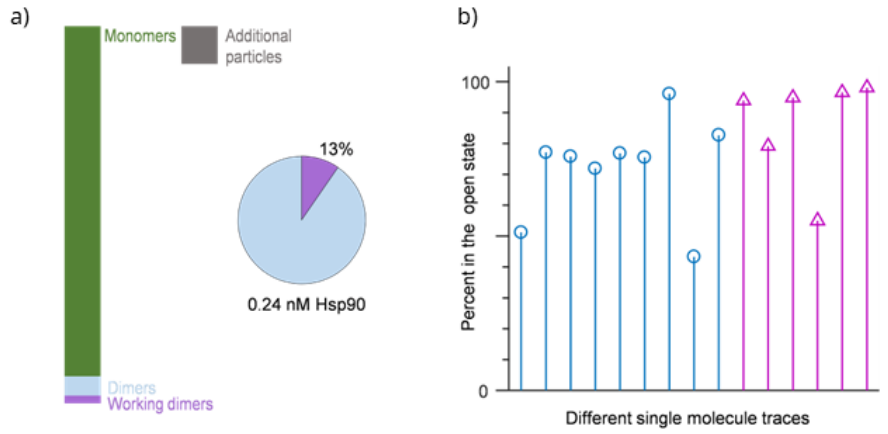

Figure 4.1: Yield and state population of HSP90 plasmon rulers. a) Bar plot shows the ratio of unreacted particles (green) to dimers (light blue) and functional dimers (plasmon rulers, purple). Inset shows that 13 percent of all formed dimers are functional plasmon rulers. b) Percentage of time spent in the open (lower intensity) conformation without (blue) and with ATP (pink) over $24\,\mathrm{h}$ time series. Reprinted with permission from [8].

of the experiments failed before the recording of data was possible (Fig. 4.2 a, blue section). One-sixth of the experiments could not be finished due to various errors, for example, an air bubble removing nanoparticles from the surface during assembly or leakage in the microfluidic cell (Fig. 4.2 a) light orange section). The majority of failed experiments was caused by an insufficiently passivated surface. This causes particles to stick to the surface unspecifically and makes single-particle measurements impossible. This was the case in one third of the experiments started (eight out of twenty three). An example image of a mediocre passivated surface can be found in figure 4.4 c) and an example of a failed passivation in figure 5.2.

For the evaluation of the yield of the synthesis, I only considered the number of functional plasmon rulers, since this is the most important metric for data generation and optimization. Any plasmon ruler that is formed and is without fluctuation between states does not contribute to the recording of conformational dynamics. These can therefore be viewed the same as a not formed plasmon ruler.

To identify the time series with fluctuation between two states, I programmed an algorithm that identifies maxima in the histogram over the intensity of the time series (for detail see chapter 7). If more than one maximum is found in multiple parts of the times series it is considered a "fluctuent"[3] and after manual filtering of all found fluctuents the yield was

[3]The term "fluctuent" was suggested by Alena Kuzmina in recent discussions to avoid priming, as labeling any fluctuating signal an "HSP plasmon ruler" excludes the possibility that

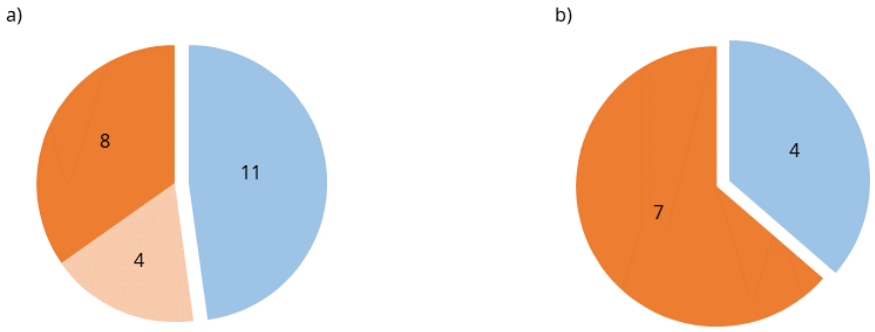

Figure 4.2: Pie chart of error sources in 23 experiments. 11 experiments (blue 48 %) could be completed and time series were recorded. Four (light orange 17%) experiments were not finished due to varying errors e.g. air bubbles removing nanoparticles during assembly. Insufficient surface passivation caused eight (35% dark orange) to fail before recording the time series. The pie chart of the fraction of experiments with HSP-like fluctuations in the successful experiments from a) 4 experiments (35% blue) showed at least 1 time series with HSP-like fluctuation between two states. The total number of these time series over the experiments was 5

calculated.
Of the successfully finished experiments, four showed times series with HSP-like fluctuation patterns in the recorded scattering intensity (Fig. 4.2 b), which means that one-sixth of the stated experiments yields the wanted experimental data. However, in total only five time series were identified as fluctuents over 21 experiments (see figure B.1 for two examples of the time series). This yield is too low to reliably record the needed sample size of data for further investigations on the HSP90 protein.

For the low yield of functional plasmon rulers, I hypothesize two reasons. Because the experiments showed inconsistent surface passivation, it cannot be excluded that there are "empty" spots on the surface where a correctly formed plasmon ruler sticks to the surface with both particles. Alternatively, two particles sit on the surface close enough that plasmon coupling occurs without being connected by HSP90. When using intensity and resonance changes as an indicator for dimer formation, as it was done by Laura Tüting and Weixiang Ye in our group, both cases would count as a formed plasmon ruler but do not show fluctuation. Although I did not investigate the amount of nonfluctuating plasmon rulers, this could explain the reported 87% of nonfunctional plasmon rulers (see figure 4.1 a, inset).

A second reason is that the majority of deposited particles does not react

the signal is caused be other sources.

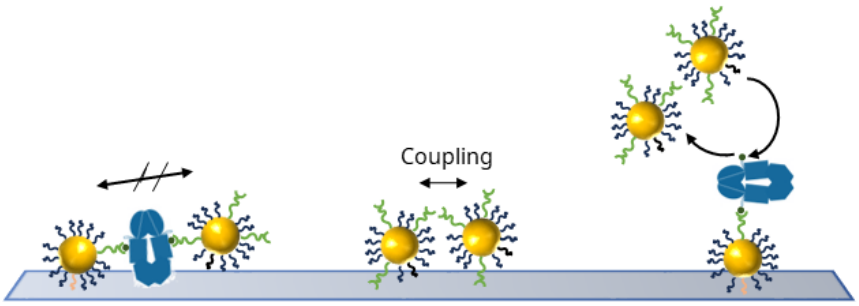

Figure 4.3: Sketch of possible reasons for low plasmon ruler yield in experiments. Left: Both particles of the formed ruler stick to the surface, locking the protein in one conformation. Middle: Two particles sticking to the surface with close enough distance to enable coupling. Only the case without HSP90 is drawn. Right: Particle hits do not form covalent bond because not all parts of the particle are reactive. Particle and protein are not drawn to scale.

with a second particle and thus don't form plasmon rulers. The particles used were functionalized according to the reported protocol where the first particle immobilized on the surface is functionalized with a ratio of 87:10:3 of HS-PEG-OMe : HS-PEG-biotin : HS-PEG-NH_2. The free diffusiing second particle is functionalized with a ratio of 97:3 of HS-PEG-OMe : HS-PEG-NH_2. As discusses before about half of the amino groups are not accessible for further reaction because they are stuck in the PEG coil [55], which results in an average of 1.5% of active PEG chains per particle. This low of amount of active funtional groups on both particles reduces the chance of forming dimers during the assembly process as I discussed in more detail in chapter 3.

From those hypothesis, I concluded two challenges for the solid phase synthesis of plasmon rulers:
1) The surface passivation lacks consistency and causes a large portion of experiments to be aborted. To increase the experimental throughput, the consistency and quality of the surface passivization should be increased to avoid correctly formed plasmon rulers from sticking to the surface. This also reduces the chance for particles to stick in close proximity to other particles on the surface and inflate the yield of plasmon rulers when resonance wavelength and intensity are used for plasmon ruler identification (figure 4.3 middle). The efforts made to improve the surface functionalization are covered in Chapter 5.

2) The yield of functional plasmon rulers is too low for small changes between different experiments to be attributed to variations in the reaction conditions. A random difference of one flucutent more or less in an experiments could double the yield. As discussed the functionalization strategy does not promote the formation of dimers and should therefore be changed. To investigate the influence of reaction parameters on the yield of fluctuents, the yield of fluctuents in an experiment should be increased by an order of magnitude.

4.2 Increasing particle reactivity leads to more binding events

To improve the number of functional plasmon rulers, either the amount of formed dimers or the fraction of functional dimers can be increased (ideally both). We decided to work on increasing the total number of formed dimer constructs. The approach was to boost the reactivity of the particles flushed in to form the dimers by increasing the amount of amino-PEG on the particle's surface. In contrast to the functionalization strategy discussed in chapter 3 we didn't also decrease the reactivity of the fixed particle by further reducing the ratio of used amino-PEG. The decision was made not to change multiple variables at once, because conclusions about which particle has a higher influence on the formation of dimers could otherwise not be made.

Because a functionalization with only amino-PEG can lead to unstable particles (for example seen on silver nanoparticles in [60]) an additional reaction path via an intermediate was chosen to avoid aggregation[4]. The intermediate of functionalizing the nanoparticle with 11-Mercaptoundecanoic acid (MUA) was chosen due to the established protocols in the group. Carboxylic groups are then chemically transformed into amino groups (Fig.4.4 a). The resulting particles carry only amino groups and should result in a fully reactive particle, therefore, increasing the amount of plasmon rulers formed. For both types of synthesized particles (direct and indirect routes), four experiments were carried out (Fig. 4.4 b). The particles functionalized with 100% amino-PEG did not produce any functional plasmon rulers (Fig. 4.4 b) left half). The particles functionalized via the MUA intermediate showed in two out of four experiments time series which were identified as fluctuating between two states. Figure 4.4 c) shows an image section of the experiment with the most fluctuents (in total four), the left side before flushing in the fully reactive particle, and the right side after the reaction. Two things are of note here. First, there are more particles visible in the image after the reaction. This again shows that the surface was not fully

[4] In practice both reaction paths give particles that have to be handled with great care in the purification steps to avoid aggregation. For synthesis and purification protocols, see appendix and [59]

passivated against unspecific particle binding. An alternate explanation is that the higher amount of amino groups increased the electrostatic attraction between glass and particle because of the higher surface charge of the nanoparticles. Previously the nanoparticles were functionalized with 15% amino-PEG and 85% methoxy-PEG (see A). The inert methoxy groups don't interact with the surface. On a perfectly functionalized surface both particles should not stick to the surface due to the PEG chains on both surfaces. Otherwise also PEGylated particles would aggregate, which is not the case. Therefore it might be possible the even in previous experiments the passivation didn't cover the full surface. Due to the lower affinity of the particles with 15% amino-PEG to the surface, this was not an issue as the particles did not interact strong enough with the spots without passivation. Second, the particle color in the right image is mostly yellow to orange. This shows that at least two particles are in close enough proximity to cause coupling of the plasmons. The nanoparticles used in this experiments have an average diameter of $40\,\mathrm{nm}$ and if separated by an HSP90 protein are $19\,\mathrm{nm}$ apart [8]. Using the plasmon ruler equation from Jain et. al. [40], and a resonance wavelength of the nanoparticle on the glass surface of $560\,\mathrm{nm}$ [22], the resulting change in the resonance wavelength is approximately $13\,\mathrm{nm}$. A single particle appears as a yellowish green ($\lambda_{res} = 560\,\mathrm{nm}$, rgb (195, 255, 0)) and a plasmon ruler as a greenish yellow ($\lambda_{res} = 573\,\mathrm{nm}$, rgb (234, 255, 0)) [5].

To identify the fomred plasmon rulers in the experiments I plotted the relative change in the scattering intensity I/I_0 against the shift of the resonance wavelength λ_{res}. Particles that did not form plasmon rulers should not change their resonance wavelength or scattering intensity. The expectation was therefore to see distinct clusters in the plot depending on the number of particles that have reacted. This however, is not the case. Figure 4.4 c) shows a scatter plot of the measured change in resonance wavelength $\Delta\lambda_{res}$ and relative intensity change I/I_0. The large increases in scattering intensity of a factor 100 for some particles as well as large shifts of the resonance wavelength of 50 or more nanometers, indicate aggregation of multiple particles. One would expect to see two (or more) distinct clusters in the plot of the scattering intensity (figure 4.4 d) by the amount of plasmons that couple, which is not the case here. Most likely the polydispersity[6] of the particle is too large for different populations to be visible. All identified time series with fluctuations stopped after incubation with AMP-PNP[7], indicating that the fluctuations were caused by conformational changes in HSP90. Yet those fluctuents do not show similarities regarding shift in resonance and relative intensity. This could either mean close to all particles have formed plasmon rulers, yet only four of them show fluctuation. Or the change

[5] RGB codes were generated on the following website: "https://academo.org/demos/wavelength-to-colour-relationship/", February 10th 2024.

[6] Polydispersity is a measure of the size distribution of nanoparticles.

[7] Adenylyl-imidodiphosphate (AMP-PNP) is a non hydrolizing derivate of ATP, which binds to the ATP binding pocket of HSP and locks it in the closed conformation.

in resonance wavelength and scattering intensity cannot be used for the identification of plasmon rulers, as the variation in both parameters is too high due to the polydispersity of the nanoparticles.
Although an increase to five found HSP90 dimers over four experiments is a noticeable increase compared to five over twenty one, the absolute number of plasmon rulers per experiments remains low. Therefore changes in the number of functional plasmon rulers cannot be attributed to the changes made in the reaction conditions. The change in reactivity did therefore not lead to an increase in formed dimers but most likely to the formation of aggregates of more than one particle. This matches the hypothesis made in chapter 3 for the case of two reactive particles. In the tested synthesis particles with 100% amino-PEG reacted with particles that carried 3% amino-PEG (particle on the surface). Therefore it is likely that the used amount of amino-PEG on the particle on the surface offers too many binding sports and should be reduced to avoid aggregation.

4.3 The reduction in reactivity resulted in no functional plasmon rulers

Increasing the reactivity of the free diffusing nanoparticle has lead to the formation of aggregates of more than two nanoparticles. However aggregates of more than two nanoparticles do not yield time series that represent the dynamics of a single protein. To reduce the probability to bind on multiple points on the particle that is bound to the glass surface, we reduced the number of binding sites on this particle to 0.5% amino-PEG. We also used a reference particle, that does not carry HSP90, to probe for unspecific aggregation between the particles.

The experimental steps are depicted in figure 4.5 a. The resonance wavelength of the particles in each group (plasmon ruler forming group and reference group) is presented below the reaction scheme. We used the same reaction protocol as before until HSP90 has bound to the nanoparticle on the surface. Then, we flushed in particles from the same batch (functionalized with 0.5% amino-PEG) and bound them to the surface as well. These particles act as a reference group. Since amino groups (on the now flushed in nanoparticle) and thiol groups (on the HSP90 on the previously bound nanoparticle) cannot form a covalent bond there should be no reaction. We did not observe a change in the resonance wavelength for the nanoparticles on the glass surface after the introduction of the reference particle, which indicates that not aggregation through unspecific binding occurred. After this step the synthesis protocol was resumed as before, which resulted in one group of particles that carry HSP90 and should form plasmon rulers (labeled "G1" in figure 4.5 a, blue markers) and one group of particles without HSP90 that should not bind any other particles (labeled "G2" in figure 4.5 a, orange markers).

Calculating the change in the resonance wavelength for each step relative to the first deposition of the particles showed again that the addition of the reference particle did not influence the resonance wavelength of the particles carrying HSP90 (see figure 4.5 b). There is no significant shift visible for the addition of HSP90 because the amount per particle is too low to cause a change in the resonance wavelength larger than the measured standard deviation of one nanometer. Comparing the particles with HSP90 (G1 blue markers, which should form dimers) and the control group (G2, orange markers) after the completion of the protocol there was no significant difference between the two groups of particles. For the control group a few particles showed large changes in scattering intensity and resonance wavelength (see figure 4.5 c) which indicates that aggregates of multiple particles were formed. However, in both groups, no time series with fluctuation between states was found.
Therefore the reduction in the reactivity of the particle on the surface has succeeded in reducing the formation of aggregates of multiple particles, but failed in increasing the number of functional plasmon rulers.

4.4 Conclusion - Solid phase only yields singular time series with fluctuation

In this chapter the repeatability of the published reaction protocol for the solid phase synthesis of HSP90 plasmon rulers was investigated to gather insight for the optimization of the reaction. For this we repeated the reaction protocol and found that surface functionalization presented a major challenge. The given passivation protocol did not result in consistently functionalized surfaces that prevented unspecific binding. This caused one third of the experiments to fail before the recording of a time series. A too dense population of the surface with nanoparticles does not allow for single-particle experiments. Additionally, we found two third of all experiments did not yield any time series with signals typical for HSP90. In the successful experiments, the total number of HSP90 typical signal was five in four experiments. This number is too low for systematic optimization of the reaction protocol. A singular randomly formed or not formed plasmon ruler can increases the yield by 100% or caused the experiment to not contain any.
To increase the probability of dimer formation, we increased the number of binding sites on the particle. Refer to chapter 3 for more details on reaction control in the synthesis of solid phase plasmon rulers. The experiments conducted showed high amounts of aggregation of multiple particles evident by the observed large increases in scattering intensity of more than twenty times and shifts in the resonance wavelength of more than the expected $13\,\mathrm{nm}$ for plasmon rulers. While the increased reactivity did lead to more binding of particles, it did not increase the yield of time series with HSP90

typical signals.
To counteract the reaction of multiple particles, the reactivity of the fixed particle was reduced. This suppressed any reaction of the particles with each other and resulted in no measurable difference between a group of particles with HSP90 and without HSP90. The balance of reactivity between both nanoparticles seems to be delicate and would require more experiments to fine tune.

However, the inconsistency found in the surface passivation provides a challenge for the optimization of the solid phase synthesis. It can cause experiments to fail before recording data and potentially cause correctly formed plasmon rulers to not fluctuate as both particles can stick to the surface.
Therefore, I decided to work on the passivation of glass surfaces for the synthesis of plasmon rulers before optimizing the synthesis (see chapter 5). Additionally, I developed a batch synthesis as this synthesis that does not require a passivated surface. The results of the synthesis are presented in chapter 6.

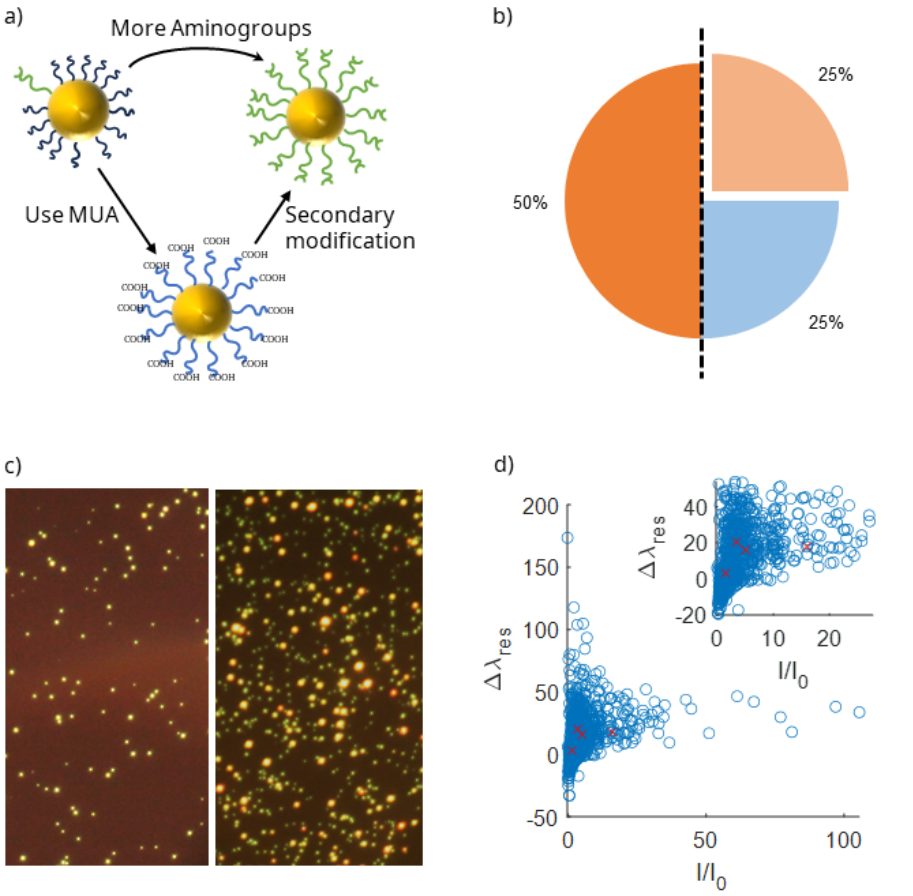

Figure 4.4: a) Cartoon of two strategies to increase the amount of binding sites on the dimer forming nanoparticle. Black arrow: replacing methoxy-PEG (black) with amino-PEG (orange) in functionalization Blue arrow: functionalizing with MUA and changing the carboxy group in a second step to amino. b) Pie chart of experimental results using starts from a) Left half was using the amino-peg way, where out of 4 experiments all showed no working plasmon rulers, and right half was using the MUA way, where 2 out of 4 experiments showed working plasmon rulers with a total of 5 working dimers in total. c) Real color image section from the field of view form a successful dimer synthesis using the MUA way. The top shows the field of view (FOV) section before the second particle was introduced. Green dots are singular gold nanoparticles. The bottom shows the same section of the FOV after incubation with the dimer-forming particle. Note that there are visibly more particles indicating insufficient passivation of the surface. d) Scatter plot of resonance change versus relative intensity change on dimerization. Blue circles are particles without fluctuation in the time series, and red crosses the identified dimers. No clustering of functional plasmon rulers can be identified.

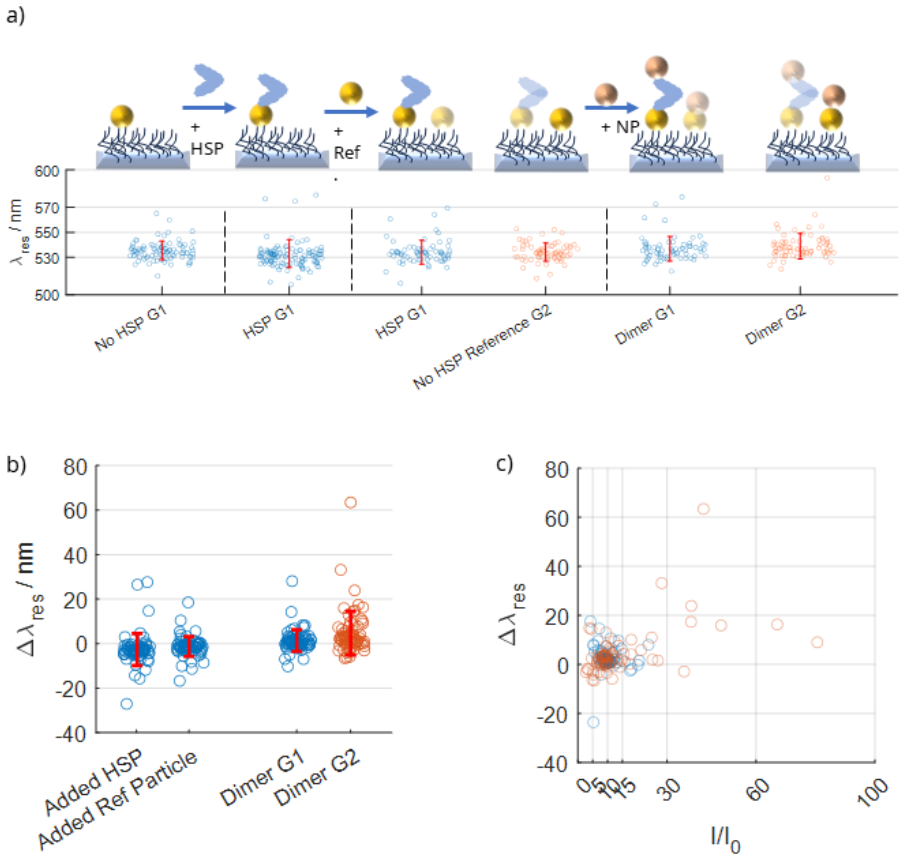

Figure 4.5: Resonance wavelength for reactive and control group during flowcell synthesis of HSP90 plasmon rulers Top: Sketch of the synthesis; opaque drawings belong to the scatter plot below. Bottom: Scatter plot of nanoparticles in the flow cell during each reaction step. Each circle is an average from three consecutively measured resonance positions with a mean standard deviation of 1 nm per particle. The red error bar indicates the standard deviation for all particles per step. b) Scatter plot of change in resonance for both particle groups. Red error bar is calculated from the standard deviation over all resonance changes is a reaction step. Over the reaction, there is a collective shift toward higher wavelength. Upon adding a second particle for dimerization, the control group shows a higher amount of particles with resonance changes above 10 nanometers than the groups intended to form plasmon rulers. c) Scatter plot of resonance change against relative intensity change in the dimer forming step. Blue circles are data from reactive particles intended to form plasmon rulers, orange circles the reference group.

Chapter 5

Passivation of glass surfaces for plasmon ruler experiments

Making measurements of single molecules or particles requires a small amount of analyte to bind to a surface without saturating the surface. To avoid undesirable binding events, altering the surface by covalent binding of silane components is a common practice[13, 61–63]. In our research, we utilized the passivation reaction described by Schenk et al. [61] to prevent the adhesion of gold nanoparticles to the glass surface of the microfluidic cell. This reaction involves the use of trimethoxy-silane-polyethyleneglycols (PEGs) to stericly shield the surface from interacting with the nanoparticles.[1] By using a 1 % fraction of silanes that offer a binding site, it should be possible to immobilize a small number of particles onto the surface via biotin-streptavidin (for a detailed explanation, see Chapter 4).

In this chapter, I present the results of using three different methods [61, 64] to passivate a glass surface and prevent unspecific binding of gold nanoparticles. First, I introduce the chemical reaction mechanism for silanization of glass surfaces and discuss the reaction conditions used in the literature. Data is presented for two reaction conditions of silanization with trimethoxy-silane-PEG: one in basic and apolar conditions, and one in aqueous acidic conditions. Both conditions proved to be not suitable for single particle plasmon ruler experiments.
A comparison is made with a two-step passivation protocol where in a first

[1] Steric passivation is a process that involves a reduction in entropy. When the polyethylene glycol chains on the surface and on the nanoparticle are in contact, an ordering process has to occur to present enough contact area for van der Waals forces to form which are strong enough to keep the particles bound. This ordering of the chains results in a reduction of degrees of freedom (entropy), which is unfavorable.

step the small molecule Aminopropyl-(trimethoxy)silane (APTMS) silanizes the surface and in a second reaction step a PEG molecule is bound to form the passivation layer.
Finally, it is demonstrated that the (co-)passivation technique utilizing bovine serum albumin (BSA)[65–69] cannot be used in conjunction with the current strategy for binding the HSP90 protein to the nanoparticles. The conjugation of amino (on the nanoparticles) and thiol (on the protein) groups is done through Succinimidyl-4-(N-maleimidomethyl)cyclohexan-1-carboxylate (SMCC). As BSA also contains a free thiol group, nanoparticles can bind to BSA.

In this chapter, I collaborated with Daniel Lauxen, who conducted experiments on the storability and repeatability of passivation in toluene. Leonie Vollmar, from the research group of Professor Thorsten Hugel at the University of Freiburg, taught us the passivation protocol applied for their FRET experiments. Additionally, Biswajit Pradhan from the group of Eugene Kim at MPI Frankfurt kindly provided us with glass slides that were passivated, and he showed the two step passivation protocol to Alena Kuzmina to use in our group. Alena Kuzmina and Eva Wächtersbach performed testing of his protocol for our use case.

5.1 Different reaction conditions for the same reaction

Preventing non-specific binding is crucial in plasmon ruler experiments for multiple reasons. Firstly, during the solid-phase synthesis reaction process (refer to Chapter 4), a large number of particles are used to form nanoparticle dimers. If particles stick to the surface the dimer formation is influenced in different ways, depending on the distance between the bound particles. When the particles are further apart than the optical resolution limit[2], the particles are separated and visible as two distinct dots or as a peanut shaped object. Since we record the scattering intensity over a disc shaped area and the background of the particle in an area of a few pixels around the disc, any particle inside this area would cause a higher recorded background signal. Therefore, our software discards any particle where either the particle shape is not a symmetrical dot (e.g. peanut shaped) or other particles are detected in the area around the particle used for background correction. Assuming one correctly formed plasmon ruler and another particle are separated less than the optical resolution limit, the signal-to-noise ratio would decrease, as the signal causes by the plasmon ruler now makes up less of the total recorded signal. Alternatively, if a particle unspecifically adheres to the glass next to another particle with a

[2]Using the Rayleigh limit to determine the minimal distance at which two sources of light (in this case the nanoparticles) can be distinguished: $d = 0.61 \cdot \frac{\lambda}{n \cdot \sin \Theta} \approx 0.61 \cdot \frac{600nm}{1.5} \approx 250\,\mathrm{nm}$

distance lower than the particle diameter, coupling of the plasmons occurs (refer to chapter 2) and therefore looks like a correctly formed plasmon ruler but gives no signal. (See Figure 5.1 a)

When gathering experimental data without a passivated surface, if both particles of the plasmon ruler have the potential to adhere to the surface, the motion of HSP90 may be impeded, resulting in lower data output. The HSP90-triggered distance change can be modified through surface interaction. For example, a tapping of the free particle on the surface can extend the dwell time as the attractive force between the surface and the particle must be overcome before conformational changes can resume.

Therefore, I came up with three criteria for a well-passivated surface in plasmon ruler experiments.

1. No more than 1% of the total particles show non-specific binding.
2. The reaction leaves no light scattering residues on the surface.
3. A low amount of binding site that stably holds particles in place for several hours.

Reaction mechanism I examined various published procedures for functionalizing glass with the molecule types used in this chapter's experiments (APTMS and Trimethoxysilane) and compared their reaction conditions [61–64, 70–74] (Fig. 5.1 c)[3]. All presented reactions dissolve siloxanes (R-Si(OR)3) in a solvent and use a borosilicate (laboratory glass) substrate. The reaction conditions vary widely (see Figure 5.1 b).
While one group reports a successful reaction under acidic conditions in water, another group reports success using a weak base in water-free toluene. The use of heating during the reaction (and curing of dry slides in an oven) varies among groups. Additionally, reported reaction times range from 15 minutes to overnight or up to 24 hours. All reactions in the here made comparison are claimed to be effective and are using molecules that should follow the general reaction mechanism of Figure 5.1 b). This suggests that the reaction functions independently of the reaction conditions employed (which is doubtful) or that the specific glass substrate utilized has a greater effect on the reaction than is acknowledged.
The reaction is postulated to work like this: the first step involves the hydrolysis of alkoxy silane into the silol in a state of equilibrium (See Fig. 5.1 bottom section A)). These silols can undergo oligomerization to form longer chained siloxanes which bind to the hydroxy groups on the surface and form a covalent bond with the surface after the elimination of water. The mechanism indicates that heating is necessary in the final step to remove water.

[3]For an overview over reaction conditions for different substrates, different cleaning procedures and silanization molecules, please read: "Organosilane deposition for microfluidic applications. *Biomicrofluidics* 2011" by Nick Glass [75]

A few observations can be made from the reaction mechanism. Firstly, the reaction requires water to form chains that bind to the surface. Secondly, water acts as a catalyst as it is regained when forming the covalent bond with the surface. Thirdly, for the reaction to occur, the surface must have hydroxy groups.

Adsorption to heterogeneous surfaces [76] Multiple factors influence the coupling of silane components to an interphase[4]. The pH of the silane solution is important because it affects the relative rates of silane hydrolysis and condensation. Secondly, the pH impacts the surface potential, that can only be calculated as an average over the entire component for mixed oxide surfaces such as glass due to micro-heterogeneities. This chemical heterogeneity varies not only between manufacturers and batches but also over the history of the substrate, including how it was cleaned and stored. The shape of the surface to be treated with the silane component, be it in the form of a plate, sphere, or cylinder, has an influence on the chemical reactions that occur. Even when the diameters of the same geometry are varied, this chages the surface potential and therefore the reactivity of the surface.

The condensation of neutral alkoxysilanes is catalyzed by aliphatic amines, whereas basic functional groups, for example, amines in APTMS, self-catalyze the hydrolysis reaction. The quantity of water in the reaction system impacts the extent of polymerization in solution. Excessive water leads to excessive polymerization, while a water deficiency results in the formation of an incomplete monolayer. The drying conditions affect the structure of the adsorbed silane layer as the number of siloxane bonds between adjacent silanes and with the surface is influenced by temperature and duration of the curing.

Lastly, "[s]olvent, concentration, reaction time, and reaction temperature all have an effect on the attachment kinetics, but most studies only examine one or two of these parameters, and so often a consistent picture of silane adsorption remains missing." [76]

5.2 Storage does not degrade passivation

In chapter 4, I showed that insufficient passivation caused 35% of experiments to fail due to non-specific adsorption of particles during the plasmon ruler assembly. This resulted in a too densely packed surfaces for single particle experiments when using the in our group established method for silanization. This method uses trimethoxysilane-PEGs in dry toluene carried

[4]Janis Matisons' book chapter "Silanes and siloxanes as coupling agents to glass" provides great insight into the reaction and factors affecting the coupling of siloxanes to glass which is the basis for this section.

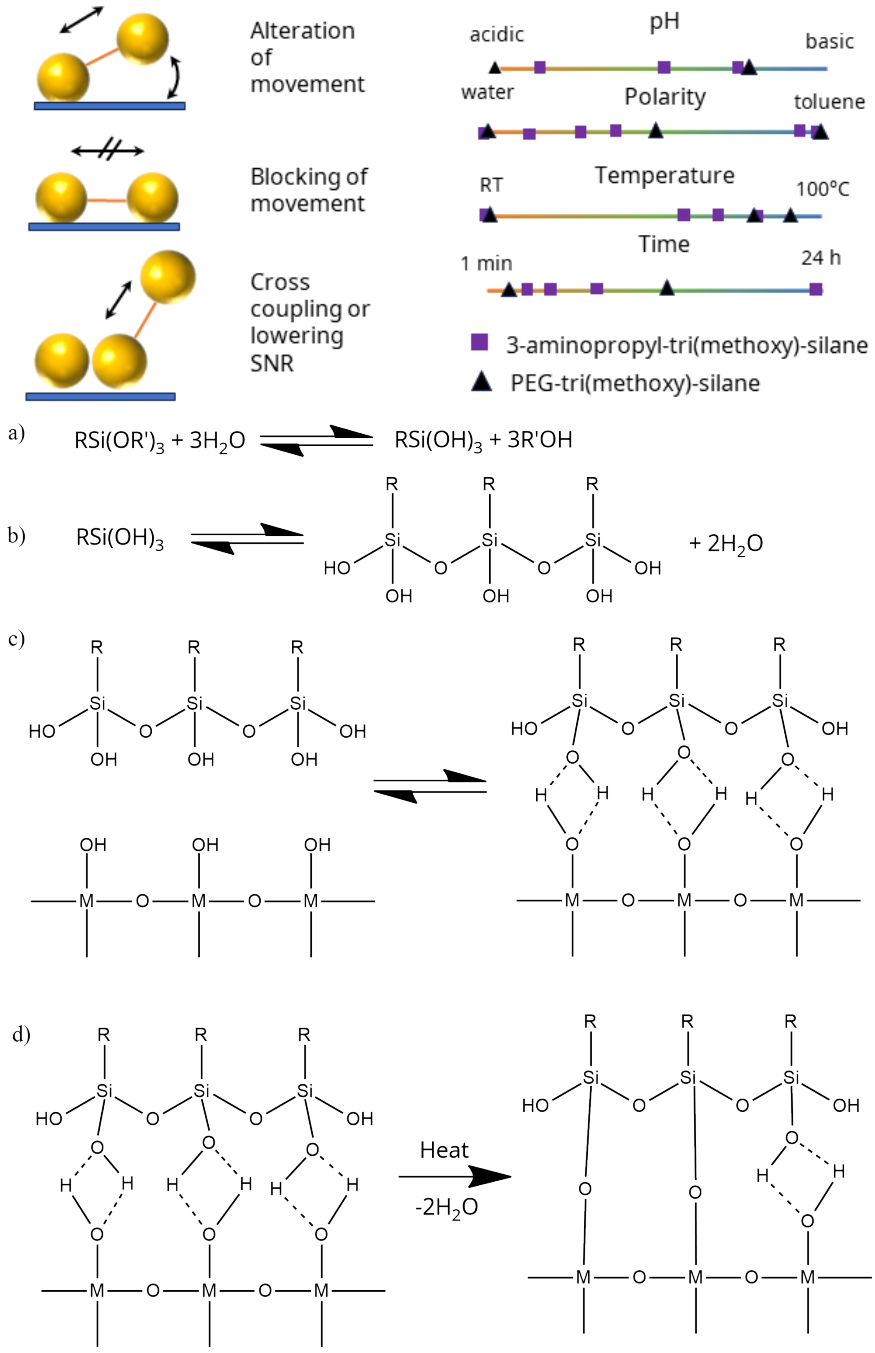

Figure 5.1: Top left: Sketch of surface interactions of HSP90 plasmon rulers. Top right: Qualitative overview over reaction conditions for the silanization with the components used in this chapter [61–64, 70–74]. Bottom: General reaction mechanism for siloxane with metal oxide surfaces [76].

out at $90\,^{\circ}\mathrm{C}$ over night, with triethylamine as a weak basis for catalysis. Due to the challenges in reproducability of this passivation protocol, we tested whether the slides passivated by this method could be stored. Our aim was to test one slide from each batch and store them if one batch produced a passivated surface. For this we stored the prepared surfaces under three different conditions: at room temperature in the laboratory, in a fridge at $4\,^{\circ}\mathrm{C}$ and in a freezer at $-20\,^{\circ}\mathrm{C}$ for up to five weeks.

Figure 5.2 a) shows a real color image of a well passivated surface after treatment with gold nanoparticles (functionalized with HS-PEG-NH_2) for 30 minutes. In the field of view, three nanoparticles (bright dots) were observed to have bound unspecificly, allowing for the use of this slide in single particle experiments with the specified constraints. Section b) in Figure 5.2 displays an image section of a surface exhibiting inhomogeneous passivation. The white particles present on the surface are most likely self-polymerized silane-PEGs. Although we used dry toluene, it cannot be excluded that water from the air and residual water on the surface of the reaction vessel are present and lead to the formation of oligomers.

We studied the inhomogeneity of the passivation by treating three freshly prepared surfaces with gold nanoparticles and determining the number of particles on different sections of the same surface. Quantifying the number of particles was done using Matlab[5]. As shown in Figure 5.2 c, none of the surfaces had an average particle count below 8000.

Three surfaces were prepared for each of the storage conditions and for each storage time. Although the number of particles varied between the stored weeks, a clear trend was not recognizable (see Fig. 5.2 d). The variation in particle count on the surface over time and storage condition falls within the previously determined range for the reaction. However, the surface passivation does not appear to be deteriorating over time as a result of storage conditions, indicating the possibility of future storage.

5.3 Silanization in aqueous hydrochloic acid leaves residues on the surface

The group of Thorsten Hugel collaborating with us on the Plasmon Ruler Project also employs surfaces that are passivated with trimethoxy-silanes in their experiments. The reaction is conducted in aqueous HCl at room temperature.

We tested whether the reaction protocol leads to surfaces that meet the criteria for our experiments, and we also varied the reaction conditions by using different amounts of PEG, solvents, and cleaning steps. The provided method utilized BSA as a copassivation agent to fill in gaps in the formed PEG layer. In the initial experiments, BSA was excluded to improve comparison

[5]The inbuilt function "imfindcircles" was used, which finds circular objects in images.

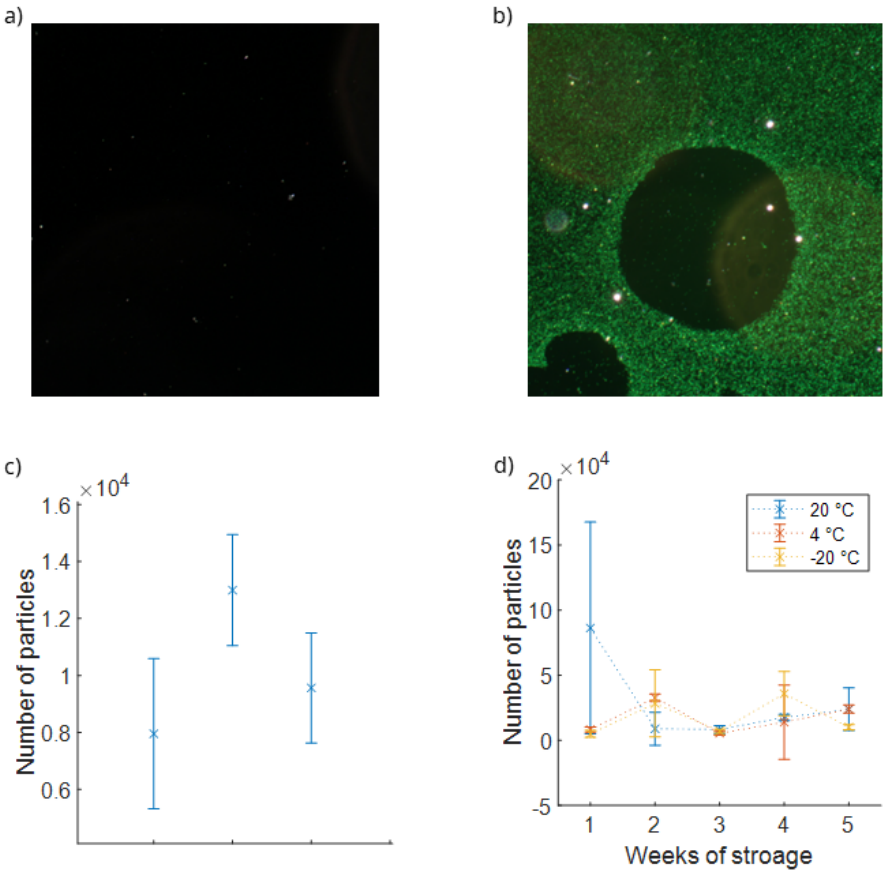

Figure 5.2: a) Real color image of a well passivated surface after incubation with functionalized gold nanoparticles. White scattering particles are most likely residues from the passivation reaction. b) Real color image of an inhomogeneous passivated surface. Green dots are gold nano spheres. The island in the middle right shows less particle binding than the areas around it. White spots are residues from the passivation reaction c) Average number of particles binding for three freshly prepared flowcells. Average taken over different positions in the flowcell, errorbar given by the standard deviation. d) Number of particles binding for different storage conditions and storage times. No trend can be identified indicating that the initial quality of passivation is more impactful than storage condition or duration.

as the previous protocol did not incorporate BSA. The impact of BSA on passivation quality will be assessed in a different section of this chapter.

Figure 5.3 shows a sample field of view of a passivated surface before (a) and after (b) treatment with nanoparticles. Comparing the color images with those in figure 5.2, it is clear that the reaction in toluene produced a surface that binds more particles. In contrast, the reaction in water produced a surface with many white dots before the nanoparticles were added. These residues may either elevate the background or scatter brighter than the nanoparticles, rendering some parts of the surface unusable.

Comparing particle adhesion across different silane-PEG concentrations (ranging from $8\,\mathrm{mg}\,\mu\mathrm{L}^{-1}$ to $80\,\mathrm{mg}\,\mu\mathrm{L}^{-1}$) in both water (conditions 1 to 4) and ethanol for plasma-cleaned surfaces (see Fig. 5.3c), we found that no tested reaction condition resulted in less than one thousand bound particles on any given surface section. This number is too high for our experiments. We also investigated whether passivation against nonspecific adhesion could be enhanced through RCA cleaning, replacing HCl with acetic acid, and post-curing in an oven, as those conditions were reported in literature. However these experiments were only done on a single field of view and therefore do not allow for a generalized conclusion (refer to the appendix).

None of the tested conditions produces a surface that meets the criteria for a passivated surface to be used in our experiments.

Contact angle measurements were performed to assess if the contact angle is correlated to the passivation quality. This would give an alternative way to test for the passivation quality before building a flow cell and flushing in nanoparticles. The handheld device used[6] was temporarily provided by the group of Prof. Siegfried Waldvogel and not used in later studies. However, as evidenced in Figure 5.3 c) and d), no definitive correlation was observed between the contact angle (water/air/glass) and the number of particles adhering to the surface. Condition three bound the highest number of particles and yielded the same mean contact angle as condition one, which bound approximately one third of nanoparticles. Therefore, the contact angle of water on the passivated surface cannot be utilized to evaluate the efficiency of the passivation reaction.

5.4 Silanization with aminopropyl-trimethoxysilane leaves residues

Neither of the tested methods for functionalizing glass surfaces with trimethoxy-silane-PEGs met our criteria for creating a passivated surface in our darkfield experiments.

Another method involves binding the small molecule Aminopropy-trimethoxysilane (APTMS) to the surface, followed by functionalization with PEG in a second

[6] Krüss Mobile Surface Analyzer "One-Click SFE"

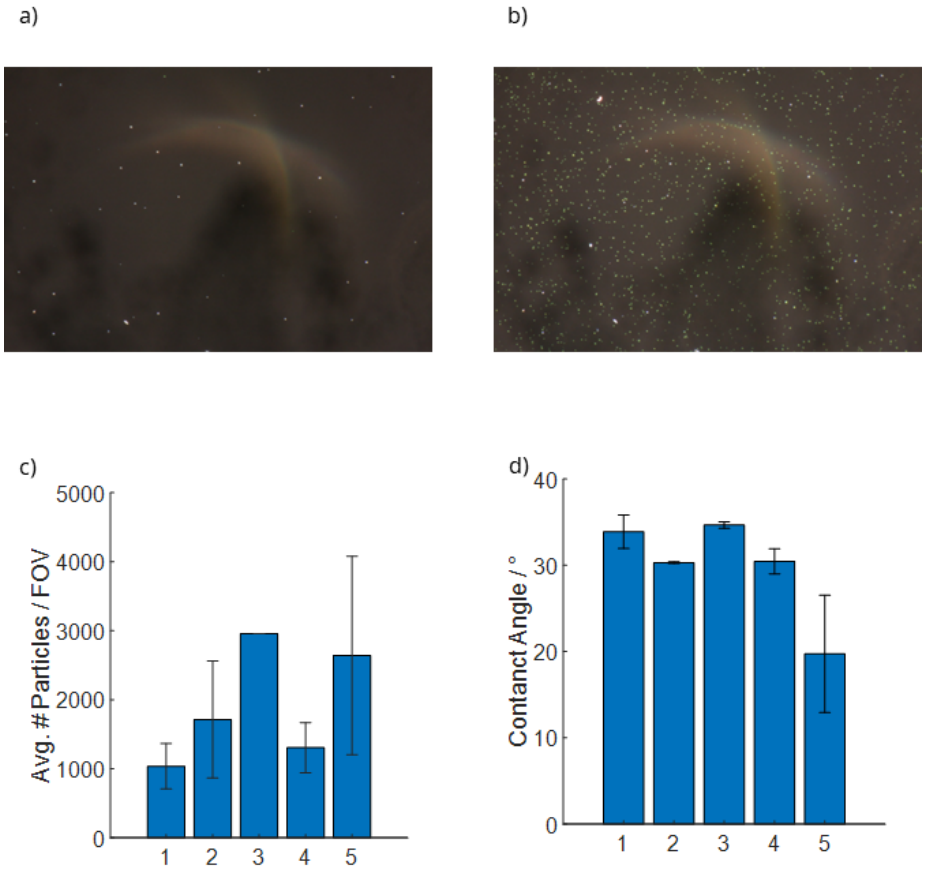

Figure 5.3: a) Real color image of passivated flow cell prior to particle incubation. White dots are scattering residues from the PEGylation. b) Real color image of the same surface after incubation with nanoparticles functionalized with 10 % Amino-PEG for 30 minutes. c) Bar plot of average numbers of particles sticking to the surface for different reaction conditions d) Bar plot of average contact angle (water-glass-air) for each tested condition. Contact angles were taken on three different spots.

step. For the functionalization, we employed the protocol offered by Biswajit Pradhan [64], which he has kindly provided and shown us in practice. The full protocol can be found in the Appendix.

Comparing images of particle-free surfaces, it is noticeable that this method leaves more white scattering residues on the surface (refer to Fig. 5.4 a and Fig. 5.3 a). Again, these are probably polymers of the APTMS used, as the reaction occurred in water. When treated with nanoparticles, this passivation method did not prevent particle attachment to the surface.
We learned from a prior study [48] that PEG chains form crown ethers with potassium ions and therefore a denser coil. To increase the packing density of PEG on the surface, we performed PEGylation of our APTMS surfaces under different amounts of potassium chloride. The expectation was that higher degrees of potassium would lead to a denser packing of PEG on the surface, resulting in fewer adhered particles. However, the opposite effect occurred (Figure 5.4 c).

A hypothetical explanation could be the entrapment of ions within the PEG chain. This could potentially increase the attractive forces between the nanoparticles and the surface, resulting in non-specific binding, similar to the aggregation of nanoparticles caused by higher salt concentrations that shield surface charges.

5.5 Co-passivation with BSA can not be used with SMCC for dimer formation

The passivation protocol from Biswajit Pradhan and the protocol from Thorsten Hugels group, both, use BSA a a co-passivation agent to fill gaps left after the passivation with PEG.
We tested if the copassivation decreases the number of particles bound, by building our flowcell with one slide which was passivated using APTMS + PEG and one without any treatment. To evaluate the impact of BSA, we incubated passivated slides with $10\,\mathrm{mg/mL}$ BSA in our measurement buffer (HEPES pH 7.4) for a duration of 30 minutes.
For the surface passivation of Pradhan, two different slides. One was passivated according to protocol, the other one was not and was used as a control without PEG. We then flushed in nanoparticle functionalized with SMCC. While the surface containing PEG bound less particles in most cases (Fig. 5.4 d) markers are above the dotted line), which suggests that indeed not all of the surface is covered with BSA due to the PEGylation. However, it did not prevent binding of our nano particles. In both cases, with PEG and BSA for passivation and with only BSA the number of bound particles is too high to meet the constrains for a solid phase synthesis of plasmon rulers.
The slides passivated with the reaction protocol from the Hugel group contain a small amount of biotin-PEG-silane to covalently bind molecules for a solid phase synthesis of plasmon rulers. We first tested the passivation with

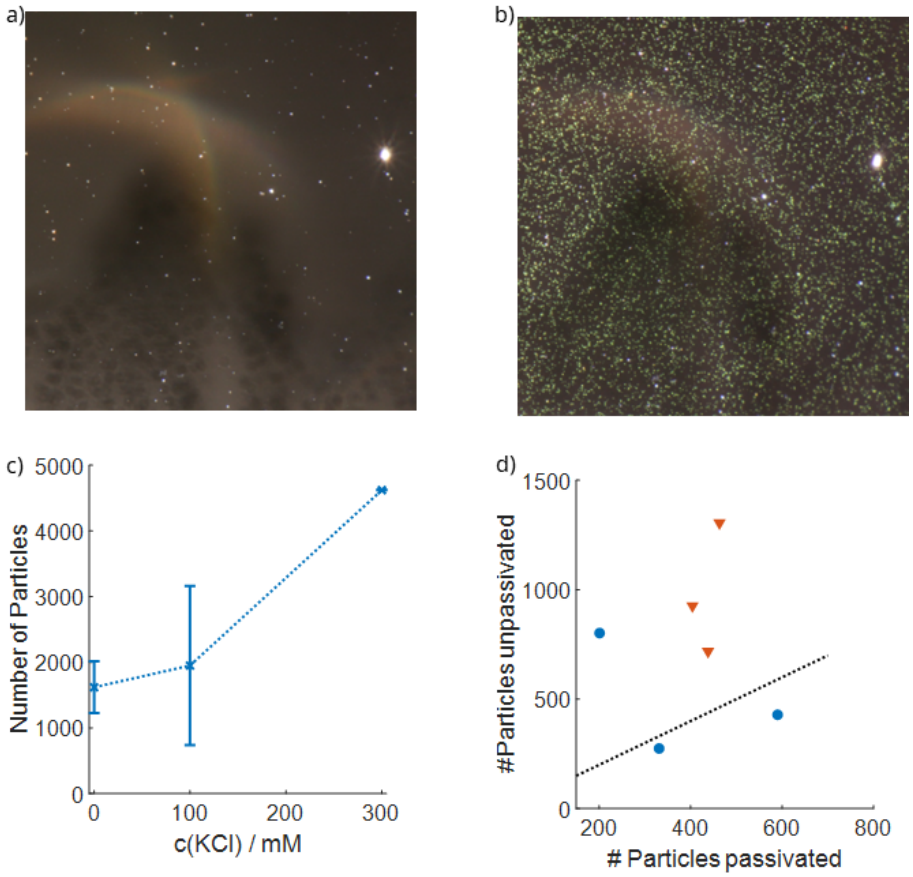

Figure 5.4: a) Section of a real color image of the passivated flowcell before treating with nanoparitcles. White bright scattering residues are visible in the whole field of view disturbing single particle experiments. b) Same section of the field of view after treating the surface with funtionalized gold nanoparticles. The surface is covered by thousand of particles which should not be binding to the surface, indicating either a failure of the reaction or interaction between particles and passivated surface. c) Number of particles binding to surface depending on the amount of potassium chloride used in the binding reaction of NHS-PEG-OMe to the APTMS surface. Average over three positions on the same surface were taken (cross) and errorbars calculated from standard deviation. For 300 mM data was only recorded for one positon, therefor no standard deviation is given. All Data shown did exclude BSA for co-passivation. d) Scatterplot for number of particles binding to the passivated and unpasisvated side of the flowcell for three positions in the cell in two different cells (colors and symbols) for 300 mM KCl and using BSA for copassivation. Dotted line with altitude of one is drawn for guidance.

nanoparticles functionalized with 10% amino-PEG. The test of the combined passivation of PEG and BSA resulted in single, unspecifically bound particles (Fig. 5.5 a). Using the same surface, we build plasmon rulers using the solid phase synthesis protocol from chapter 4 with reduced incubation times of 10 minutes because of the higher amount of amino groups present on the particles here. Figure 5.5 b) shows the particles bound to the surface via streptavidin and 5.5 c) the same field of view after assembly and measurement over night.

We discovered that the attachment of the particles to the surface proved to be unstable over a period of $12\,\mathrm{h}$, as seen by the circles in Figure 5.5 c) that do not surround a particle. Non-specific binding was observed on the surface, indicating that the BSA had detached from the surface, leaving open areas in the passivation layer. Since BSA was only deposited in the initial step and not included in our reaction solutions, it is possible that BSA was flushed out, leaving open spots for particles to deposit.

To prevent desorption of BSA from the surface during the assembly, one could include a small amount (tenth of the initial concentration) in each flushed in solvent. This would replenish detatched BSA on the surface and keep it passivated over multiple flushing steps. From literature it is known that BSA contains a reduced thiol from a cysteine (not in a bithiol bridge). Depending on the conformation of BSA this group might be able to react with the SMCC and bind to our nanoparticles. To determine if binding between BSA and the functionalized nanoparticles occurs, we incubated our particles with BSA and monitored the binding using gel electrophoresis.

Using our reaction components, we have observed that BSA binds covalently to particles that are functionalized with SMCC as seen by the change in migration distance (see Figure 5.5 d, dotted black and dotted blue marks). Since the migration distance was the same as for particles that bound HSP90, we concluded that the particles are fully covered with BSA when BSA is included in the reaction solutions. Particles that have already bound HSP90 and are then exposed to BSA do not bind additional BSA which can be seen from the same migration distance of both samples. Changes in the buffer does not alter the outcome (compare dotted and dashed markers in Figure 5.5) This experiment shows that BSA can not be used for co-passivation of the glass surfaces. If BSA is included in the solvents of the reaction it will also react with the binding sites we want to bind HSP90 to, and in turn block the reaction from happening. If no BSA is used in the reaction solvents non-specific binding occurs during the solid phase synthesis.

To overcome the binding of BSA to the nanoparticles during the reaction another chemical connection has to be used to bind HSP90 and the nanoparticles together. Examples for this could be using biotin-streptavidin, nickel-NTA, or using a BSA mutation without a free cysteine. Alternatives to BSA

that are commercially available are protein free blocking buffers which use polymer mixtures to passivate the surface against non-specific binding.

Lastly, if the cysteine on HSP90 were to be more accessible than the cysteine on BSA a particle functionalization that binds HSP90 but not BSA might exist. Only 10 % of the PEG chains on the particle carry maleimide groups (from the SMCC that binds to be amino groups on the particle), if those groups are bound to PEG chains shorter than the surrounding PEG chains with methoxy groups (non reactive) the binding site is "hidden" in a "crater" on the surface and only reactive towards the cysteine of HSP90.

5.6 Conclusion - Criteria for passivation

I investigated three different reaction protocols to prevent non-specific binding of gold nanoparticles to the glass substrate by silanization. For this, I set three criteria that the reaction must satisfy:

- No more than 1% of the total particles show non-specific binding,
- The reaction produces no light scattering residues,
- The possibility to introduce a binding site that stably holds particles in place for several hours.

None of the tested methods have been effective in creating a passivated surface dense enough to prevent nonspecific binding of nanoparticles. During our study of silanization degradation over time, we observed that the quality of the passivation remained constant for at least 5 weeks regardless of storage temperature, suggesting that storage of silanized surfaces is possible once a stable protocol is found. Two of the reaction protocols used co-passivation with BSA to cover any unreacted spots with the silane component. With the currently used particle functionalization and reaction strategy, which links HSP90 to the particle through the thiol group of cysteine, the nanoparticle can also attach to the free cysteine of BSA. Therefore, BSA is not a co-passivating agent but a binding site and cannot be used with the current reaction strategy.

The white scattering residues observed in our experiments are likely the result of silane components polymerizing, as noted in literature [76]. As the reaction carried out in toluene showed minimal residues, it may be necessary to use a solvent other than water to meet the specified requirements. Since the boro-silicate glass slides used are composed of mixed oxides, their surface is chemically heterogeneous. This variability varies among manufacturers, batches, the cleaning procedure, and storage conditions [76]. Therefor using a quartz glass surface might yield less variation from the silanization reaction due the ordered surface.

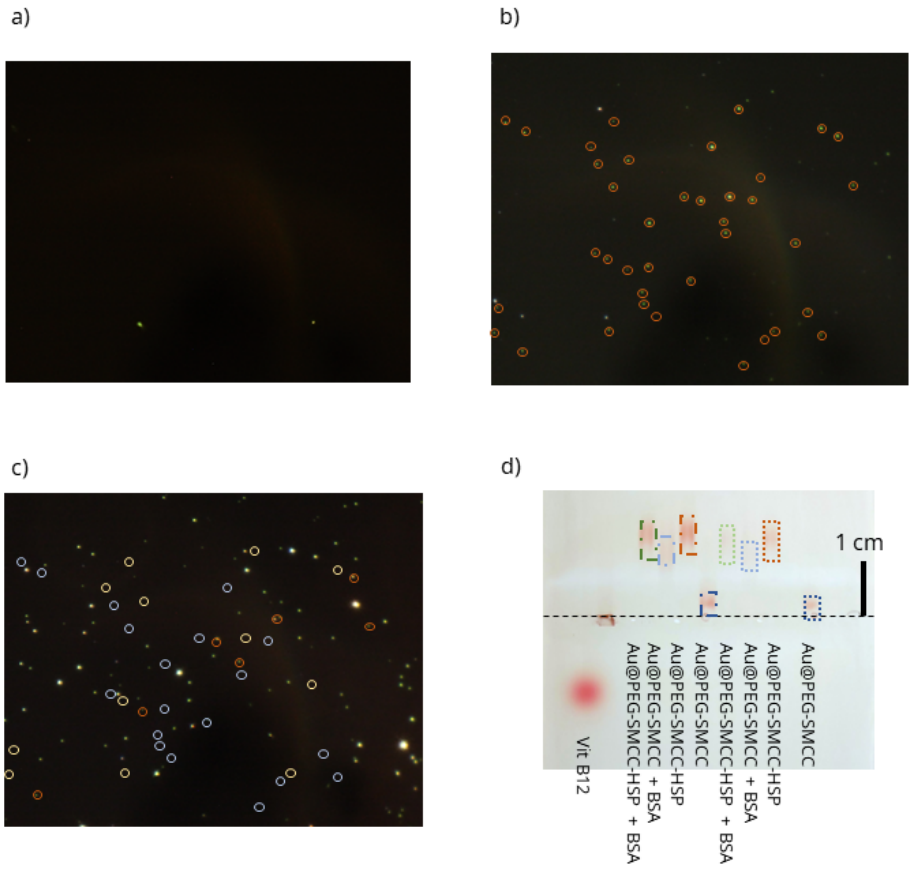

Figure 5.5: a) Real color image of a PEGylated and with BSA passivated surface after 30 min incubation with 10% AminoPEG – NP. Green dots are unspecifically bound nanoparticles b) Same field of view as a) after 30 min incubation with 10% amino-PEG and 3% biotin-NP . Orange circles are particles that remained on the surface from the initial binding, blue circles are spots where the particle unbound from the surface. Additional green dots are unspecifically bound nanoparticles c) Same field of view as b) 16 h later. Yellow circles show spots where particles unbound over night. d) Gel electrophoresis of nanoparticle from different states of the synthesis with and without BSA in different buffers. Dotted lines are particles in HEPES 7.4 buffer, dashed lines "conjugation buffer" (0.5M NaCl +TWEEN20 in buffer). Particles incubated with BSA (blue) show similar migration length as reaction with HSP90 (red) while no additional migration is seen for BSA incubation for particle covered with HSP90 (green).

To find a silanization method that meets the constraints of darkfield experiments with borosilicate glass sides, either the reaction protocol is kept the same and different glass slides (different batches from different manufacturers) are used. Or one batch of surfaces is used and the protocol altered. In both cases the hope is to find a surface whose chemical inhomogenity is overcome by the reaction conditions. I think the first method might have a chance for faster success as multiple slides can be used in the same reaction without the need for further parallelization of the reaction.
Alternatively, future work could avoid silanization altogether and use other non-covalent passivation agents such as polymers or BSA. To use BSA it should be explored which alternative binding and functionalization strategies exist for the nanoparticle to forgo linking HSP90 and particles via thiols.

Chapter 6

High yield batch synthesis reveals unknown states and decay channels in HSP90

An alternative way to the synthesizing plasmon rulers on a surface is the assembly in solution.

In this chapter, I present the results of the development of the batch synthesis of HSP90 plasmon rulers. First, I introduce the reaction protocol with a summary of the theoretical considerations made for the reaction as presented in chapter 3. I show that the synthesis produced HSP90 plasmon rulers repeatably for a given particle batch with higher yields than the previously used solid phase synthesis and discuss flaws and drawbacks of the reaction protocol. The presented synthesis allowed for higher experimental throughput due to the lower synthesis time compared to the solid phase synthesis of chapter 4. This required new evaluation tools to filter the recorded data. For this I developed and programmed a fluctuation filter and a visualization method that we called "heatmap". Both tools enables fast identification of time series with fluctuation between states and revealed that HSP90 shows more than the two known states from FRET and the previous plasmon ruler study. Evaluation of the time series with two states showed that the assumed model of three decay channels does not fit the recorded data. A model with five decay channels for the open and closed conformations shows the best fit for my experimental data. Additionally, I show that the HSP90 protein can populate more than the previously known two states. If those additional states are caused by more than one protein, the occurrence should be strongly correlated to the concentration used in the synthesis. I tested this hypothesis by lowering the concentration by five orders of magnitude. This did not influence the occurrence of time series with more than the known two states. From this I concluded that those are

rare states of a single HSP90 protein. Finally, I show that the high yield of the batch synthesis enabled me to see a rare loss of functionality of HSP90. In some time series the fluctuation between states changes to random fluctuations without distinct states. After some time the protein resumes its normal fluctuation. This phenomenon was recently reported for the monomer of the talin R3$^{\mathrm{IVIV}}$ domain and attributed to partial denaturation [77]. The investigation of this phenomenon in HSP90 is subject of futher studies.

In the work presented in this chapter, I designed the used synthesis, the experiments, did the evaluation of the data and designed the figures. The presented filter algorithm was developed and programmed by me. The heatmap visualization was developed in discussions with Carsten Sönnichsen and Thorsten Hugel. Experiments were conducted by Alexander Mielke, Florian Kolfer, Alena Kuzmina and me. Karl Wandner programmed the algorithm for the state identification, and Johannes Sutter synthesized the nanoparticles.

6.1 Batch synthesis protocol

For the formation of plasmon rulers in batch, there are two possible strategies to ensure the connection by a single protein. One way is to use different reactivities of the nanoparticles. It is possible to saturate one of the gold nanoparticles with the HSP90 protein and let this nanoparticle react with a second nanoparticle with a low amount (ideally one) of reactive sites. Alternatively, HSP90 can be used in deficit with particles with many binding sites. Here both nanoparticles are identical. HSP90 will react with the particles but leave most binding sites open for the following dimerization, as the protein diffuses faster than the particles. I decided to use the HSP90 protein as the limiting factor and use it in low concentrations instead of saturating one particle with HSP90. This allows for a reaction with fewer purification steps, since there is no excess protein that needs to be removed before the dimer formation. Refer to chapter 3 for further details on advantages and disadvantages of different reaction strategies.
For the nanoparticles, I used gold nanospheres with a diameter of $48\,\mathrm{nm}$ and functionalized them with a ratio of 40:60 HS-PEG-OMe : HS-PEG-NH_2 as this was the highest amount of amino-peg that produced reliably stable particles (see Figure D.1 in the appendix). Here, I present a shortened version of the developed reaction protocol (see appendix for a detailed protocol).

- Wash nanoparticles from stock solution once to remove surfactant, centrifuge again and remove supernatant
- Add double of the initial volume of PEG mixture with concentration of $10\,\mathrm{mmol\,L^{-1}}$ to the particle pallet

- Reaction over night at room temperature
- Wash $20\,\mu L$ with $100\,\mu L$ of buffer and then with $50\,\mu L$. Add $5\,\mu L$ TWEEN20 1% in each washing step.
- Re-suspend particles in $50\,\mu L$ buffer and add $5\,\mu L$ SMCC (concentration $1\,mg\,\mu L^{-1}$ in buffer)
- Let react for $10\,min$
- Add $5\,\mu L$ TWEEN20 1%, centrifuge and remove supernatant, then wash with $50\,\mu L$ buffer + $5\,\mu L$ TWEEN20 1%
- Remove supernatant, re-suspend in $30\,\mu L$ buffer, determine concentration[1], freeze in $2\,\mu L$ aliquots at $-80\,°C$ until use
- Add HSP90 in 1:1 ratio to particles, mix well
- Let react without shaking for $10\,min$
- Dilute for experiment

The total time needed for the synthesis starting from PEG functionalized nanoparticles amounts to about one to one and a half hour, which is significantly shorter than the required five hours for the solid-phase synthesis. The time required before recording of the time series was further reduced by storing small amounts ($2\,\mu L$) of SMCC functionalized nanoparticles so that only a known amount of HSP90 must be added. This shortened the time needed in preparation for a measurement to half an hour. This synthesis also does not involve a functionalized surface, which saves additional time.

6.2 New filters for fast plasmon ruler identification

The resulting increase in recorded data required new tools to filter the recorded data and identify time series with fluctuations from the large number of recorded time series (one experiment contains between 500 and 1000 individual time series). To overcome this challenge, I developed two software tools. A filter algorithm to reduce the amount of time series (see 6.2.1) to be viewed by the scientist and a visualization method, we called "heatmap" that allows for easier identification of states in a time series (see 6.2.2).

[1] Concentration of the gold nanoparticles was determined by the absorbance measured at $400\,nm$

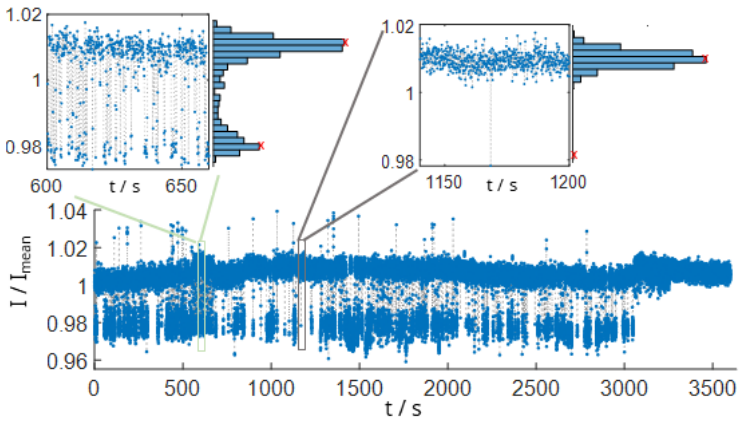

Figure 6.1: Example time series over one hour with fluctuation between two states. Insets show two sections of one minute length with a histogram of the intensity. Red crosses mark found maxima in the histogram.

6.2.1 Times series fluctuation filter

Fluctuations in the recorded intensities are the primary criterion for the identification of functional HSP90 plasmon rulers. In a drift free measurement the histogram over all intensities recorded gives the number of all visited states by the number of maxima in the histogram. Since drift cannot be fully excluded in experiments, I split the time series in multiple shorter pieces of $2\,\mathrm{min}$ each and took the histograms over the intensity in those. Figure 6.1 shows an example time series of one hour duration and $100\,\mathrm{ms}$ time resolution. The insets show two sections of the time series with the corresponding histogram. Red crosses mark the identifies maxima. In both sections two maxima were identified and therefore counted as parts of the time series with two states. The fraction of pieces with and without more than one maximum (one maximum means no fluctuation) gives the fraction of time with fluctuation. This fraction was used as a filter criterion and only time series that showed fluctuation in more than 30% of the pieces was further evaluated. All selected time series were checked manually for false positives where noise was identified as fluctuation between states. For a detailed discussion of the influence of the input variables "length of time piece" and "fraction of fluctuation", see chapter 7.

6.2.2 Heatmap visualization

Fast visible identification of the number and location of states was another need that arose from the large number of time series recorded. Figure 6.2 shows an example time series of $20\,\mathrm{h}$ duration with a time resolution of $30\,\mathrm{ms}$. Each datapoint is displayed as a small marker connected by a dotted

line. In this typical representation the number and location of states is not directly visible. To overcome this issue, we developed a tool that enables the direct identification of the number of states, their location and changes to population density over time, which we called "heatmap". For this we categorized the intensities recorded in the time series into 256 bins and then moved the histogram over the time series similarly to a moving average. We allocated the intensities in the window to the pre-allocated bins, which is shown in the yellow inset of figure 6.2. The counts per bin were color coded in a logarithmic color scale and put back together as a time series (green inset in figure 6.2). As seen in figure 6.2 the number of states is more visible in the heatmap than in a plot using markers for each recorded data point in the top of the figure. In the recorded time series each state is correlated to a minimum in the energy landscape of the possible conformations. The longer one state is populated the deeper the minimum is which means is rarer to overcome the energy barrier [2]. The logarithmic color scale of the heatmap therefore directly visualized the relative depth (by deepness of color) for the taken conformations.

6.3 Batch synthesis achieved higher yield than flowcell synthesis

As I have shown in chapter 4 the yield of plasmon rulers was too low with the solid phase synthesis. To study rare phenomea in protein dynamics it is essential to have a more than single plasmon rulers in a single experiment. This reduces the influence of variations between experiments and leads to more robust data. Therefore, I developed a batch synthesis which I describes in chapter 6.1. With the presented synthesis protocol we conducted experiments with the HSP90 protein. To evaluate the performance of the reaction, I used the number of functional plasmon rulers like in the evaluation of the solid phase synthesis. Since with a batch synthesis the reaction happens outside of the flowcell, there is no state before and after dimerization. Thus we cannot use the characteristic change of resonance wavelength and scattering intensity for the identification of dimers.

For the identification of fluctuations in the time series, I used the beforementioned fluctuation filter with a cutoff limit of 30%. Figure 6.3 a shows the fraction of experiments that did yield any time series with fluctuations according to the filter criterion and visual filtering by me. With the set filter criteria only singular time series per experiment were falsely identified as

[2] The activation energy E_A which gives the height of a energy barrier for a chemical process is given by the Arrhenius equation: $k = A \cdot e^{-\frac{E_A}{RT}}$. A is the Arrhenius factor, T is the temperature, R is the universal gas constant, and k is the rate of the process.

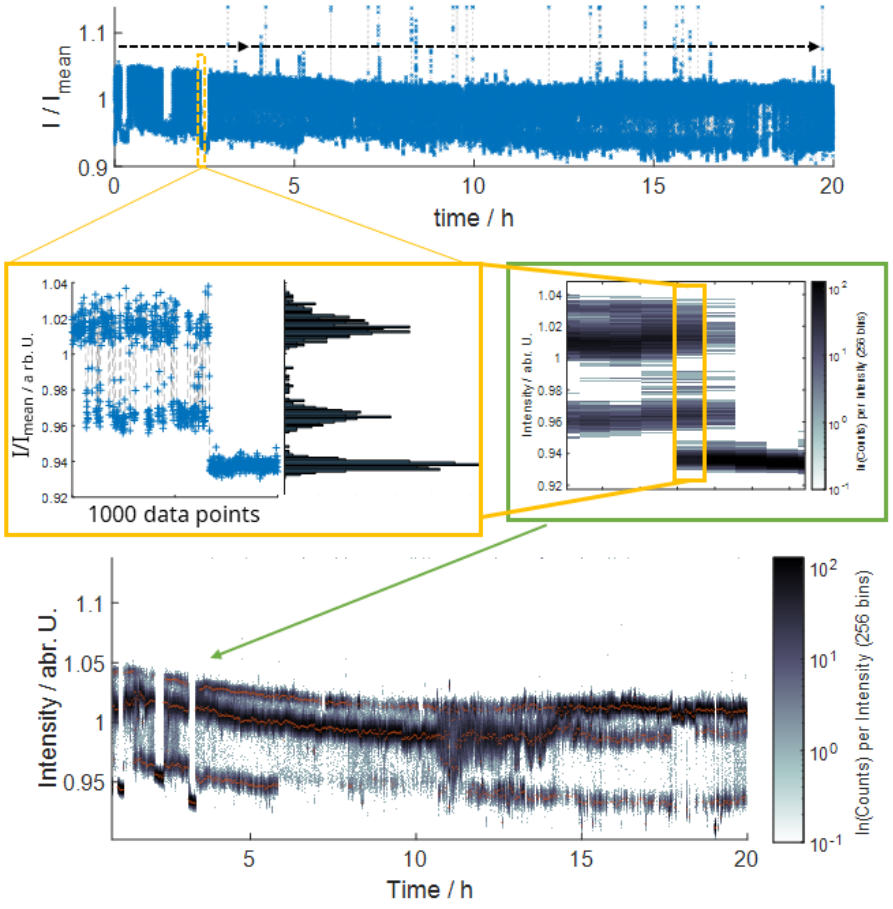

Figure 6.2: Working principle of the heatmap visualization. Top shows a $20\,\mathrm{h}$ time series recorded with a time resolution of $30\,\mathrm{ms}$. In the plot with cross markers for each data point, the number and location of the visited states is not visible. Insets show one sections of the time series with $30\,\mathrm{s}$ length and corresponding histograms in the 256 bins. The counts per histogram bin are color coded for each section (yellow frame). This is repeated in steps of 500 data points over the time series and the colored counts per histogram recombined into a full time series. The red frame shows a the zoomed in section of the time series with section of the yellow inset marked in yellow. Bottom shows the final heatmap with four directly visible states. Orange crosses mark maxima of the histograms of each section.

plasmon rulers (see B for detail on the filter performance). Almost ninety percent of the experiments showed at least one time series with fluctuations between states. Since I randomly deposit the particles on the surface, I cannot control the number of particles in my experiments. To compare the yield between experiments, I used the relative value (normalized to total amount of particles in the field of view). Figure 6.3 b shows the relative yield for the different experiments as well as the absolute number as a color code. The majority of experiments showed fluctuation in less than four percent of all particles. An average of 13 ± 16 fluctuents were found over the experiments. The synthesis shows a large variation in the absolute number of fluctuents. Additionally, the majority of experiments yielded below 4% plasmon rulers. The experiments shown here were conducted by different persons and with different batches of functionalized nanoparticles. While the protocol for the functionalization was the same each time, pipetting errors and small differences in the removal of suprenatant influence the concentration of the nanoparticles and reactants. This in turn alters the important ratio of HSP90 to nanoparticle in the final assembly step. The small differences strongly influence the yield of plasmon rulers as is evident by the divergence in figure 6.3 b.

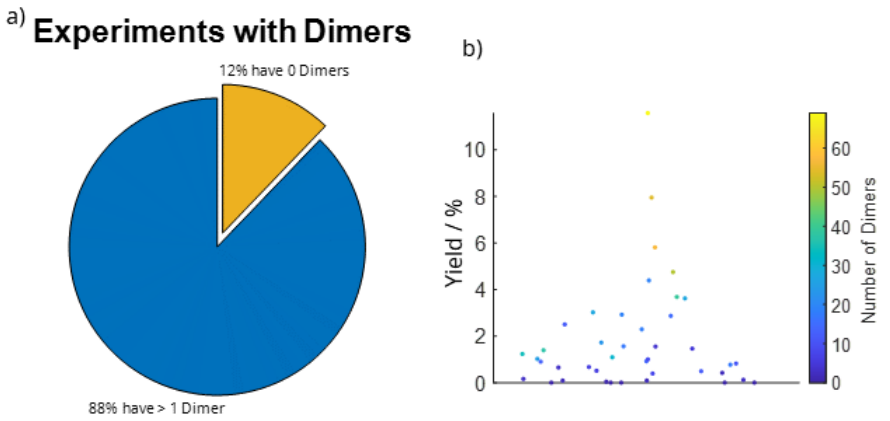

Figure 6.3: a) Pie chart of experiments with and without dimers. Blue part shows fraction with at least one time series with fluctuation between at least two states. b) Swarm plot of dimer yield of experiments calculated as fraction of total particles. Color bar shows the absolute number of time series with fluctuation between states.

The consistency achieved in the synthesis with the used batch of particles surpasses the solid phase synthesis. There one-third of the experiments showed fluctomers, whereas here nearly ninety percent do. The average yield is an order of magnitude higher but still varies between the experiments. For most of the experiments, stored particles have been used to

avoid variation from different functionalization batches, but over the course of this thesis, multiple functionalization batches were prepared, stored and used. From experience in our group we know that the functionalization of nanoparticles varies even when using the same protocol. Therefore, I hypothesize that this is the largest source of variation. Since we did not use a functionalization of the glass surface for the experiments the formed plasmon rulers can stick with both particles to the surface. As mentioned before we cannot identify non-fluctuating plasmon rulers. Therefore, the yield might change between experiments because of the random orientation of the formed plasmon rulers on the glass.

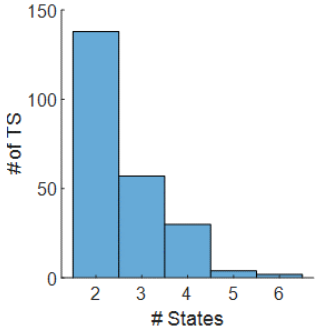

Figure 6.4: Histogram over the amount of states found in time series of HSP90. Data combined from 232 time series. All time series stopped fluctuation after addition of AMP-PNP, ensuring that fluctuations were caused by HSP90.

Although this protocol was used to successfully synthesize plasmon rulers with a yield of up to ten percent of functional HSP90 plasmon rulers in one experiment (calculated to the total of all particles), it has some clear flaws. The dilution used in both the washing after the PEGylation and after the reaction with SMCC is insufficient and leaves a significant amount of unreacted species. The PEGylation is carried out with a concentration of $10\,\mathrm{mmol\,L^{-1}}$ and the stock concentration of the nanoparticles was measured to be $0.08\,\mathrm{nmol\,L^{-1}}$. For the purification the nanoparticles are centrifuged and form a small pallet from which the supernatant can be removed. Assuming that the remaining nanoparticle pallet is small and the supernatant is carefully removed, the volume of the pallet for this example is estimated to have a volume of $1\,\mu\mathrm{L}$. The remaining PEG concentration after the first dilution and washing is then $0.095\,\mathrm{mmol\,L^{-1}}$, after in the pallet the second washing step $0.0019\,\mathrm{mmol\,L^{-1}}$. After re-suspension in $50\,\mu\mathrm{L}$ buffer for the reaction with SMCC, the concentration of PEG in the solution is $0.000\,038\,\mathrm{mmol\,L^{-1}} = 3.8\,\mathrm{nmol\,L^{-1}}$ and therefore multiple times higher than the particle concentration. Therefore, residues of the different reaction steps remain in the solution and can react in the next step. Second, the synthesis was found to be sensitive to the particle batch used.

I used particles that were prepared by Johannes Sutter in our group and stored particles after the reaction with SMCC in a freezer (at $-80\,^{\circ}\mathrm{C}$) until further use. After the particle batch was fully used up, the reaction protocol did not produce any functional plasmon rulers. Gaining a deeper understanding of why the reaction worked, despite the observed error

sources and the influence of the particle batch, is the subject of ongoing research.

More than two states found for HSP90 time series In the analysis of the recorded time series we found that some show more than the known two states from previous HSP90 studies. Over different recording length we saw three and sometimes more distinct states in the time series. An example of a time series with four states on a $24\,\mathrm{h}$ time scale is shown in figure 6.2, and additional examples with three and four states are shown in figure 6.5.

Time series showing three states are rarer than time series with two states. Out of 232 time series 60 showed three states compared to 140 with two states. Additionally more than three states were observed with increased rarity (refer to figure 6.4). The data shown in figure 6.4 are from 232 time series where all fluctuations stopped after the addition of AMP-PNP which is known to lock HSP90 in the closed conformation. Therefore, I assume that the states are caused by different conformations in HSP90. An investigation into whether the increasing number of states is caused by one or multiple HSP90 proteins is presented later in this chapter.

6.4 Additional decay times found in HSP90 time series

The analysis of the recorded time series is separated by the number of states present. First, I evaluated the dwell times and resulting decay times for time series with two states as those were also seen in previous plasmon ruler experiments [8].

Because of the polydispersity of the nanoparticles and the differences in the particle volume that result from this, the scattering cross section for the formed plasmon rulers varies[3]. For a comparison, each time series is normalized to the mean intensity. The resulting relative intensity can be compared without influence of higher or lower overall scattering intensity. Data points that are further than seven times the standard deviation apart from the average intensity are deemed outliers and replaced with the average value of the left and right data points of the outlier. For time series where the present drift caused the state allocation to fail, a correction was made with the signal of the closest particle without fluctuation. This correction was not done with the average signal of all particles since any global phenomena are captured by all particles. Local drift, on the other hand, is not and therefore averaged out when correcting with only the global trend, resulting in an incomplete correction of the drift.

[3] The scattering cross section c_{sca} determines how much light is scattered and is proportional to V^2 of the nanoparticle.

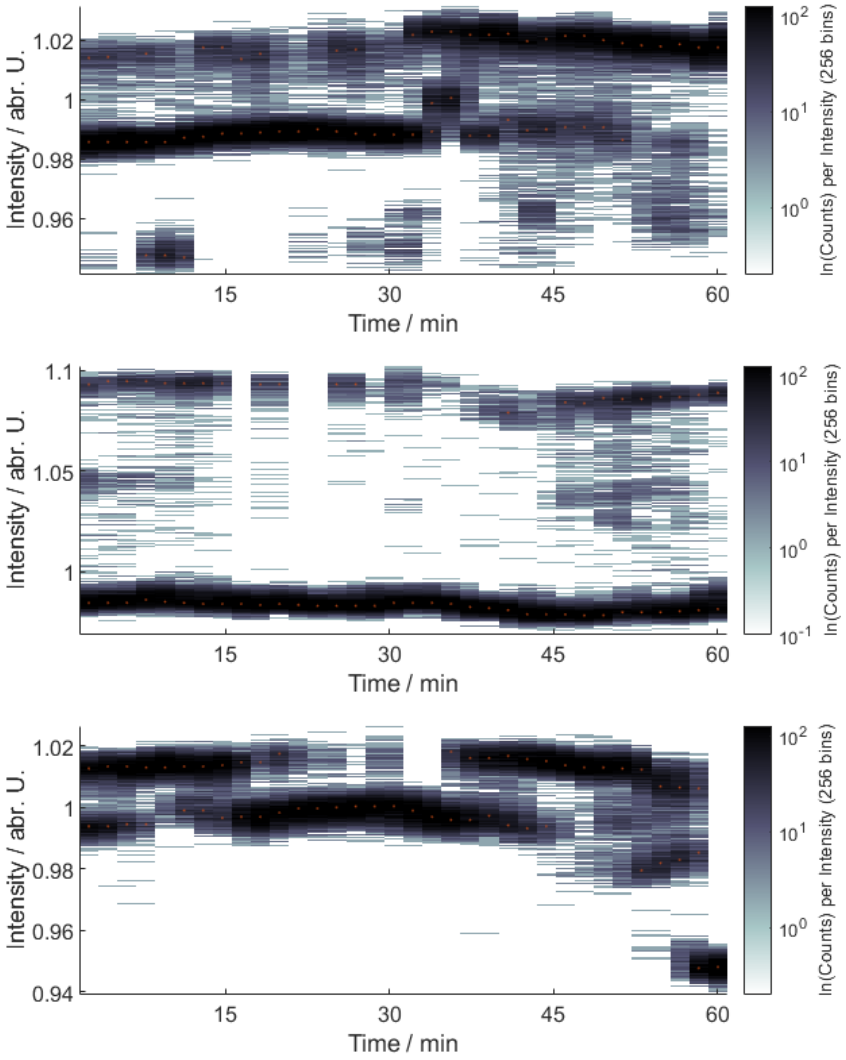

Figure 6.5: Heatmap of time series with more than two states. Top two time series show three states with different prominence, bottom shows four states. All time series are from the same experiment and were recorded with a time resolution of $100\,\mathrm{ms}$.

For the extraction of dwell times, I used a different algorithm than my predecessors. Since the recorded data also show more than two states, the previously used threshold algorithm cannot be used[4]. The statefinder

[4]Previously a MATLAB inbuild function *pulsewidth* was used. This function can only handle a bi-level signal.

algorithm works in multiple steps. First the data undergoes denoising with a total variance denoising algorithm [78]. The resulting step signal consists of multiple steps with varying length (dwell time) and intensity levels. The user can define a minimal length and level difference which each step has to conform to. I set the minimal length to two data points since a single data point could also be an outlier. The minimal difference between the states was set according to the intensity levels of the individual time series until a visually best identification of the states was achieved. In a last step the level and length of each step is saved for further evaluations. The statefinder algorithm was programmed by Karl Wander and used for the evaluation of all time series. For more details on the function of this algorithm see chapter 7.

Figure 6.6 shows two example time series with different signal to noise ratios and different degrees of drift. The data points are colored according to the allocated state. The used code is able to identify present states for both cases. For the time series with drift (figure 6.6 bottom) detrending would have been required to be used for a threshold algorithm to correctly allocate the data points to each state. Also visible are some overlaps of the colored markers, which indicates that the algorithm did not correctly assign the data point to the state. I evaluated the performance of the statefinder algorithm for my data and found that the wrongly allocated states do not influence the extracted decay times for time series with two states (refer to chapter 7 for the evaluation).

I evaluated and extracted 59,800 dwell times from 140 time series of one hour length. All used time series stopped fluctuation after incubation with AMP-PNP as known for the HSP90 plasmon ruler experiments. To determine the decay times from the dwell time distribution I used exponential sum fitting which is used to describe the decay behaviour of single ion channel experiments and other phenomena in nature [79–84]. The formula used was formulated by Sigworth and Sine [85].

$$\sqrt{c} = \sum_{i=1}^{n} a_i \cdot exp[t - \tau_i \cdot exp(t - \tau_i)] \tag{6.1}$$

Here t is the time , τ_i the decay constant of decay channel *i* and c the amount of dwell times in the histogram bin of time t. A is a scaling factor. The dwell times of each state are logarithmicly binned which allows plots of multiple orders of magnitude in time, that are still easily readable [84, 85]. It also reduces computational time for fitting of the exponential function, as the calculation time mainly depends on the number of bins. With the used formula of Sigworth and Sine, plotting the square root of dwell times per bin versus ln(t) the resulting decay time of each channel is given by the x location of the maximum of each individual function.
For HSP90 three decay channels are currently known. Using equation 6.1 with three decay channels (n = 3) and fitting the function to the dwell time

distribution of both states did not result in an overlap of experimental data and fit function as seen in figure 6.6 b and c. Specifically the long and rare dwell times are not represented by a fit with three decay channels. Since the model of three decay channels does not match the recorded data, I expanded the number of possible decay channels. The two free parameters in this evaluation are the width of the bin and the number of decay channels. I used the adjusted coefficient of determination R^2, which is a measure for the correlation of the fit and the experimental data. Adjusted R^2 was used due to the penalty imposed when using more fit parameters[5]. In figure 6.7 I plotted R_2 against the bin width and number of decay channels which were used for the fit function. As reported by *Sigworth* the fit quality is mostly independent of the width of the used bins [85].

Table 6.1: Maximum R^2 for each number of fitted decay channels

channels	R^2_{open}	R^2_{closed}
2	0.758	0.769
3	0.908	0.894
4	0.941	0.945
5	0.944	0.951
6	0.943	0.944

When decreasing the number of decay channels in the fit below four the fit accuracy decreases compared to fitting with more decay channels. This further indicates that there are additional, previously unknown decay channels present (see table 6.1). While the maximum fit accuracy (maximum of R^2 was reached for fits with five decay channels for both states, the difference in R^2 is small between fits with four, five and six channels. Especially for the open conformation (lower state) the difference in fit accuracy is in the third decimal place. For both open and close conformation I investigated the fit of four to six decay channels. A fit with four decay channels does not include rare dwell times with high length ($\ln(\tau > 6)$) for both states. For the state representing the closed conformation of HSP90, a fit with six decay channels fits a decay channel for higher times than the recorded data and is therefore not further taken into account. For the open conformation, there is no visible difference for a fit with five and six decay channels. Due to these reasons I decided to use the fitted model of five decay channels for both states.

I tested whether the determined decay times are present in all recorded time series by fitting the dwell times of each time series individually with the model of five decay channels. I compared the average of the resulting decay times with the previously determined decay times from the combination of all dwell times. Figure 6.9 shows that the decay times connected with long dwell times and especially the longest determined decay time can't be extracted from averaging, as the average determined decay time is orders of magnitude larger than the experimental time. These errors likely occur because not each time series shows all decay times. The long decay times

[5] Using more parameters to fit data will improve the fit accuracy but may not represent the reality. Therefore, the model with the least number of parameters should be applied.

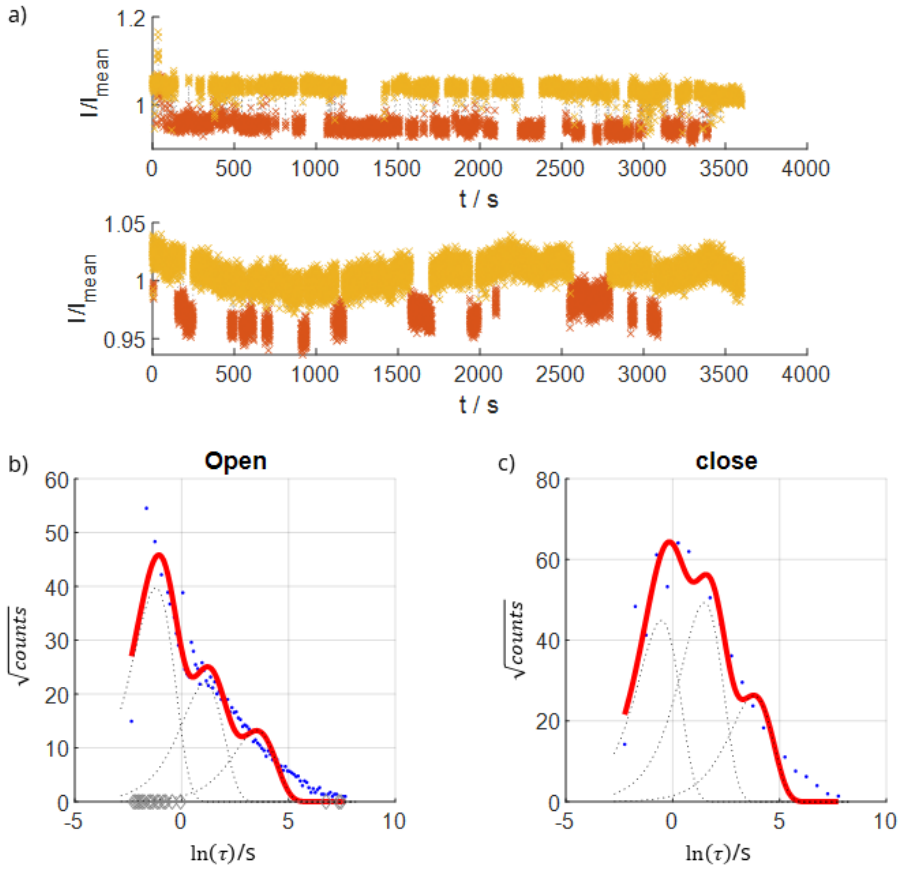

Figure 6.6: a) Example time series with two states colored as identified by statefinder algorithm. Top: time series with signal to noise of above one with no longterm noise. Bottom: time series with signal to noise of ca. one and wavelike long-term noise. Both time series are from the same experiment. b) Logarithmic binned histogram of dwelltimes of the open conformation with the previously known three channel model, using squareroot of counts on y scale for better visibility. Curve fitted with linear combinations (red line) of individual decay channels (dotted lines). Diamonds indicate histogram bins without data and were excluded for fitting. c) Logarithmic binned histogram of dwell times of the closed conformation with the previously known three-channel model using squareroot of counts on y scale for better visibility. Curve fitted with linear combinations (red line) of individual decay channels (dotted lines). Diamonds indicate histogram bins without data and were excluded for fitting.

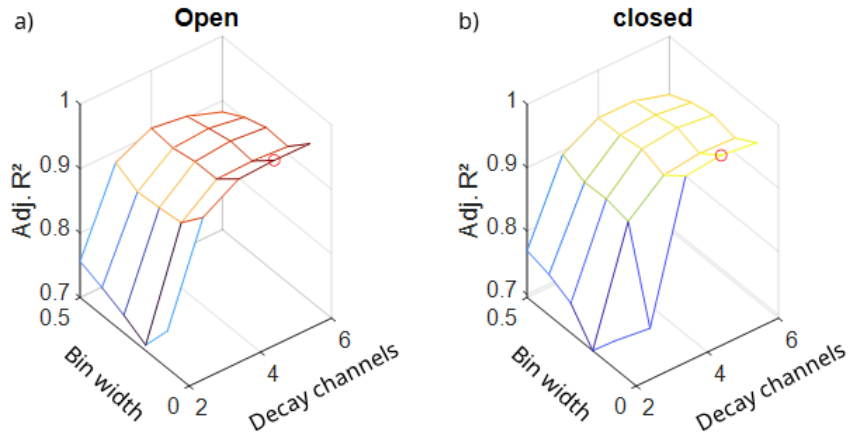

Figure 6.7: Surface plot of the R^2 adjusted by the number of fit parameters against bin width and number of decay channels for the open (lower intensity in time series) conformation on the left and closed (higher intensity in the time series) conformation on the right. For both an optimal fit was obtained with five decay channels as marked by the red circle.

are rare and fitting a model to data without the long decay time causes errors which result the overly large decay time.

If the dynamics of HSP90 were ergodic[6] on this time scale one would expect that the average over all dwell times from all time series would result in the same decay times as from a single time series. This only the case for the three lowest decay times which still have a large relative error when averaging over all time series (see table 6.2). This matches results of the previous HSP90 plasmon ruler study where over $24\,\mathrm{h}$ the population probability did not converge which indicated breaking of ergodicity.

Comparing the determined decay times with the previously reported ones shows that there is an overall good agreement between the decay times. The long decay time in the 100 to 200 second range for the closed conformation shows the largest deviation. In the study of 2018 the first two decay times were determined from a double exponential decay function and the third from a linear fit to the cumulative dwell time distribution ([8] supporting information). In this thesis I used sum exponential fitting to extract all decay times. The differences in extraction method as well as the amount of dwell times used (here 59,800, in [8] 27,700) might explain the difference as the long dwell times are rare and therefore offer little data points for the fit.

[6] Ergodicity means that the average over a long time and a large sample of shorter times converge to the same result.

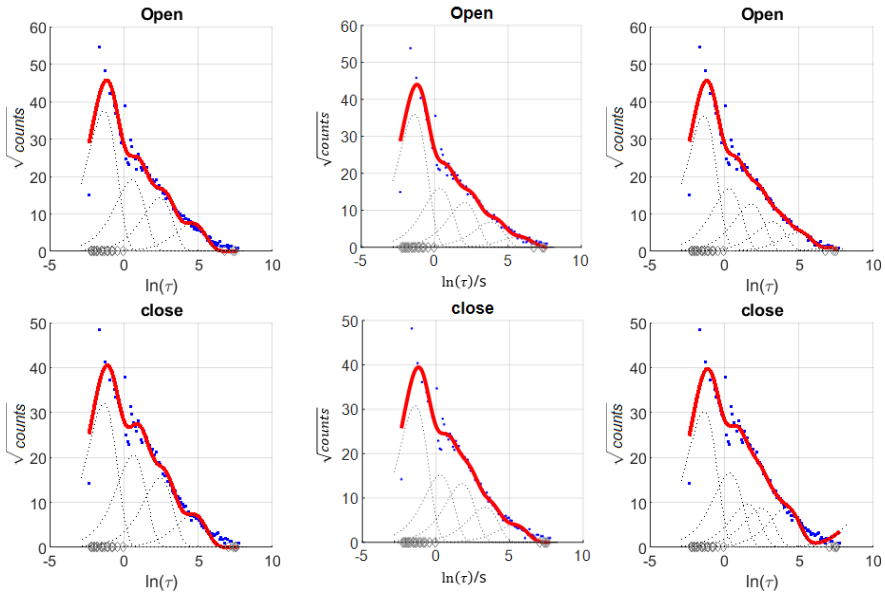

Figure 6.8: Logarithmic binned histogram of dwell times (in seconds) with bin width of 0.1. Using square root of counts on y scale for better visibility. Curve fitted with linear combination (red line) of individual decay channels (dotted lines). From left to right, four, five and six decay channels are fitted to the dwell times distribution of the open conformation of HSP90 (top) and the closed conformation (bottom). When fitting four decay channels, long dwell times are not represented by the fit function. Fitting the six decay channels to the dwell time distribution of the closed conformation introduces a decay channel outside of the experimental data.

Table 6.2: Comparison between extracted decay times for HSP90 from single one hour time series, combining 59,800 dwell times from said one hour time series and from previous plasmon ruler experiments from [8]. The decay times four and five of the averaging are not shown due to the large error of more than 200%. Errors of the combined evaluation of dwell times is derived from the 95% confidence interval of the fit and given as the standard error.

	τ_1	τ_2	τ_3	τ_4	τ_5
Open state $\bar{\tau_n}$	0.4 ± 0.3	2 ± 2	10 ± 20	-	-
Closed state $\bar{\tau_n}$	0.4 ± 0.3	2 ± 2	10 ± 10	-	-
Open state $\tau_{n,combined}$	0.25 ± 0.02	1.5 ± 0.3	8 ± 2	40 ± 20	300 ± 100
Closed state $\tau_{n,combined}$	0.25 ± 0.02	1.4 ± 0.3	7 ± 2	40 ± 10	300 ± 100
Open state $\tau_{n,2018}$	-	1.63 ± 0.03	13.2 ± 0.06	-	340 ± 70
Closed state $\tau_{n,2018}$	-	0.78 ± 0.02	4.3 ± 0.1	-	115 ± 9

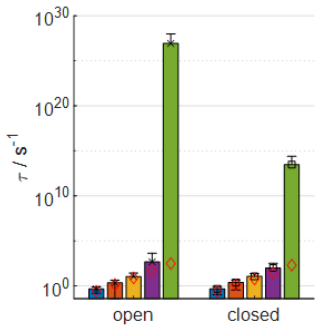

Figure 6.9: Bar plot comparing the decay times from fitting the a 5 decay channel model to the dwell times of individual time series (bar height) and combining all dwell times and then fitting the decay times (red diamonds).

Additionally there are two previously unknown decay time present. One in the sub one second range and one in the half minute to minute range. The short decay time is close to the used exposure time of $0.1\,\mathrm{s}$ and the set limit of decay times of $0.2\,\mathrm{s}$. To ensure this decay time is not an artifact, additional experiments should be made for exposure times lower than the here used $100\,\mathrm{ms}$. The previously reported decay times matched with reports for FRET experiments on HSP90. Since in this study I found matching decay times, using a different evaluation method, it makes it plausible that the newly found decay times also originate from the dynamics of a single HSP90 protein.

6.5 Occurance of more than two stated independent of HSP90 concentration

In the recorded time series of HSP90 dynamics I also found that a significant portion of the time series with fluctua-

tions between states visit more than two (see figure 6.4 and figure 6.10 a for an example time series). This is in contrast to the known data. As stated in chapter 3 the reaction in free diffusion can yield different byproducts. For example the formed plasmon ruler could be moved by another HSP90 against the surface. Glass has a higher refractive index than water and therefore a distance change will induce a small resonance and intensity shift. For a single nanoparticle I did BEM[7] simulations to evaluate the change in scattering intensity (see figure A.3 in the appendix). The scattering intensity for the used illumination bandwidth of the LED amounted to ca. 1.5% which matches with some of the recorded state differences of ca. 2%.

A second possibility is the formation of trimers, where one particle bound two other via a single HSP90. Here the final signal also depends on the orientation of the particles to each other as also higher order coupling can occur depending on the distance of all particles to each other. In both hypothesis the signal originates from more than one HSP90. To test this hypothesis I designed experiments where the used HSP90 concentration is reduced by multiple orders of magnitude. The reduction in HSP90 concentration reduces the probability for a particle to carry more than one protein faster with decreasing concentration than it does for a single protein. If the additional states are caused by more than one HSP90 this would result in a reduction of overall yield of formed dimers but relative increase of time series with two states. In the experiments conducted by Alena Kuzmina, we did not see the expected trend. For the resulting yield we see an increase with the reduction of used HSP90 concentration (see figure 6.10 b). The experiment done with $2.4 \cdot 10^{-5}\mathrm{nmol\,L^{-1}}$ showed a much lower yield than the other experiments. We noticed that the yield depends on the side of the microfluidic channel that is used for the measurement. On the upper side the yield is lower than on the bottom side (figure 6.10 b). Since the formed plasmon rulers are heavier than single particles they diffuse downward and are less likely to stick to the top surface than to the bottom. Because we typically conduct measurements on the side with the darkfield condensor[8] and used one upright and one inverted microscope the used side varied between the two microscopy setups. However, the increase of yield of fluctuating time series when decreasing the used HSP90 concentration is contradicting to the initial assumptions. This could indicate that the determined nanoparticle concentration was too high and therefore the used amount of HSP90 was also too high. The nanoparticle concentration was determined by measuring the absorbance at $400\,\mathrm{nm}$ which is correlated to the number of gold atoms and therefore the amount of gold in the sample. Due to the low particle concentration the noise in the measured absorbance introduces error is the following calculation of the particle concentration. The determination of the concentration dependency of the synthesis should

[7] Boudary element method is a numerical calculation method to solve the maxwell equations for a "net" of boundary triangles to approximate the spectral properties.

[8] This side has a better signal to noise ratio due to the lower recorded background.

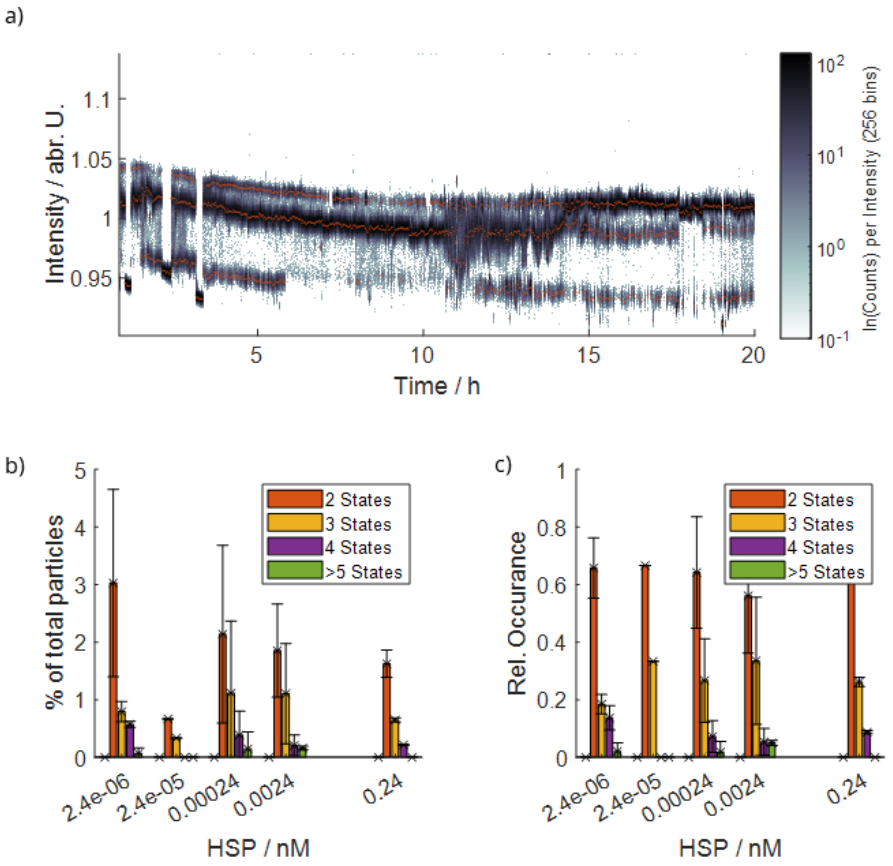

Figure 6.10: Dependency of yield and number of states on HSP90 concentration. a: Example time series with four states over $20\,\mathrm{h}$ recorded with time resolution of $0.1\,\mathrm{s}$. b: Dependency of yield of time series with each state versus used HSP90 concentration. Lower concentrations slightly increase the yield. b: Relative occurrence of state numbers versus HSP90 concentration. The occurrence of state numbers above the known two states is independent of the used HSP90 concentration.

be further investigated in future studies together with higher concentrated samples of nanoparticles to reduce errors in the concentration determination.
In the relative occurrence of the number of states in the recorded time series, a trend is not visible. The time series with two states made up around seventy percent of all time series that were identified as fluctuating in intensity. While there might be an indication that the relative occurrence for time series with three states decreases with decreasing concentration of HSP90, time series with four states increased in relative occurrence. Therefore, no trend for the relative occurrence can be identified from the conducted experiments. We excluded the possibility that the signals are artifacts and not caused by HSP90 at all due to a control experiment with the same particle batch and protocol but without HSP90. This experiment showed two time series with fluctuations between states (see figure 4.5 in the appendix). However, the number of plasmon rulers formed in the synthesis with HSP90 is an order of magnitude larger and thus these artifacts should not influence the evaluation of dwell times. The lack of correlation between the number of states in the time series and the amount of HSP90 indicates that these time series are derived from a single protein and not from multiple ones.

For the investigation of time series with more than two states, I evaluated the performance of the state finder algorithm for those time series. I used the same data set from a single experiment which contained twelve time series with three states and six with four states and the same testing method as for two state time series (see chapter 7). Here I found that the time series with more than two states are much more prone to wrong allocation of states (refer to figure 7.9 for a histogram over the percentage of wrongly allocated states per time series). For both cases, the average percentage of wrongly allocated states is around ten percent. Therefore, I did not evaluate the dwell times and resulting decay times for those time series, as extracted dwell times might not represent the experimental data. However the percentages of wrongly allocated states might not show the full picture. Since the total time of the time series is the same as for the two state time series ($1\,\mathrm{h}$) there is less relative time that can be spent per state. Therefore, a lower number of wrongly allocated states results in a higher percentage of wrongly allocated states. Secondly the difficulty in allocation seems not to be homogeneous across the time series as seen in the inset of figure 7.9. The wrong allocation of the lowest intensity level state in the shown four state time series occurs shortly before the end of the experiment. The majority of

Table 6.3: Average percentage of wrongly allocated states in time series with three and four states.

State	3 states	4 states
1	10 ± 8%	8 ± 12%
2	15 ± 17%	19 ± 24%
3	8 ± 13 %	8 ± 8%
4	-	8 ± 18%

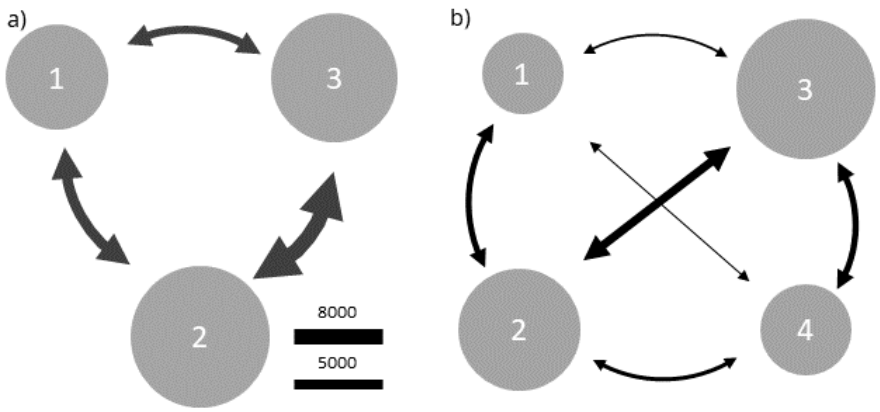

Figure 6.11: a) Transition diagram for time series with three states. The arrow thickness indicates the number of transitions, while the sphere size shows the relative occurrence of the state. b) Transition diagram for time series with four states. Arrow-thickness indicates number of transitions, while sphere size shows relative occurrence of state

the time series shows correct allocation of states three and four and could be used for evaluation. A detailed discussion on the chosen classification algorithm and potential improvements can be found in chapter 7.
I also investigated the transitions between each state, which shows hints that the transition between lowest and highest states most often passes all intermediate states. The further apart the states are in intensity the less likely it is for a direct transition to occur. Note that due to the previously discussed errors in state allocation all transitions and state occurrences have an error of approximately 10%.

6.6 We see disordered parts in time series

The high amount of time series recorded and the heatmap made another phenomenon visible. We found that in some parts during the experiment the time series loses the fluctuation between states and goes into random noise (see figure 6.12) for examples) The duration of this phenomenon differs between different point in one time series and the protein resumes the fluctuation afterwards.

In a recent study on the dynamics of a single protein, this phenomenon was also reported [77]. The authors hypothesized that this behaviour is linked to the loss of the tertiary structure. This means that the HSP90 would partially denature and refold into the correct structure and resume its dynamics. This behaviour in HSP90 was previously not recorded.

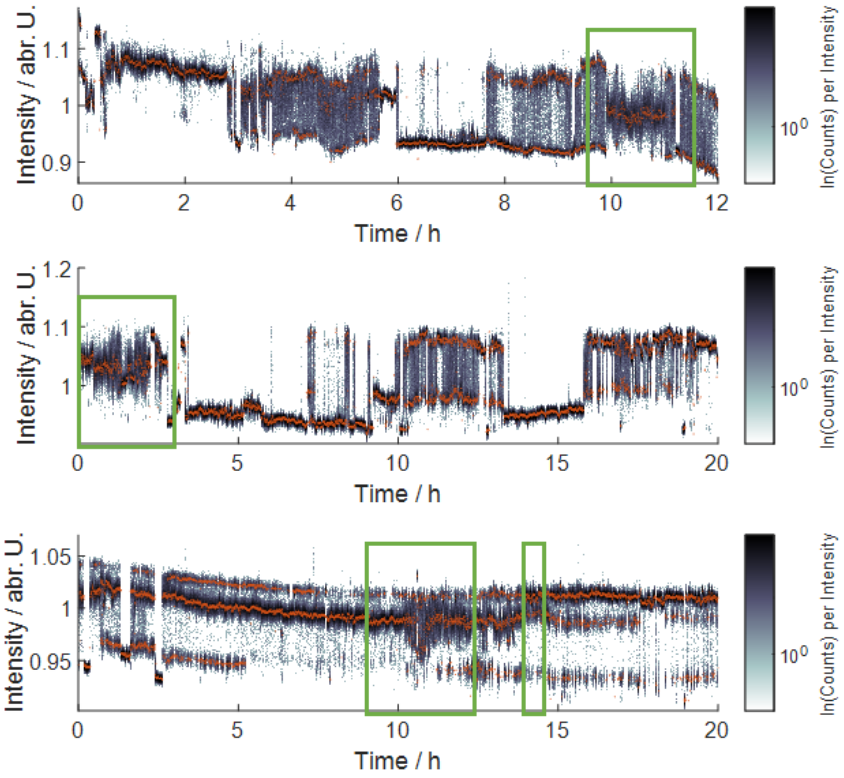

Figure 6.12: Example time series of different length in the heatmap visualization. HSP90 time series sometimes show loss of distinct states in the signal and resume fluctuation between states afterwards. Areas are marked by green rectangles

6.7 Summary

I developed a new batch synthesis for HSP90 plasmon rulers, which overcame the previously low yield of functional plasmon rulers and the need for a functionalized surface. The synthesis uses particles functionalized with amino-PEG and SMCC and HSP90 in deficiency to control the reaction towards single protein links between two nanoparticles. The yield of functional plasmon rulers reached a maximum of ten percent of all particles in the field of view in the evaluated experiments. Preparation time was also reduced to about half an hour compared to five for the previous solid-phase synthesis.

The resulting higher number of recorded HSP90 time series required new filter tools. For this, I developed a new filter tool that identifies fluctuations between states in the recorded time series. This reduces the amount of experimental data that the scientist can view and speeds up the evaluation. The second tool I developed is a "heatmap" that makes the number and location of states in the time series directly visible, which otherwise is difficult, especially for long time series of ten hours or more.
I evaluated a total of 232 individual time series (á $1\,\mathrm{h}$ duration) of HSP90 and found that, in addition to the known two states, half of the recorded time series showed more than two states. In this chapter, I showed that these time series are not an artifact but caused by a single HSP90 protein, as the occurrence does not scale with the used concentration of HSP90 and does stop after the addition of AMP-PNP. Evaluation of the time series with the known two state revealed that the assumed model of three decay channels does not fit with the here presented data. I optimized a sum exponential fitting routine to find the number of decay channels that best fit my recorded data. This resulted in a model of five decay channels for both the open and closed conformation. The extracted decay times include the previously reported decay times from the three state model and two new decay times. One in the sub one second range and one on the time scale of half a minute to a minute. For the time series with more than two states I showed that the transitions are rarer the more states have to be skipped in the transition. Due to the large number of individual time series, we also saw a rare loss of fluctuation between states for HSP90 over the experiment. The duration varied, but the protein returned to its function afterwards. A recent study emphasized this phenomenon in their experiments and linked the loss of fluctuation between states to the loss of structure for their protein. We think that this could also be the case here for HSP90 which was not seen before.
However, the presented synthesis is not without flaws. I showed that the developed protocol does not purify the nanoparticle to the degree necessary to avoid byproducts. This could alter the reaction in unpredictable ways as the remaining PEG contains thiol groups and amino groups which both bind

to SMCC. Therefore the real ratio of free binding sites on the nanoparticle are unknown. Secondly, I showed that the yield of the synthesis is seemingly independent of the used HSP90 concentration but yields no time series with fluctuation when HSP90 is excluded. Since the particles concentration was determined from the absorbance at $400\,\mathrm{nm}$ from diluted samples, the noise of the spectroscopic measurement introduces an error in the calculation. Finally, the reaction was not repeatable after the prepared samples of functionalized nanoparticles were used. Future studies should focus on the synthesis of functionalized nanoparticles that can undergo excessive purification to ensure a little residue PEG and SMCC remain in the sample before the reaction with HSP90.
The state finder algorithm should also be improved for the further study of the time series with more than two states. In those time series about ten percent of states are wrongly allocated which can have a significant impact on the dwell time distribution. But since the wrongly allocated states are not evenly distributed a use of parts of the recorded time series is possible for future research.

Chapter 7

Software Improvements

The changes in the reaction protocol lead to the successfully recording of multiple thousands of time series. To efficiently find the ones which show HSP90 dynamics and extract the dwell times new software tools were needed.

In this chapter I present the improvements and new developements I made for the filtering and evaluation of HSP90 plasmon ruler experiments. First, I explain the principle behind the fluctuation filter I developed and evalauate the performance based on the user inputs. Second, I show the heatmap visualization. This method allows for a fast visual identification of the location, number and relative population of states in time series. For the extraction of dwell times form the recorded time series, I used a new algorithm. I evaluated the accuracy of this algorithm for time series with two, three and four states. I show that for time series with two states the accuracy is high enough that wrongly allocated states do not influence the evaluation of the extracted dwell times. For time series with three and four states the accuracy is worse than for two states. Here around ten percent of states is allocated falsely.

7.1 Development of a fluctuation filter for the identification of plasmon ruler time series

The developed batch synthesis enabled a higher experimental throughput due to the lowered preparation time and omission of the surface passivation. To not view all recorded time series by eye and efficiently filter out non fluctuation time series, I developed a fluctuation filter. In an experiment without drift time series where more than a single intensity level is present can be identified by the number of maxima in the histogram over the recorded intensity. However, this doesn't necessarily give information over the amount switching between the states. Secondly, if there is drift

present a histogram over the full time series doesn't show the real number of states. To overcome these issues I split the time series in pieces of variable length (input by the user). In each piece the number of maxima in the histogram over the intensity is determined (see figure 7.1 a). If more than one maxima is found in the histogram this time piece is counted as having fluctuation. As seen in the insets of figure 7.1 a, sections with a lot of fluctuation and with little are correctly recognized. The fraction of number of pieces with more than one maxima to the number of pieces with exactly one maximum is given as the time fraction with fluctuation between states (see figure 7.1 b). The user can decide for a minimal fraction of fluctuation (e.g. 20% of the time series shows fluctuation) and only time series confining to this criterion are then shown.

I evaluated the performance of the developed filter for both input variables, length of the time series piece and percentage of fluctuation. For this I manually viewed all time series that remained after applying the filter and counted how many did not show fluctuations between states and were not filtered out. Figure 7.1 c shows the percentage of time series that were within the filter criteria and the percentage of time series that were excluded from the filtered subset after viewing by me. The larger the time span of the time series piece, the more time series were falsely remaining within the filter criteria and the larger the threshold for the fluctuation fraction the less total time series remained after filtering. I decided to use a time span of two minutes for the time series pieces and a fraction of fluctuation of 30% as for those parameters no time series without fluctuation was found within the filtered time series. The code for the filter algorithm can be read in the appendix E.2.

7.2 Heatmap visualization for fast identification of states in plasmon ruler time series

While in shorter time series the number of states can often be seen directly, this is not the case in time series that are multiple hours long. To identify the number and intensity levels of the present states, one has to zoom in multiple times which cost time and does not show changes over the whole experiment (see figure 7.2). Together with Thorsten Hugel we developed a visualization method that makes it possible to see the location and population density of all states over the full time series length. We called this tool "heatmap".
Similarly to the fluctuation filter, the heatmap also uses histogram in pieces of the time series. The binning of the histograms is predefined to achieve comparable counts for each piece of the time series. In a piece of 2000 data points a histogram over the intensity is calculated. The number of

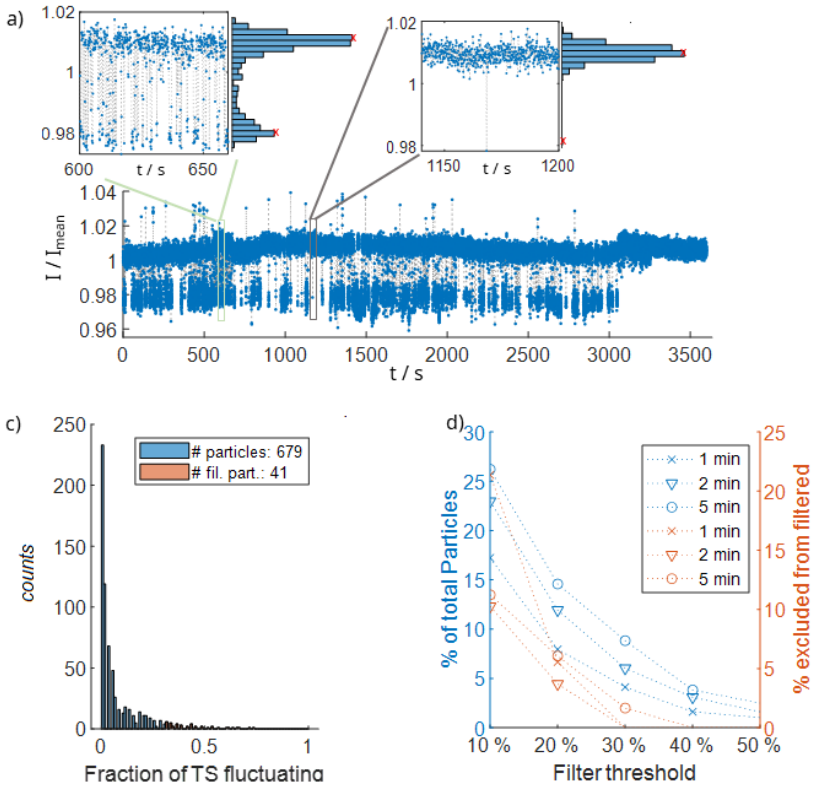

Figure 7.1: Working principle of the developed fluctuation filter. a) Example timeseries over one hour recorded with 100 ms exposure time. The timeseries is split into pieces of a length determined by the user. Insets show two different sections of 1 minute length of the timeseries. Over each section a histogram is taken and the number of maxima determined (red crosses) (See right of the insets). The number of sections with more than one maxima is divided by the total number of sections which gives an estimation over the fraction of recorded time that shows fluctuation between different states. b) Histogram over the fraction of fluctuation time for one experiments. The user picks a cutoff and only timeseries with a higher fraction of fluctuation will be included for further evaluation. In this image a cutoff of 30% was chosen. c) Evaluation of filter performance by input parameter.Left y-axis shows the percentage of total particles included in the filter criteria, meaning (potential) functional plasmon rulers. Right y-axis shows the fraction of particles which were excluded by hand after applying the filter and were wrongly included because for example drift caused a signal of only one state to appear like two states in the histogram.

data points per histogram bin is then transformed to a color scale. In the next step the histogram moves by 1000 data points which results in an overlap of the taken histograms. This makes it possible to see the onset of ending of each state (see figure 7.3). We used a logarithmic color scale for two reasons. For one it makes the difference better visible and secondly it linkes the shown color to the free energy landscape. What we see in a time series is a two dimensional projection of the free energy landscape of the protein conformations. Each stable conformation is a minimum in the energy landscape and the higher the barriers around one minimum, the longer the protein stays in that conformation. The rate k at which an energy barrier is overcome in a chemical process is given by the Arrhenius equation $k = A \cdot e^{\frac{E_A}{RT}}$. The universal gas constant R, the temperature T and the Arrhenius factor A are constants for the process. Since we see the rate at which the conformational changes take place, the color code of the heatmap directly visualized the height of the energy barrier E_A.

Listing 7.1: Function which transforms the data points of the time series ts into a heatmap

```
function [slid_hist, sp_x, mploc] = tsheatmap(ts,wl,bn)
    % input into function:
    % ts = time series
    % wl = window length
    % bn = bin number (of intensity)
    tsl = length(ts);
    % default parameters if not provided by user
    if nargin < 3
        bn = 256;
    end
    if nargin < 2
        wl = 1800;
    end
    % global histogram for uniform bins in sliding
       histogram
    [~, edge] = histcounts(ts, bn);
    %transform bin edges to bin centers
    edge2 = edge+(edge(1)-edge(2))/2;
    edge2(end) = [];
    sp_x=edge2;
    % setting up parameters for loop
    stepsize = round(wl/2);
    j=0;
    %set slidhist to zeros for faster loop
    slid_hist=zeros(round((tsl-wl)/stepsize),bn);
    %start of sliding histogram calculation
    for i = 1:stepsize:tsl-wl
        j=j+1;
```

```
28          slid_hist(j,:) = histcounts(ts(i:i+wl), edge);
29      %find peaks in histograms
30      [mpks{j},mploc{j}] = findpeaks(spline(edge2,smooth(
            slid_hist(j,:)),sp_x),'MinPeakProminence',10);
31      end
32  end
33  % output:
34  % slid_hist = counts per bin for one window
35  % sp_x = x value of each window
36  % mploc = location of found maxima in histograms
```

We used the heatmap to quickly visualize the number, location and changes in the states of our recorded time series. This made it possible to see the disordered parts in the time series shown in figure 6.12 which could be causes by denaturing of the protein and subsequent refolding.

7.3 New Statefinder for signals with more than two state

For the evaluation of time series with more than two states we required a new algorithm. When no drift is present and the time series shows only two states a simple threshold algorithm can be used to classify each state. All data point above a set level belong to state a and all data points below to state b. This, however, is more complicated to realize for more than two states and when drift in present in the experiment and not easily correctable.

Since the recorded data showed more than two states with varying signal to noise ratio, I used another algorithm for the state identification and dwell time extraction, which Karl Wandner programmed for me.

The algorithm works in two steps. First the signal is treated with a total variance denoising algorithm [78]. This results in a signal of constant levels of varying height and length (figure 7.4 top). In a second step, this signal is cleaned according to the user input regarding minimal step width and minimal step height (figure 7.4 middle). For the minimal step width I chose two data point to avoid the counting of single outliers as real states and potentially cutting a rare long dwell time in two pieces. The minimal step height was chosen for each time series individually until a visually well fitting allocation was achieved (figure 7.4 bottom).

Once all constant parts confine to the set parameters, with regard to the minimal width and level difference, the dwell times and state levels are save for further evaluation. I tested the performance of the new statefinder on the time series with fluctuation from one experiment. I did use the experiment with the highest number of found HSP90 time series for the evaluation. This experiment contained 53 time series which conformed to the filter criteria of 30% of time show fluctuation. From those time series I

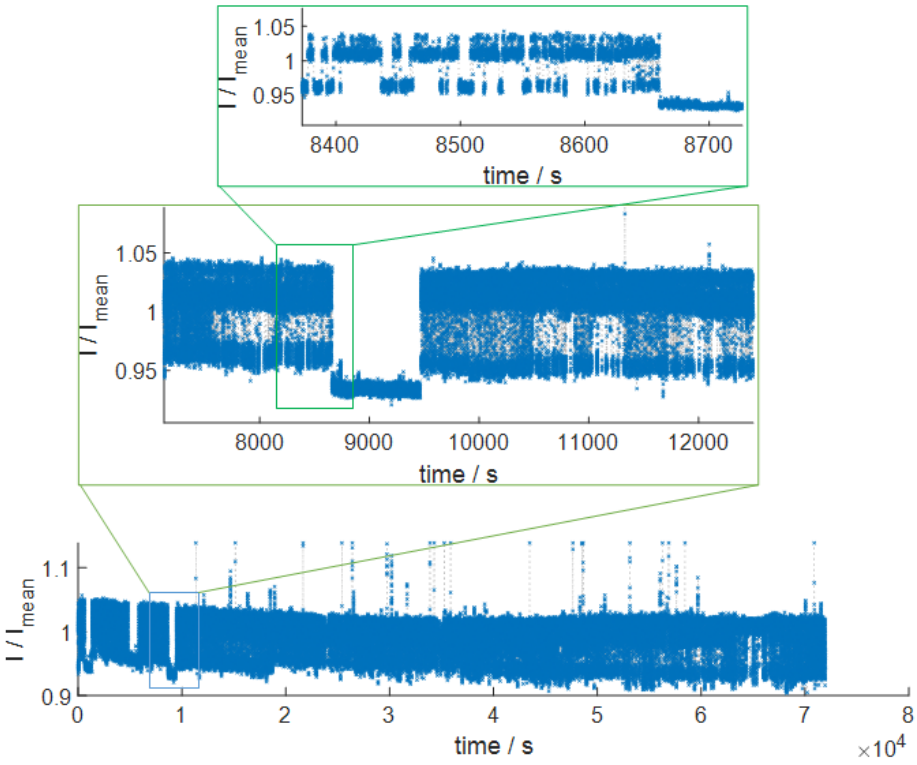

Figure 7.2: Example timeseries taken over 20 hours with time resolution of 30 ms. Looking at smaller fragments of the timeseries shows the number of intensity levels more clearly than looking at the full timeseries

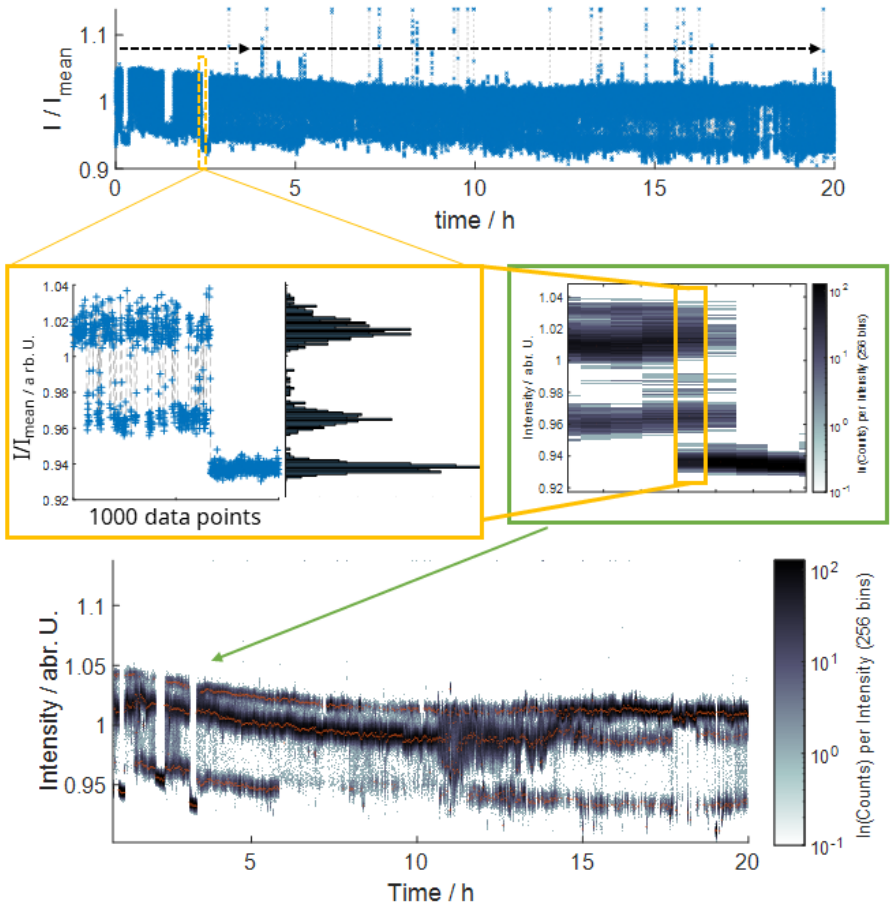

Figure 7.3: First the recorded intensities of the time series are binned into 256 bins which are then used for the visualization process. In a window of 2 minutes length (orange rectangle) a histogram with the bins determined before, of the time series section is taken (orange box) and maxima with a minimum prominence determined (red crosses). The window is shifted over the time series by half its window size and the process repeated until the end of the time series is reached. The histogram counts are displayed in a logarithmic color scale over time. Darker colors means more data points, red point mark the determined maxima for each time section.

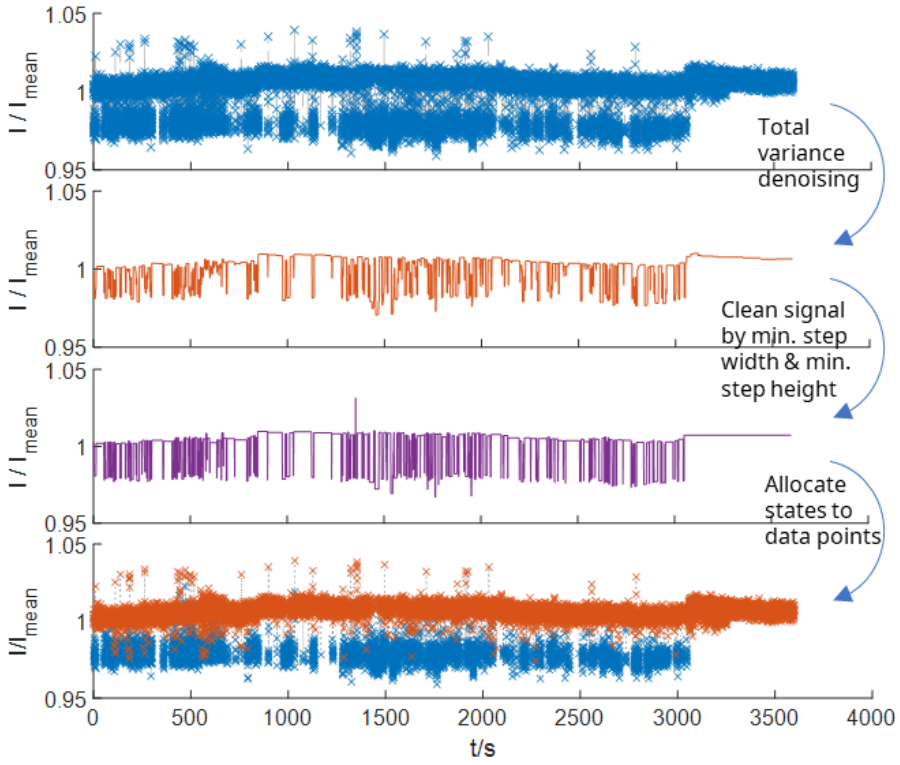

Figure 7.4: a) Example time series of 1 hour duration with time resolution of 100 ms. b) Signal after total variance denoising, resulting in a signal containing plateaus with constant levels. c) Data after cleaning the denoised signal so each plateau conforms to the minimal length and the minimal difference to neighbouring states which are inputs by the user. d) Raw signal colorcoded by assigned states from c)

excluded 14 because the algorithm did not allocate the number of states correctly (see figure 7.9 for an example). My assumption in the evaluation of the state finder accuracy was that the distributions of state levels for each individual state should not overlap if the allocation is correct. To determine whether a state is allocated in the distribution of levels of another state I determined the separation line between each state by calculating the half distance between the maxima of each states level distribution (see figure 7.5 b). As seen in the histogram of the determined state levels (figure 7.5 b) there is almost no overlap between the two distributions. This shows that the algorithm can correctly allocate states even with small amounts of drift in the experiment.

The evaluation of the state level accuracy showed that the majority of time series has little to no wrongly allocated states. Also the state of the closed conformation (higher intensity) seems to be more prone to errors in the allocation (figure 7.5 c). The bias in the allocation accuracy could be an artifact in the algorithm. Out of the evaluated 21 time series, 6 showed to have more than 5% wrongly allocated states.
The incorrect allocation of state can have different impact on the evaluation of the extracted dwell times. Three cases are possible:

1. State A is incorrectly allocated but both neighbouring states are allocated correctly. (Only possible for three and more states)

2. State A is incorrectly allocated inside of State B, therefore cutting the dwell time of state b in two shorter pieces

3. State A is incorrectly allocated because of missed transitions into state B, therefore extending the dwell time of state A.

If only case one was possible, one could exclude the falsely allocated states without changes to the overall distribution. However, the other cases result in incorrect dwell times and result in either too short or too long dwell times that are not present in the data.
To determine the effect of the falsely allocated states and the resulting errors in the dwell time distribution on the number of decay channels and decay times, I compared two sets of dwell times. One includes all dwell times and one excludes all dwell times from time series with more than 5% falsely allocated states. Since I cannot determine which of the three cases applied to each wrongly allocated state, I excluded all dwell times from time series with more than 5% falsely allocated states.

For both data sets I used the fit optimization I explained in chapter 6 to find the number of decay channels that best fit the dwell time distribution. While the distributions of the data set is visibly different, in both cases five decay channels resulted in the best fit to the dwell time distribution (figure 7.6). Especially for long dwell times the difference influences the fit accuracy since there are only single data points left. The exclusion of all dwell times from time series with falsely allocated states also excludes a substantial

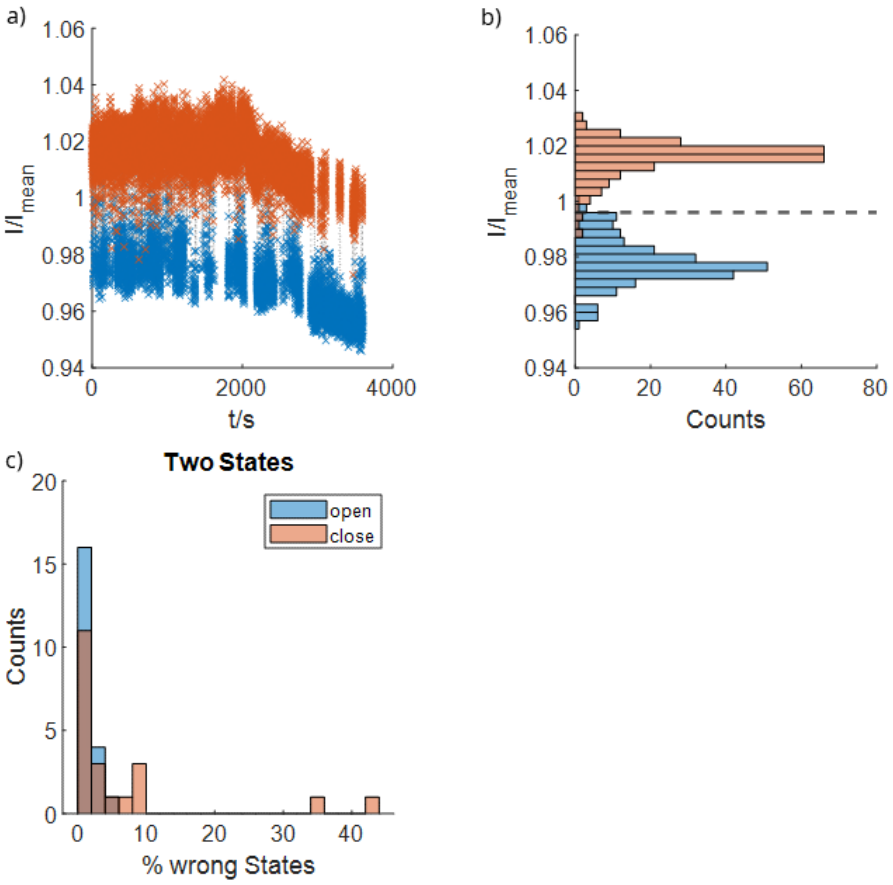

Figure 7.5: a) Example Timeseries with two states. Datapoints are colorcoded for the state the were allocated by the statefinder algorithm b) Histogram of the identified state levels by colored by state. Dashed line is calculated as the middle distance between the maxima of both states. States that cross over this line are considered “wrongly allocated” c) Histogram of the percentage of wrongly allocated states from 21 time series.

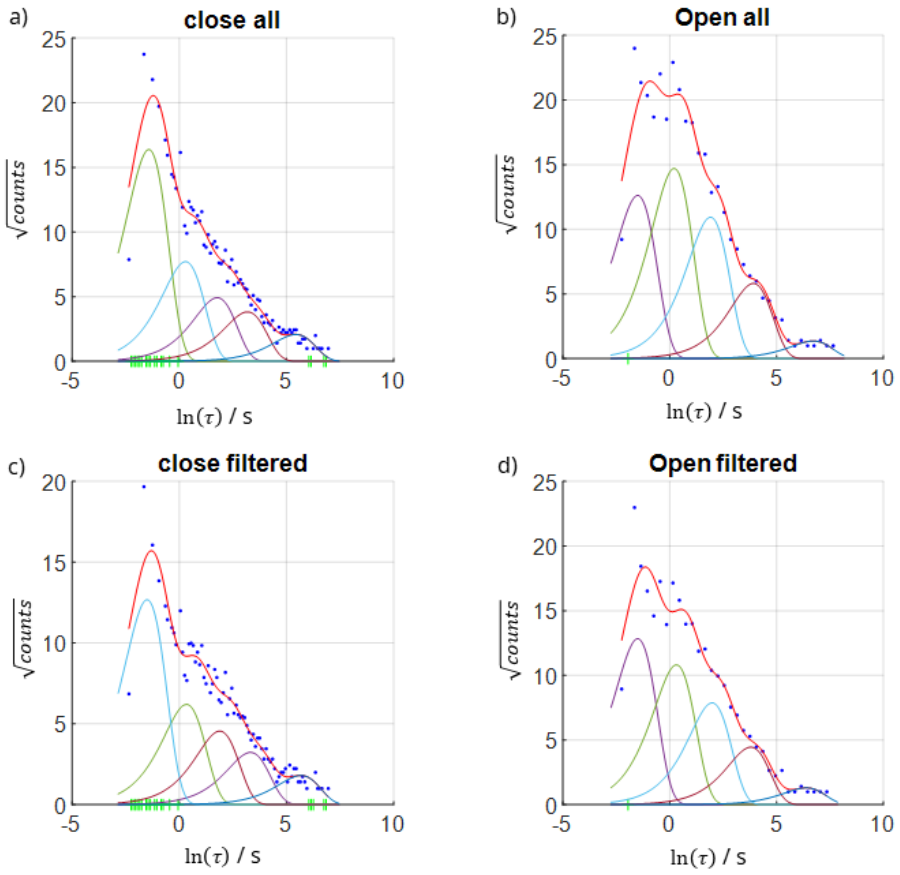

Figure 7.6: Dwell times for two state timeseries were fitted with the determined optimal parameters. Top: dwell times from all two state timeseries were included. For both states a model with 5 decay channels gave the best fit. Dwell times from timeseries with a more than 5% wrongly allocated states were removed and the data fitted again (bottom). In both cases the exclusion did not affect the number of decay channels or visible changes in the location of the individual channels. Resulting decay times are given in the figures, errors calculated from 65% confidence intervals.

amount of data points from the data set that is not effected by the errors in the state allocation. However, the number of states found is the same in both cases and the decay times for short dwell times are matching although the errors of the decay times from the filtered data set are large.

Table 7.1: Comparison of the extracted decay times of all dwell times and a filtered subset where all dwell times from 21 time series with more than 5% falsely allocated states were excluded (13 excluded).

$\text{open}_{\text{unfiltered}}$	$\text{open}_{\text{filtered}}$	$\text{closed}_{\text{unfiltered}}$	$\text{closed}_{\text{filtered}}$
0.24 ± 0.02	0.2 ± 0	0.24 ± 0.02	0.22 ± 0
1.4 ± 0.2	2.0 ± 0.7	1.3 ± 0.3	2 ± 2
7 ± 1	9 ± 44	6 ± 3	6 ± 12
50 ± 10	40 ± 60	24 ± 9	50 ± 90
800 ± 800	400 ± 7000	230 ± 70	500 ± 5000

I decided to not exclude any dwell times from the evaluation of the time series in chapter 6 to not reduce the number of rare long dwell times. The errors produced by the absence of long but real dwell times are more severe than the error caused by few falsely allocated dwell times in this data set (see table **??**). A further investigation in the allocation of states, potential trimming of time series and excluding only the falsely allocated states should be subject of further studies.

Statefinder accuracy for three and four state time series For time series with three and four states I also determined the accuracy of the state finder algorithm. I used the same threshold classification of the state levels as described in the previous section. Figure 7.7 shows example time series with colored states and the corresponding distributions of the state levels. For three states, the distributions of state levels show more overlap which indicated more falsely allocated states. The example time series with four states shows a flaw of the chosen classification strategy. If, like in this example, more states are falsely allocated than correctly, the threshold gets placed incorrectly. This causes a wrong classification of the states. To overcome this, one could alter the classification algorithm to not only use the number of states at a certain level but also the time spent in each state. However, the wrong allocation of state one happens only in a portion of the time series. The first two thirds of the time series are correctly allocated and could be used for further analysis.

In the analysis of all time series with three and four states from the example experiment, none showed perfect allocation of all states (see figure 7.7 a and b). Since the time series allocate more states in the same experimental time ($1\,\text{h}$), there are less individual data points for each state. Therefore,

the same number of falsely allocated states makes up a larger percentage. Especially for rarely visited states this can cause large percentage of false allocation. For time series with three states, there were no time series with less than 5% falsely allocated states, for time series with four states there were two. I evaluated the dwell times of the falsely allocated states to see if a certain dwell time in more susceptible to wrong allocation and might cause artifacts in the evaluation.

Figure 7.7 c and d show the histogram of the logarithmic binned dwell times of the falsely allocated states. For both, three and four state time series mostly short dwell times are visible. In time series with three states, predominantly state two had falsely allocated dwell times. The visible pattern matches the distribution of dwell times for two state time series, thus indicating that the falsely allocated dwell times match the distribution of correct dwell times. In the distribution of the dwell times from four state time series, the dwell times of state two and three make up the majority of falsely allocated states. Those states are also the ones which are visited the most. Here a pattern is visible, where for both states distinct maxima are formed in the distribution that match previously extracted decay channels. One maximum is around $t = ln(-2)s$ matching the decay time of $0.2\,\mathrm{s}$ and the other around $t = ln(1.5)s$ matching the decay time of $1.4\,\mathrm{s}$.

A comparison of the number of decay channels and resulting decay times between dwell time from time series with and without falsely allocated states in four state time series was tried (see figure 7.10 and 7.11 for comparisons between the fitted models). However the amount of data is too low from two time series to make conclusions.

7.4 Summary

In this chapter I presented the software tools that were developed by me for the evaluation and identification of HSP90 time series from my experiments.

I developed a fluctuation filter which determines the amount of time in a time series with more than one distinct level (called states) in the recorded intensity. The user can choose how small the time increments should be at which the filter operates. As a second parameter the user can set a fraction of total experimental time in which more than one state is detected. I evaluated the filter for both parameters with regard to found plasmon rulers and falsely found plasmon rulers. Using time increments of two minutes and a cutoff of 30% of the time series have to show more than one state, no false are present, which are the parameters that I used for all experiments. Future research could lower the threshold to 20% or 10% to gather more HSP90 data with the drawback of additional manual filtering of the false positive that remain after filtering.
To quickly visualize the number and location of all states in a time series, I developed a visualization methode we called "heatmap". The heatmap uses

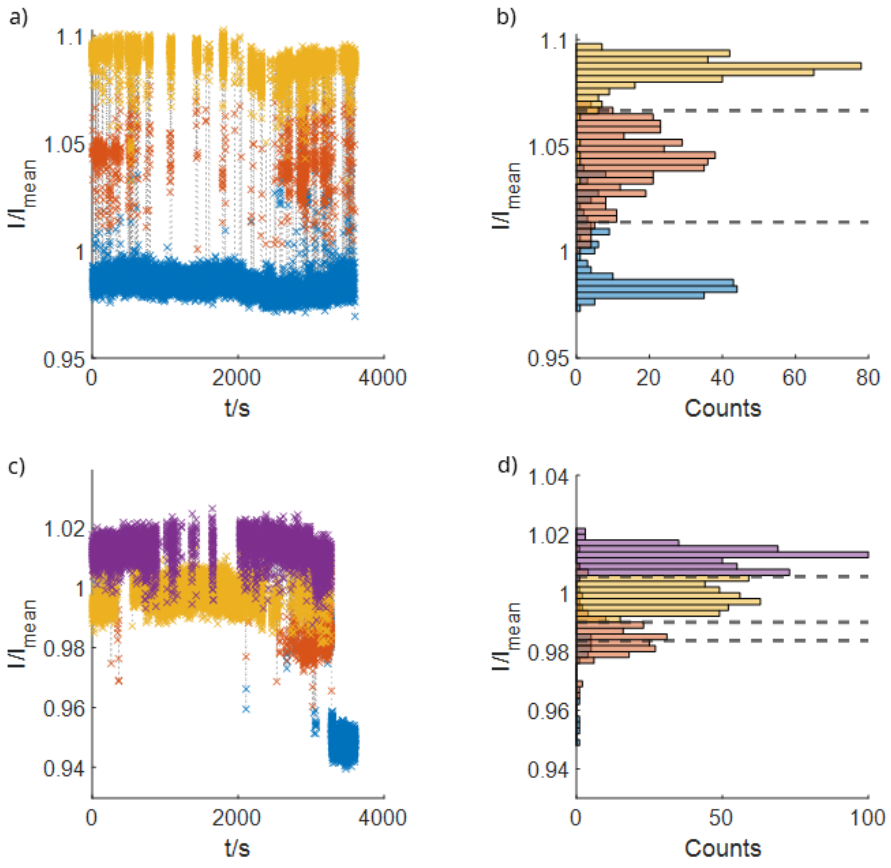

Figure 7.7: a) Example times eries with 3 states. Datapoints colorcoded with states as identified by algorithm. b) Histogram over identified statelevels of each state of time series in a). Colorcode for individual states. Dashed lines are calculated from half difference between maxima and indicate thresholds for “wrongly allocated” states. c) Example timeseries with 4 states. Datapoints color coded with states as identified by algorithm. d) Histogram over identified state levels for each state of time series in a). Color-code for individual states. Dashed lines are calculated from half difference between maxima and indicate thresholds for “wrongly allocated” states. The separating line for state 1 (blue) and state 2 (orange) is not allocated correctly since the majority of state 1 was allocated at the level of state 2 in the later third of the time series.

a sliding histogram and depicts the counts of the histogram in a logarithmic color scale. This links the color directly to the energy barrier between the states.
For the evaluation I used a new statefinder algorithm which was programmed for me by Karl Wandner. This algorithm operates in multiple steps. First the time series with transformed to a step signal by total variance denoising. Afterward the steps are combined until the user inputs of minimal height difference of each step and minimal length are satisfied. This algorithm is able to identify distinct states even when small amounts of drift are present and for low signal to noise. I evaluated the accuracy of this algorithm for my experimental data and found that for time series with two states the majority of time series has no errors in the allocation of states. Six out of twenty-one time series had more than five percent of their states wrongly allocated, which did not influence the number of found decay channels. For time series with three and four states the accuracy is not good enough in some parts of the time series. Future developments should involve the trimming of time series with more than two states to extract the dwell times from the parts where the allocation was correct.

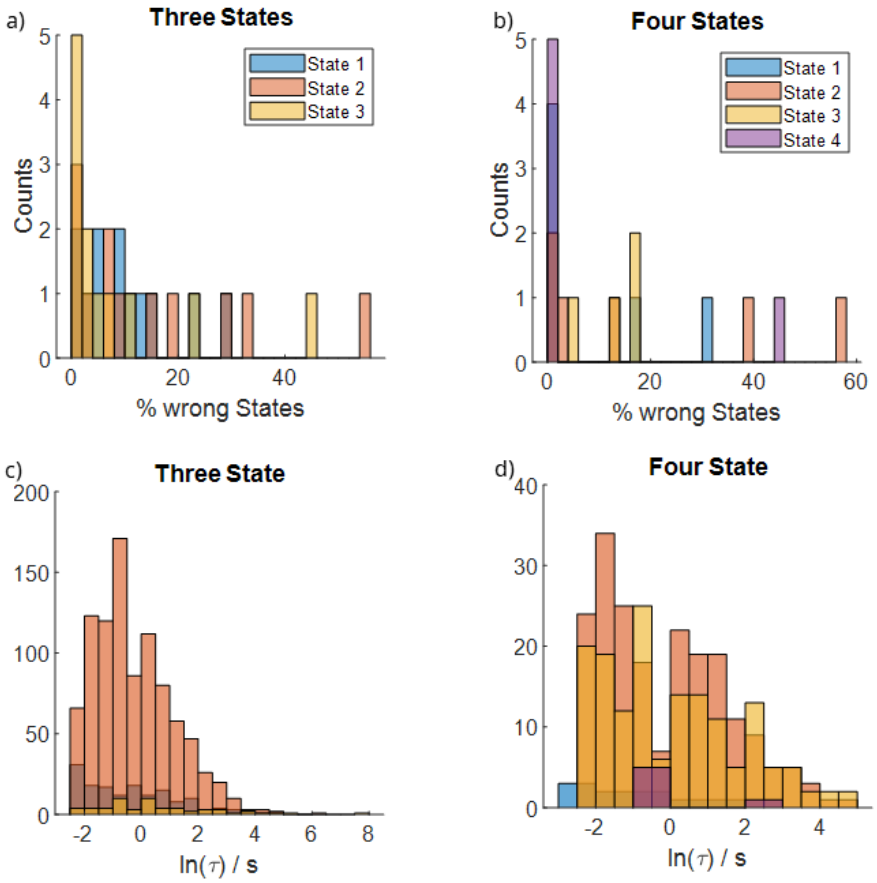

Figure 7.8: a) Histogram over the number of wrongly allocated states for all time series with three states from a single experiment. State two (orange) and three (yellow) show the largest percentage of wrongly allocated states. No time series in this experiment has a sum of wrongly allocated stated below 5%. b) Histogram over the number of wrongly allocated states for all time series with four states from a single experiment. Because the experimental time is fixed but more states are visited, the number of times each state decreases and therefor the same number of wrong allocations leads to higher percentage of wrongly allocated states. Two out of six time series have a total of less than 5% wrongly allocated states. c) Logarithmic binned histogram over dwell times of wrongly allocated stated, color-coded by state (see above for legend). State two (orange) makes up the majority of time and dwell times that were wrongly allocated. d) Logarithmic binned histogram over dwell times of wrongly allocated stated, color-coded by state (see above for legend). The wrongly allocated dwell times of state two (orange) and three (yellow) show at least two populations matching roughly with two corresponding decay channels ($\ln -2s$ and $\ln 1.5s$).

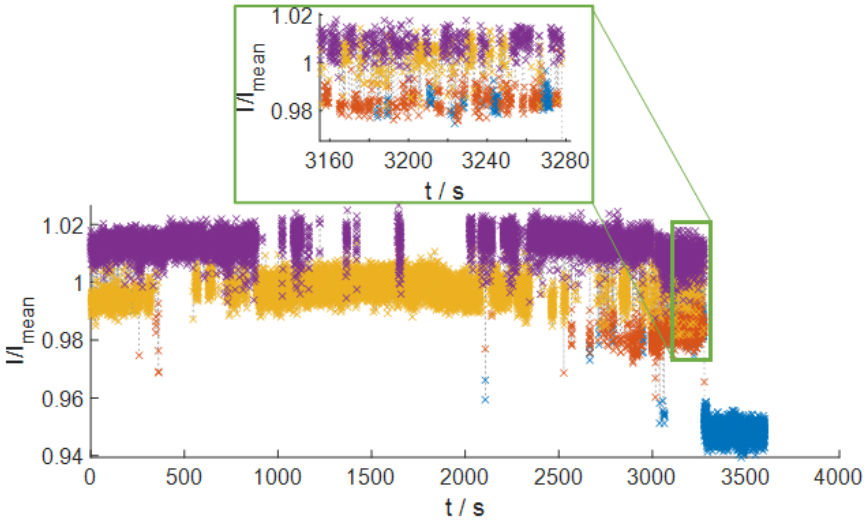

Figure 7.9: Example time series of $1\,\mathrm{h}$ duration and time resolution of $100\,\mathrm{ms}$. Four states were identified and color coded as identified by the algorithm. The inset shows the are where the allocation did not work correctly.

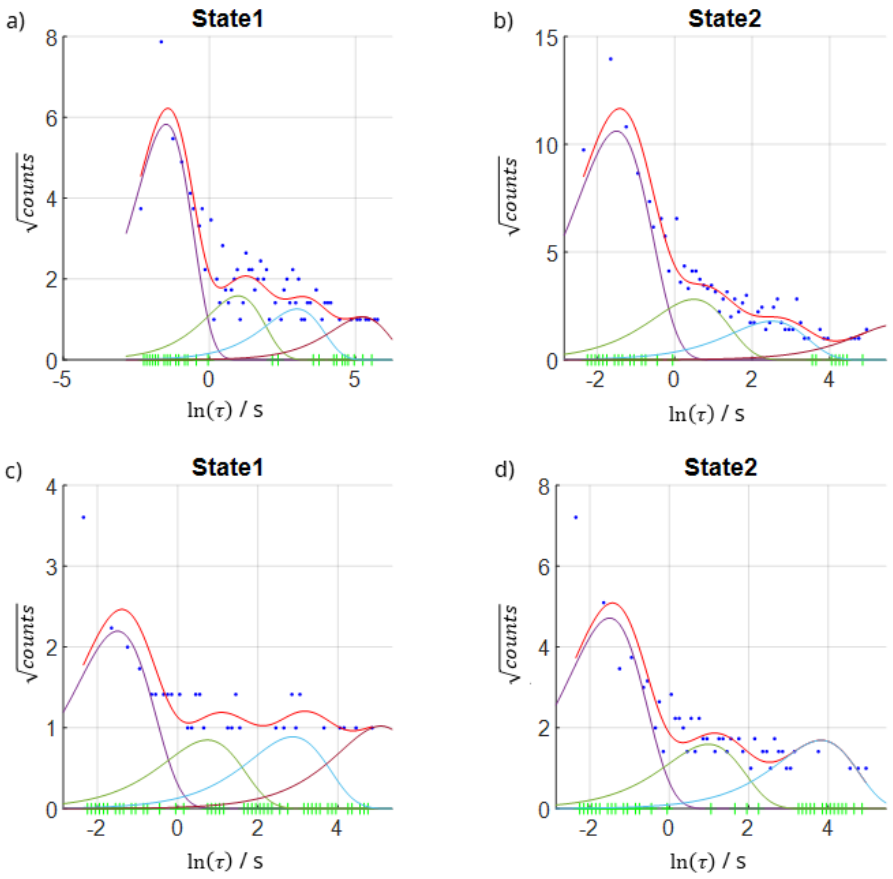

Figure 7.10: Comparision of the dwell time distribution from four state time series with (top) and without (bottom) dwell times from time series with more 5% falsely allocated states.

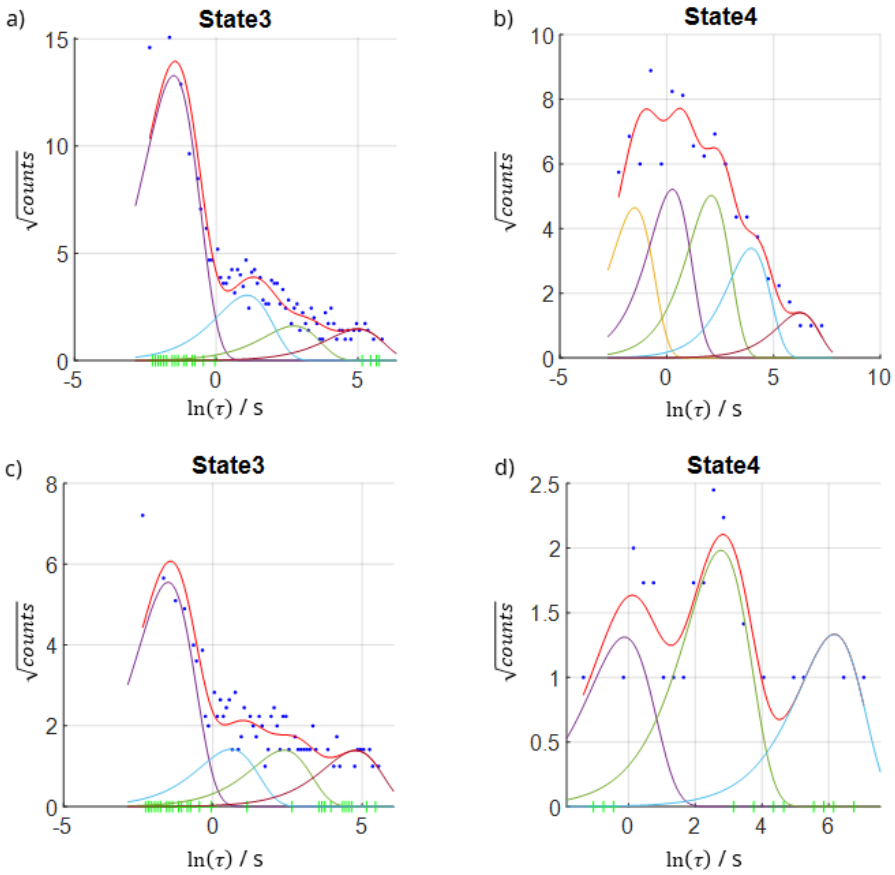

Figure 7.11: Comparision of the dwell time distribution from four state time series with (top) and without (bottom) dwell times from time series with more 5% falsely allocated states.

Chapter 8

Summary and outlook

Plasmon rulers consist of two noble metal nanoparticles. When the distance between the particles is less than their diameter, the plasmons couple which results in a large increase in scattering intensity and resonance wavelength. The strength of the coupling and therefore the increase in scattering intensity and resonance wavelength scale exponentially. Our group used these properties to investigate the conformational change of the HSP90 protein. In this work I present the advances made in the plasmon ruler project which resulted from the development of a new synthesis method and analysis tools.

I investigated the previous synthesis method, which build the plasmon ruler step by step in a solid phase synthesis, to gain insight in the variations between individual experiments. I show that this synthesis yield functional plasmon rulers in one sixth of the started experiments. However the total number of functional plasmon rulers was five over 21 experiments. I increased the number of binding sites on the nanoparticle to increase the number of formed plasmon ruler, which lead to the formation of aggregates of more than two particles. In these experiments I found that an insufficiently passivated surface is the biggest source of failed experiments. To improve the plasmon ruler synthesis, I investigated theoretical reaction conditions and present strength and weaknesses of different possible reactions. For both, a synthesis in flowcell and a in batch, an asymmetry in reactivity is needed. If both particles are highly reactive the chance to form aggregates of more than two particle increases drastically. For the batch synthesis I propose two functionalization strategies to form plasmon rulers and calculated the maximum yield of formed plasmon rulers to be 18%. The average reaction time to form a plamon ruler in a batch synthesis was calculated to be ten minutes.
In chapter five I probe different passivation strategies for the application in plasmon ruler experiments. I present the theoretical background on the reaction and challenges when conducting reactions on glass. For the

use of passivated glass surfaces in plasmon ruler experiments I set three constraints: A maximum of 1% of particles bind unspecifically, the reaction must not leave scattering residues and a low amount of binding sites has to be introduced for covalent fixation of the nanoparticles on the surface. I tested three reaction protocols which were provided from collaborators, which all failed to meet the constraints for plasmon ruler experiments.
In chapter six I presented a new batch synthesis for HSP90 plasmon rulers which achieved an order of magnitude higher yields than the previous synthesis. Using this synthesis enabled a higher throughput and larger sample size of recorded HSP90 time series. This revealed that HSP90 has more than the previously known two distinct states. For the visualization of the time series, I developed a tool we called heatmap, which makes it possible to see the location and population density of each state over the full time series. I evaluated time series with the known two states and due to the larger sample size found that HSP90 has more than the previously assumed three decay channels. From my experimental data I suggest that five decay channels fit the best.
Chapter seven covers the advancement made in filtering and visualizing large amounts of data. I developed a filter that determines the relative amount of time in a time series that has more than one state. This filter reduces the evaluation time by excluding non functional plasmon rulers and particles that did not form plasmon rulers from further evaluations. To visualize the number of states in the time series, I developed the before mentioned heatmap. The heatmap is created by depicting the intensities of a sliding histogram on a logarithmic scale. The logarithmic color scale directly links the color to the height of the energy barrier of each conformational state. For the extraction of the dwell times from the recorded time series Karl Wandner programmed a new statefinder algorithm. I showed that for time series with two states the algorithm allocated the states correctly without errors in the majority of time series. An evaluation of a data set with and without falsely allocated states showed that the degree or errors did not influence the number of determined decay channels. For time series with more than two states however the degree of errors was above ten percent wrongly allocated states, which was too high for an evaluation of the dwell times and resulting decay channels.

Bibliography

(1) Burgers, P. M.; Kunkel, T. A. *Annual review of biochemistry* **2017**, *86*, 417–438.

(2) Dyla, M.; Basse Hansen, S.; Nissen, P.; Kjaergaard, M. *Biochemical Society Transactions* **2019**, *47*, 1247–1257.

(3) Kodera, N.; Yamamoto, D.; Ishikawa, R.; Ando, T. *Nature* **2010**, *468*, 72–76.

(4) Nord, A. L.; Gachon, E.; Perez-Carrasco, R.; Nirody, J. A.; Barducci, A.; Berry, R. M.; Pedaci, F. *Proceedings of the National Academy of Sciences* **2017**, *114*, 12952–12957.

(5) Nogales, E. *Nature methods* **2016**, *13*, 24–27.

(6) Alderson, T. R.; Kay, L. E. *Current Opinion in Structural Biology* **2020**, *60*, Folding and Binding Proteins, 39–49.

(7) Schmid, S.; Hugel, T. *eLife* **2020**, *9*, DOI: \url{10 . 7554 / eLife . 57180}.

(8) Ye, W.; Götz, M.; Celiksoy, S.; Tüting, L.; Ratzke, C.; Prasad, J.; Ricken, J.; Wegner, S. V.; Ahijado-Guzmán, R.; Hugel, T.; Sönnichsen, C. *Nano letters* **2018**, *18*, 6633–6637.

(9) Henzler-Wildman, K.; Kern, D. *Nature* **2007**, *450*, 964–972.

(10) Ode, H.; Nakashima, M.; Kitamura, S.; Sugiura, W.; Sato, H. *Frontiers in microbiology* **2012**, *3*, 258.

(11) Bibow, S.; Hiller, S. *The FEBS journal* **2019**, *286*, 1610–1623.

(12) Avellaneda, M. J.; Franke, K. B.; Sunderlikova, V.; Bukau, B.; Mogk, A.; Tans, S. J. *Nature* **2020**, *578*, 317–320.

(13) Ganji, M.; Shaltiel, I. A.; Bisht, S.; Kim, E.; Kalichava, A.; Haering, C. H.; Dekker, C. *Science (New York, N.Y.)* **2018**, *360*, 102–105.

(14) Neuman, K. C.; Nagy, A. *Nature methods* **2008**, *5*, 491–505.

(15) Ratzke, C.; Hellenkamp, B.; Hugel, T. *Nature communications* **2014**, *5*, 4192.

(16) Stryer, L.; Haugland, R. P. *Proceedings of the National Academy of Sciences* **1967**, *58*, 719–726.

(17) Leavesley, S. J.; Rich, T. C. *Cytometry. Part A: the journal of the International Society for Analytical Cytology* **2016**, *89*, 325.

(18) Sanders, J. C.; Holmstrom, E. D. *Essays in biochemistry* **2021**, DOI: \url{10.1042/EBC20200022}.

(19) Albrecht, T. *Annual review of analytical chemistry (Palo Alto, Calif.)* **2019**, *12*, 371–387.

(20) Sönnichsen, C.; Reinhard, B. M.; Liphardt, J.; Alivisatos, A. P. *Nature biotechnology* **2005**, *23*, 741–745.

(21) Reinhard, B. M.; Sheikholeslami, S.; Mastroianni, A.; Alivisatos, A. P.; Liphardt, J. *Proceedings of the National Academy of Sciences of the United States of America* **2007**, *104*, 2667–2672.

(22) Tüting, L.; Ye, W.; Settanni, G.; Schmid, F.; Wolf, B. A.; Ahijado-Guzmán, R.; Sönnichsen, C. *The Journal of Physical Chemistry C* **2017**, *121*, 22396–22402.

(23) Rana, S.; Yeh, Y.-C.; Rotello, V. M. *Current Opinion in Chemical Biology* **2010**, *14*, Model Systems/Biomolecular Synthesis and Modification, 828–834.

(24) Heath, G. R.; Scheuring, S. *Nature communications* **2018**, *9*, 4983.

(25) Desai, V. P.; Frank, F.; Lee, A.; Righini, M.; Lancaster, L.; Noller, H. F.; Tinoco, I.; Bustamante, C. *Molecular cell* **2019**, *75*, 1007–1019.e5.

(26) Vanderlinden, W.; Brouns, T.; Walker, P. U.; Kolbeck, P. J.; Milles, L. F.; Ott, W.; Nickels, P. C.; Debyser, Z.; Lipfert, J. *Nature communications* **2019**, *10*, 4738.

(27) Yang, X.; Garnier, F.; Débat, H.; Strick, T. R.; Nadal, M. *Proceedings of the National Academy of Sciences of the United States of America* **2020**, *117*, 10856–10864.

(28) Janissen, R.; Arens, M. M. A.; Vtyurina, N. N.; Rivai, Z.; Sunday, N. D.; Eslami-Mossallam, B.; Gritsenko, A. A.; Laan, L.; de Ridder, D.; Artsimovitch, I.; Dekker, N. H.; Abbondanzieri, E. A.; Meyer, A. S. *Cell* **2018**, *174*, 1188–1199.e14.

(29) Löf, A.; Walker, P. U.; Sedlak, S. M.; Gruber, S.; Obser, T.; Brehm, M. A.; Benoit, M.; Lipfert, J. *Proceedings of the National Academy of Sciences of the United States of America* **2019**, *116*, 18798–18807.

(30) Seifert, M. et al. *bioRxiv* **2021**, DOI: \url{10.1101/2020.08.06.240325}.

(31) Zosel, F.; Mercadante, D.; Nettels, D.; Schuler, B. *Nature communications* **2018**, *9*, 3332.

(32) Fitzgerald, G. A.; Terry, D. S.; Warren, A. L.; Quick, M.; Javitch, J. A.; Blanchard, S. C. *Nature* **2019**, *575*, 528–534.

(33) Galenkamp, N. S.; Maglia, G. **2020**, DOI: \url{10.1101/2020.04.14.040733}.

(34) Laszlo, A. H.; Derrington, I. M.; Ross, B. C.; Brinkerhoff, H.; Adey, A.; Nova, I. C.; Craig, J. M.; Langford, K. W.; Samson, J. M.; Daza, R.; Doering, K.; Shendure, J.; Gundlach, J. H. *Nature biotechnology* **2014**, *32*, 829–833.

(35) Hartel, A. J. W.; Ong, P.; Schroeder, I.; Giese, M. H.; Shekar, S.; Clarke, O. B.; Zalk, R.; Marks, A. R.; Hendrickson, W. A.; Shepard, K. L. *Proceedings of the National Academy of Sciences of the United States of America* **2018**, *115*, E1789–E1798.

(36) Ahijado-Guzmán, R.; Prasad, J.; Rosman, C.; Henkel, A.; Tome, L.; Schneider, D.; Rivas, G.; Sönnichsen, C. *Nano letters* **2014**, *14*, 5528–5532.

(37) Kaefer, K.; Krüger, K.; Schlapp, F.; Uzun, H.; Celiksoy, S.; Flietel, B.; Heimann, A.; Schroeder, T.; Kempski, O.; Sönnichsen, C. *Nano letters* **2021**, *21*, 3325–3330.

(38) Reinhard, B. M.; Siu, M.; Agarwal, H.; Alivisatos, A. P.; Liphardt, J. *Nano Letters* **2005**, *5*, 2246–2252.

(39) Su, K.-H.; Wei, Q.-H.; Zhang, X.; Mock, J. J.; Smith, D. R.; Schultz, S. *Nano Letters* **2003**, *3*, 1087–1090.

(40) Jain, P. K.; Huang, W.; El-Sayed, M. A. *Nano Letters* **2007**, *7*, 2080–2088.

(41) Sönnichsen, C.; Franzl, T.; Wilk, T.; von Plessen, G.; Feldmann, J.; Wilson, O.; Mulvaney, P. *Physical Review Letters* **2002**, *88*, 957.

(42) Jun, Y.-w.; Sheikholeslami, S.; Hostetter, D. R.; Tajon, C.; Craik, C. S.; Alivisatos, A. P. *Proceedings of the National Academy of Sciences of the United States of America* **2009**, *106*, 17735–17740.

(43) Ye, W. Automated spectral imaging plasmonscope for unraveling molecular dynamics, Dissertation, Mainz: Johannes Gutenberg-Universität, 2019.

(44) Celiksoy, S. Single Line Imaging Methond (SLIM) for Biochemical Applications, Dissertation, Mainz: Johannes Gutenberg-Universität, 2021.

(45) Nan, J.; Zhu, S.; Ye, S.; Sun, W.; Yue, Y.; Tang, X.; Shi, J.; Xu, X.; Zhang, J.; Yang, B. *Advanced materials (Deerfield Beach, Fla.)* **2019**, e1905927.

(46) Yadav, P. R.; Rizvi, M. H.; Kuttich, B.; Mishra, S. R.; Chapman, B. S.; Lynch, B. B.; Kraus, T.; Oldenburg, A. L.; Tracy, J. B. *ACS Applied Nano Materials* **2021**, DOI: `\url{10.1021/acsanm.1c00309}`.

(47) Wang, J.; Song, J.; Zhang, X.; Wang, S.-M.; Kang, B.; Li, X.-L.; Chen, H.-Y.; Xu, J.-J. *Journal of the American Chemical Society* **2023**, *145*, 1273–1284.

(48) Tüting, L. Molecular Dynamics: Investigated by Plasmon Rulers, Dissertation, Mainz: Johannes Gutenberg-Universität, 2017.

(49) Merrifield, R. B. *Journal of the American Chemical Society* **1963**, *85*, 2149–2154.

(50) Xiong, B.; Cheng, J.; Qiao, Y.; Zhou, R.; He, Y.; Yeung, E. S. *Journal of chromatography. A* **2011**, *1218*, 3823–3829.

(51) Steinigeweg, D.; Schütz, M.; Salehi, M.; Schlücker, S. *Small* **2011**, *104*, n/a–n/a.

(52) Chen, G.; Wang, Y.; Tan, L. H.; Yang, M.; Tan, L. S.; Chen, Y.; Chen, H. *Journal of the American Chemical Society* **2009**, *131*, 4218–4219.

(53) Liu, N.; Hentschel, M.; Weiss, T.; Alivisatos, A. P.; Giessen, H. *Science (New York, N.Y.)* **2011**, *332*, 1407–1410.

(54) Lee, S. E.; Chen, Q.; Bhat, R.; Petkiewicz, S.; Smith, J. M.; Ferry, V. E.; Correia, A. L.; Alivisatos, A. P.; Bissell, M. J. *Nano letters* **2015**, *15*, 4564–4570.

(55) Xia, X.; Yang, M.; Wang, Y.; Zheng, Y.; Li, Q.; Chen, J.; Xia, Y. *ACS nano* **2012**, *6*, 512–522.

(56) Ward, A. F. H.; Tordai, L. *The Journal of Chemical Physics* **1946**, *14*, 453–461.

(57) Sukhov, V. M.; Dement'eva, O. V.; Kartseva, M. E.; Rudoy, V. M.; Ogarev, V. A. *Colloid Journal* **2004**, *66*, 482–488.

(58) Grebenkov, D. S.; Metzler, R.; Oshanin, G. *Communications Chemistry* **2018**, *1*, DOI: `\url{10.1038/s42004-018-0096-x}`.

(59) Kuzmina, A. OPTIMIERUNG DES HSP90-PLASMON RULERS, Ph.D. Thesis, Mainz, 2021-01-11.

(60) Hanauer, M.; Pierrat, S.; Zins, I.; Lotz, A.; Sönnichsen, C. *Nano letters* **2007**, *7*, 2881–2885.

(61) Schenk, F. C.; Boehm, H.; Spatz, J. P.; Wegner, S. V. *Langmuir : the ACS journal of surfaces and colloids* **2014**, *30*, 6897–6905.

(62) Gidi, Y.; Bayram, S.; Ablenas, C. J.; Blum, A. S.; Cosa, G. *ACS applied materials & interfaces* **2018**, *10*, 39505–39511.

(63) Benters, R.; Niemeyer, C. M.; Wöhrle, D. *ChemBioChem* **2001**, *2*, 686–694.

(64) Pradhan, B.; Engelhard, C.; van Mulken, S.; Miao, X.; Canters, G. W.; Orrit, M. *Chemical Science* **2019**, *11*, 763–771.

(65) Sweryda-Krawiec, B.; Devaraj, H.; Jacob, G.; Hickman, J. J. *Langmuir : the ACS journal of surfaces and colloids* **2004**, *20*, 2054–2056.

(66) Besecker, J.; Cornell, K. A.; Hampikian, G. *Sensors and Actuators B: Chemical* **2013**, *176*, 118–123.

(67) Park, J. H.; Sut, T. N.; Jackman, J. A.; Ferhan, A. R.; Yoon, B. K.; Cho, N.-J. *Physical chemistry chemical physics : PCCP* **2017**, *19*, 8854–8865.

(68) Park, J. H.; Jackman, J. A.; Ferhan, A. R.; Ma, G. J.; Yoon, B. K.; Cho, N.-J. *ACS applied materials & interfaces* **2018**, *10*, 32047–32057.

(69) Patra, S.; Baibakov, M.; Claude, J.-B.; Wenger, J. *Scientific reports* **2020**, *10*, 5235.

(70) Bertin, A.; Schlaad, H. *Chemistry of Materials* **2009**, *21*, 5698–5700.

(71) Chen, J.-J.; Struk, K. N.; Brennan, A. B. *Langmuir : the ACS journal of surfaces and colloids* **2011**, *27*, 13754–13761.

(72) Hasan, A.; Pattanayek, S. K.; Pandey, L. M. *ACS biomaterials science & engineering* **2018**, *4*, 3224–3233.

(73) Ercole, C.; Del Gallo, M.; Mosiello, L.; Baccella, S.; Lepidi, A. *Sensors and Actuators B: Chemical* **2003**, *91*, 163–168.

(74) Campbell, G. A.; Mutharasan, R. *Biosensors & bioelectronics* **2005**, *21*, 462–473.

(75) Glass, N. R.; Tjeung, R.; Chan, P.; Yeo, L. Y.; Friend, J. R. *Biomicrofluidics* **2011**, *5*, 36501–365017.

(76) *Silanes and siloxanes as coupling agents to glass // Silanes and Siloxanes as Coupling Agents to Glass: A Perspect*; Matisons, J. G., Ed.; Vol. 4.

(77) Tapia-Rojo, R.; Mora, M.; Board, S.; Walker, J.; Boujemaa-Paterski, R.; Medalia, O.; Garcia-Manyes, S. *Nature physics* **2023**, *19*, 52–60.

(78) Condat, L. *IEEE Signal Processing Letters* **2013**, *20*, 1054–1057.

(79) Colquhoun, D.; Sigworth, F. J. In *Single-Channel Recording*, Sakmann, B., Neher, E., Eds.; Springer US: Boston, MA, 1995, pp 483–587.

(80) Sakmann, B.; Neher, E., *Single-channel recording*; Springer Science+Business Media: New York, 2009.

(81) Clayden, N.; Hesler, B. *Journal of Magnetic Resonance (1969)* **1992**, *98*, 271–282.

(82) Wiscombe, W. J.; Evans, J. W. *Journal of Computational Physics* **1977**, *24*, 416–444.

(83) Gentin, M.; Vincent, M.; Brochon, J. C.; Livesey, A. K.; Cittanova, N.; Gallay, J. *Biochemistry* **1990**, *29*, 10405–10412.

(84) Landowne, D.; Yuan, B.; Magleby, K. L. *Biophysical journal* **2013**, *104*, 2383–2391.

(85) F.J. Sigworth; S.M. Sine; Sigworth, F. J.; Sine, S. M. *Biophysical journal* **1987**, *52*, 1047–1054.

(86) Hohenester, U.; Trügler, A. *Computer Physics Communications* **2012**, *183*, 370–381.

Appendix A

Materials and methods

For all solutions I used deionized water from a Millipore System (>$18\,\mathrm{M\Omega}$, Milli Q). Gold nanospheres with $40\,\mathrm{nm}$ were brought from BBI Solutions and used in the solid phase synthesis of plasmon rulers.
Buffers and solvents:
HEPES ((4-(2-hydroxyethyl)-1-piperazineethanesulfonic acid)) >99.5% (Sigma Aldrich), CTAB (hexadecyltrimethylammonium bromide) 99% (Sigma Aldrich), CTAC (hexadecyltrimethylammonium chloride) >98% (Sigma Aldrich), PBS tablets (Sigma Alrich), $MgCl_2$ (magnesium chloride >98% (Sigma Aldrich), KCl (pottassium chloride) >99% (Sigma Aldrich), TWEEN20 (polyoxyethylen(20)-sorbitan-monolaurat) (Sigma Aldrich), NaOH 1N (Roth), NaOH pallets analytical grade (Fisher Scientific), NaCl <99.5% (Fisher Scientific), H_2O_2 32-34% (Merck), Hydrochloric acid 37% (VWR), Sulforic acid 95% (VWR), Acetic acid glacial >99% (Fisher Scientific), Nitric acid >65% (Sigma Aldrich), THF (tetrahyrofurane) 99.8% analytical grade (Fisher Scientific), Acetone 99.8% (Fisher Scientific), DMSO (dimethyl sulfoxide) 99.7% extra dry (Arcros Chemicals), Ethanol absolute (Sigma Aldrich), Toluene 99.8% (Fisher Scientific, Merck), Isopropanol (VWR), Methanol (VWR), Ethylacetate (VWR),
Nanoparticle synthesis and functionalization
$HAuCl_4$ (chloroauric acid) (Sigma Aldirch), L(+) ascorbic acid food grade (AppliChem), $NaBH_4$ >99% (sodium borohydride) (Sigma Aldrich), Bleach Florcal Au de Javel (hardware store), SMCC (succinimidyl-4-(N-maleimidomethyl)cyclohexane-1-carboxylate) (Thermo Scientific), TCEP (tris(2-carboxyethyl)phosphine) (Merck), HS-PEG-Biotin (3kDa) (Iris Biotech), HS-PEG-MeOH (2kDa) (Iris Biotech), HS-PEG-NH_2 (3kDa) (Iris Biotech)
Glass functionalization
Triethylamine >99.5% (Sigma Aldrich), ATPMS 97% (Sigma Aldrich), Copper sulfate pentahydrate >99% (Riedle Haen), APTES >98% ((3-Aminopropyl)triethoxysilane) (Roth), BSA >98% (bovine serum albumin) (Sigma Aldrich), Alkyne-PEG-$Si(OMe)_3$ (5 kDa) (Iris Biotech), MeO-PEG-$Si(OMe)_3$ (2 kDa) (Iris Biotech), Biotin azide (Azide-PEG3-Biotine Conjugate) (Merck)

A.1 Nanoparticle synthesis

Gold nanosheres of other diameter were synthesisized by Joahnnes Sutter according to the following protocol:
Seed synthesis

- $5\,\mathrm{mL}$ of $0.1\,\mathrm{mol\,L^{-1}}$ CTAC solution were mixed with with $50\,\mu\mathrm{L}$ of $0.05\,\mathrm{mol\,L^{-1}}$ $HAuCl_4$
- Under vigorous stirring $200\,\mu\mathrm{L}$ $NaBH_4$ of $0.02\,\mathrm{mol\,L^{-1}}$ were added
- After $3\,\mathrm{min}$ the mixture was diluted 1:10 with CTAC $0.1\,\mathrm{mol\,L^{-1}}$

Partilce growth

- $500\,\mathrm{mL}$ of $0.25\,\mathrm{mmol\,L^{-1}}$ CTAC were mixes with $1.25\,\mathrm{mL}$ of the prepared seed solution and $2\,\mathrm{mL}$ of $0.1\,\mathrm{mol\,L^{-1}}$ freshly prepared ascorbic acid
- Under vigorous stirring $2.5\,\mathrm{mL}$ of $0.05\,\mathrm{mol\,L^{-1}}$ $HAuCl_4$ were added and kept stirring for ca. $20\,\mathrm{s}$
- The mixture was left undisturbed at room temperature for ca. $1\,\mathrm{h}$

Etching of particles

- The paricle solution was separated to two batches of $250\,\mathrm{mL}$ each
- Under vigorous stirring $250\,\mathrm{mL}$ particle solution and $200\,\mu\mathrm{L}$ bleach from the hardware store were mixed for a few seconds. TEM images are shown in figure A.1 on the left.
- The second $250\,\mathrm{mL}$ particle solution were mixed with $250\,\mu\mathrm{L}$ bleach analogously. TEM images are shown in figure A.1 on the right.
- The mixtures were left undisturbed for $1\,\mathrm{h}$.

Washing:
The particle solutions were centrifuged at 10,000 RPM for $10\,\mathrm{min}$ and the supernatant removed. Particles were re-suspended in CTAC $25\,\mathrm{mmol\,L^{-1}}$ and the washing step repeated two times.

A.2 Protein purification

The protein was provided and purified by the group of Thorsten Hugel by the following protocol as in [8]:
"Hsp90 (Hsp82 in yeast, UniProtKB ID P02829) was expressed as a fusion protein with a C-terminal coiled-coil motif from the kinesin neck region of Drosophila melanogaster (DmKHC) that prevents dimer dissociation at picomolar concentrations in single molecule experiments1. Wild-type yeast

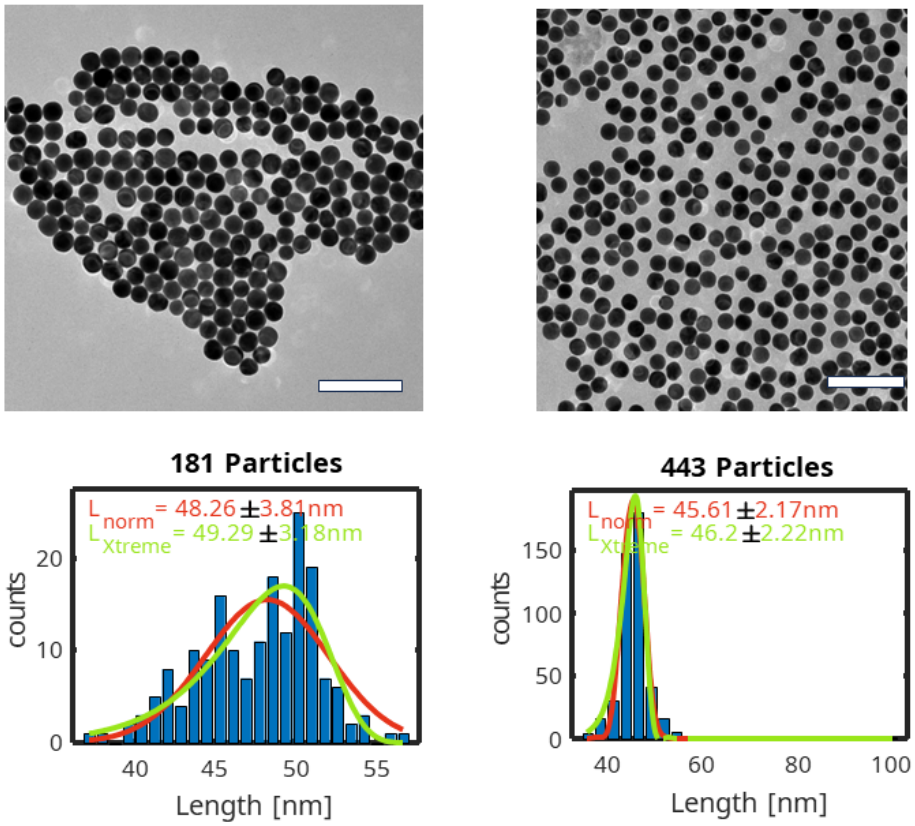

Figure A.1: Example TEM images of the nanoparicels used and corresponding size distributions below Left: Nanoparticles were treated with $200\,\mathrm{L}$ bleach, right shows partilces treated with $250\,\mu\mathrm{L}$ bleach per $250\,\mathrm{mL}$ particle solution. Scale is $200\,\mathrm{nm}$

Hsp90,containing no cysteines, was modified by site-directed mutagenesis (QuikChange Lightning, Agilent, Santa Clara, California) to attach exactly one fluorescent dye or gold nanoparticle per subunit of the Hsp90 dimer. For the plasmon ruler experiments, the T285C mutant with a non-cleavable N-terminal His-tag and a Strep-tag at the far C-terminus was used. Single molecule FRET (smFRET) experiments were conducted with a N298C single cysteine variant which additionally carries a tag for in vivo biotinylation (AviTag) at the far C-terminus. The N-terminal His-SUMO-tag is cleaved during purification. The Hsp90 constructs are contained in pET28 vectors and expressed from Escherichia coli BL21 (DE3) or BL21 Star (DE3) cells in the case of AviTag constructs (Thermo Fisher Scientific, Waltham, Massachusetts).Standard expression was done in LB medium supplemented with $50\,\mu g\,mL^{-1}$ kanamycin at $37\,^{\circ}C$ and inoculation from an over-night culture (1:100). Cells were induced at an OD600 of 0.6 by addition of $1\,mmol\,L^{-1}$ PTG. After 3 hours, the cells were harvested by centrifugation (20 min, $4\,^{\circ}C$, 3000 rpm, JLA 8.1, Avanti JXN-26, Beckman Coulter), resuspended in phosphate buffered saline (PBS) and pelleted again (10 min, $4\,^{\circ}C$, 4700 rcf Rotanta 460R, Hettich, Tuttlingen, Germany). For in vivo biotinylation, the biotin ligase (BirA) is co-expressed from pBirAcm (Avidity LLC, Aurora, Colorado) following the manufacturer's instructions. Briefly, TB medium was supplemented with 0.5% glucose and $30\,\mu g\,mL^{-1}$ kanamycin. Expression was induced at an OD600 of 0.7 by adding 1 mM IPTG and $50\,\mu mol\,L^{-1}$ d-biotin (from a 5 mM stock, in warm 10 mM bicine buffer pH 8.3, filter-sterilized). After induction for 3 h at $37\,^{\circ}C$, cells were harvested by centrifugation, washed with PBS and pelleted again. For purification, the cells were re-suspended in approximately 30mL PBS and lysed with a Cell Disruptor (Constant Systems) at 1.6 kbar. Cell debris was pelleted by centrifugation at 30000g at $4\,^{\circ}C$ for 45 min (JA-25.50, Avanti JXN-26, Beckman Coulter) and the supernatant was cleared by additional filtration (Filtropur S 0.45, Sarstedt, Nümbrecht, Germany). To prepare the protein for the plasmon ruler experiment, the solution was applied to a gravity flow Strep-Tactin column (IBA GmbH, Göttingen) and eluted according to the manufacture's protocol. For the smFRET construct, 20 mM imidazole was added from a 1 M stock, the solution was applied to a 5 mL HisTrap HP (GE Healthcare, Freiburg, Germany) and eluted by a linear gradient from 20 to 500 mM imidazole in 50 mM sodium phosphate pH 8.0, 300 mM NaCl at $8\,^{\circ}C$. Protein-containing fractions were pooled and dialyzed against the imidazole-free buffer overnight in the presence of 1/100 equivalent SENP protease. This protease cuts off the N-terminal His-SUMO sequence, leaving the native, tag-free protein2. The solution is again applied to the HisTrap column and the flow-through is collected and diluted 1:3 with MilliQ water to decrease the ionic strength. Both constructs were then applied to a HiTrap Q HP 5mL (GE Healthcare) and the protein was eluted with a linear gradient from 50 mM to 1 M NaCl in 40 mM HEPES pH 7.5. Hsp90 fractions were pooled and concentrated using centrifugal filters with a 50 kDa molecular weight cut-off (Amicon Ultra, Merck Millipore, Darmstadt, Germany). Finally, the protein was applied to a gel filtration

column (HiLoad 16/600 Superdex200, GE Healthcare) and eluted with 40 mM HEPES, 200 mM KCl pH 7.5. Peak fractions were again pooled and concentrated to 50-100 $\mu\mathrm{mol\,L^{-1}}$"

A.3 Building of the microfluidic cells

The microfluidic cells (flowcells) were build from cover slips (borosilicate 24x60 mm) acquired from VWR. The hole for the tubing were cut out with a Trotec Speedy 300 laserengraver. The separating layer between the slides consists of a piece of "Parafilm" with cut rectangular channels. The Parafilm is placed between both cover slips and the sandwich places on a pre-heated heating plate with ca. $100\,^{\circ}\mathrm{C}$. Light pressure is applied to the glass surface to evenly seal the surfaces with the melting parafilm and places in a holder for cooling. To clean the flowcells prior to an experiments the channel used for the measurement is flushed with Hellmanex™(diluted to ca. 30% in water) for five minutes. Afterwards the flowcell was flushed with water for five minutes. If residues remained the cleaning was repeated.

A.4 Microscopy setup and measurement procedure

I used two different microscopy setups in my experiments. Both are modified zeiss darkfield microscopes, one upright and one inverted. For the illumination I used LEDs with center wavelengths of $590\,\mathrm{nm}$ (M590L4) and $625\,\mathrm{nm}$ (M625L4) from Thorlabs. For white light illumination, I used a halogen lamp. Spectral images were taken by inserting a Thorlabs VariSpec Kurios VB1 into the light path of the halogen lamp, to illuminate with a single wavelength. The objective used was a plan-apochromat 40x 1.3 objective also from Zeiss and a Hamamatsu Orca flash 4.0 CMOS camera was used for image and time series acquisition. The data acquisition and processing was done by self written (by Karl Wandner and Sirin Celiksoy) Matlab software. The measurement principel is based on the work of Sirin Celiksoy [44].
After the flowcell was placed in the microscope at least on day priot to the experiment and cleaned with Hellmanex™, dilluted nanoparticles samples are flushed in and the particles randomly deposited on the glass. All experiments with the HSP90 protein were carried out in HEPES buffer with pH 7.4 and $50\,\mathrm{mmol\,L^{-1}}$ KCl and $10\,\mathrm{mmol\,L^{-1}}$ $MgCl_2$ in a temperature controlled room at $21\,^{\circ}\mathrm{C}$.

A.5 BEM simulation

I performed BEM simulations for the expected singnals upon dimerization and conformational changes for different sized of nanoparticles. For the simulation I used the MNPBEM toolbox for MATLAB [86] and used the solver function for the full maxwell equations. Figure A.2 shows the caluclated scattering crosssection for a nanoparticle with $40\,\mathrm{nm}$ dimeter (black) and the scattering crosssection of a dimer of two of this nanoparticle (blue and orange). For the calculation of the scattering spectra of the dimers, I used polarized light along the longitudinal axis to only excite the dimer mode of the coupled plasmon. The resonance wavelength shifts towards longer wavelength and the scatterin intensity strongly increases as expected. Since nanoparticles in reality are polydisperse, nanoparticles of different sized are present in the experiment. I repeated the simulation for different diameter of particles from $30\,\mathrm{nm}$ to $90\,\mathrm{nm}$ and calculated the resonance wavelength from fitting a lorentz function. Figure A.2 b shows the change in the resonance wavelength $\Delta\lambda_{res}$ between monomer and dimer together with the relative change in the maximum scatterin intensity ($I_{max,dimer}/I_{max,monomer}$ against the particle diameter. The figure shows the calculated valued for three different distances between the nanoparticle which correspond to the distances of the experiments with HSP90. The open conformation ($22\,\mathrm{nm}$, triangles), equilibrium distance ($19.5\,\mathrm{nm}$, circles) and closed conformation ($17\,\mathrm{nm}$, crosses). With increasing diameter the change in the resonance wavelength increases wich is in agreement with the plasmon ruler equation (see chapter 2 and [**empty citation**]). The maximum scattering intensity increases by a factor of at least three and reaches a maximum of six for particles with a diameter of ca. $45\,\mathrm{nm}$. Therefore nanoparticles of this size should be clearly distinguishable from dimers formed from those nanoparticle due to the large increase in scattering intensity upon dimerization. In my exeriments I use the single line detection method of Sirin Celiksoy [44] with a LED as a light source. To estimate the maximum signal for a HSP90 plasmon ruler

Additionally, I performed BEM simulations of the fluctuation of a single gold nanosphere against the surface to check whether the recorded signals with low amplitude (about two percent difference in intensity between both states) could be causes by a single particle. Figure A.3 shows a sketch of the dimensions used for the simulation. The refractive index of the glass surface was set to 1.5 and the surrounding medium has a refractive index of 1.33 for water. In the simulation I used nanparticles with a diameter of $48\,\mathrm{nm}$ in water. I disregarded the PEG layer around the nanoparticle and the protein which have a refractive index higher than water. The scattering cross section was estimated by solving the Maxwell equations and is shown in figure A.3 b for a distance of one nanometer and twenty nanometer to the surface.

The distance between the binding sites on the HSP90 were measure to

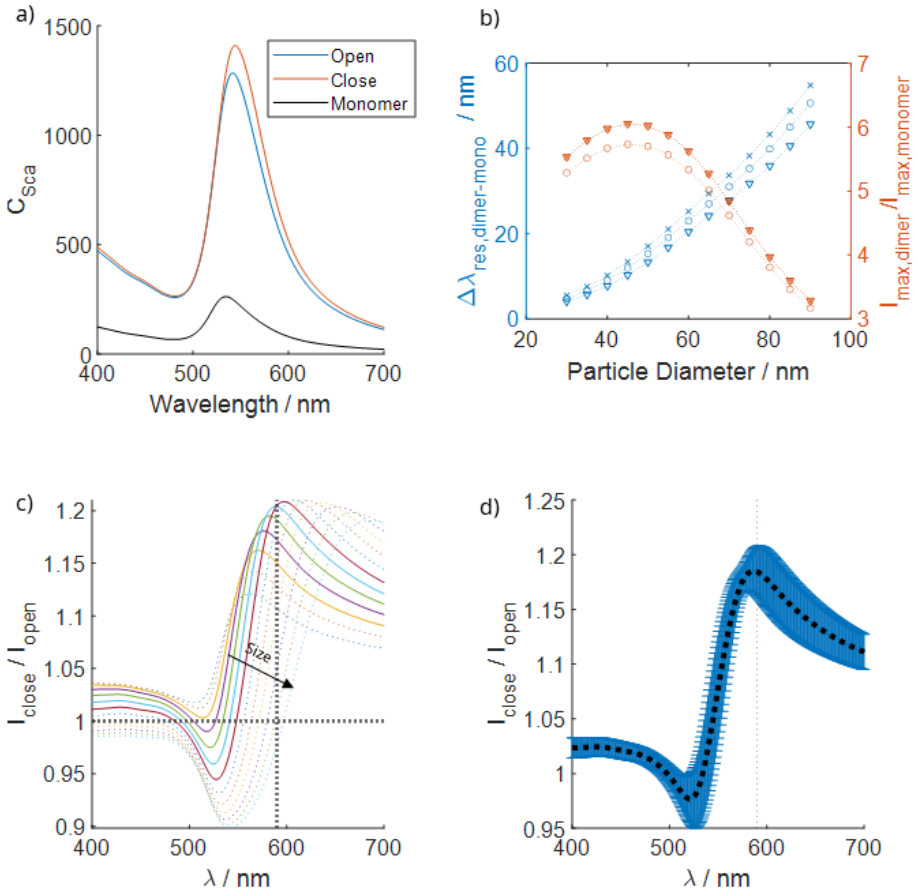

Figure A.2: BEM Simulation of plasmon rulers with different particle sizes. A: Scattering crosssection calculated from the maxwell equations for a single nano particle ($40\,\mathrm{nm}$ diameter) in water (black curve). Blue and orange show the scattering crosssection for a dimer of two nanoparticles (both $40\,\mathrm{nm}$ diameter) with distances of $17\,\mathrm{nm}$ (blue) for the open conformation of HSP90 and $22\,\mathrm{nm}$ (orange) for the closed conformation. B: Change in the resonance wavelength and maximum scattering intensity upon dimerization for different diameters. Markers indicate different distances between the nanoparticles (triangles $22\,\mathrm{nm}$, circles $19.5\,\mathrm{nm}$ and crosses $17\,\mathrm{nm}$). With increasing diameter the change in the resonance wavelength increases, the relative increase of the scattering intensity reaches a maximum at ca. $45\,\mathrm{nm}$. C: Intensity change between closed and open conformation (distance change from $17\,\mathrm{nm}$ to $22\,\mathrm{nm}$) plotted against the wavelength for different sized of nanoparticles. The larger the nanoparticle, the higher the wavelength that yields the largest signal. Particles size was varied in $5\,\mathrm{nm}$ steps from $30\,\mathrm{nm}$ to $90\,\mathrm{nm}$. Solid lines indicate particles sized from $40\,\mathrm{nm}$ to $60\,\mathrm{nm}$ which is in the range of the nanoparticles of $48\,\mathrm{nm}$ that I used. Dotted lines mark the location of the LED (SI595 and one which corresponds to no signal) D: Expecred signal for SI48 nanopartiles depending on the wavelength. Datapoints calculated from the average calculated realtive signal of particles sized $40\,\mathrm{nm}$ to $60\,\mathrm{nm}$, errorbars represent the standard deviation. Red dotted line marks the wavelength of the LED ($595\,\mathrm{nm}$) which gives a maximum signal of ca. 20%.

be $7.5\,\mathrm{nm}$ in the closed conformation and $12.2\,\mathrm{nm}$ in the open conformation by Leonie Vollmar and Julia Schimpf. In the previous publication [8] the PEG layer was said to be four nanometers. I used a thickness of three nanometers and a HSP90 distance in the closed conformation of eight nanometers.

To see the potential difference in the measured intensity, I calculated the integral over the scattering cross section for distances corresponding to the open and closed conformation. Figure A.3 c shows the relative intensity change from the open to the closed conformation calculated for the used LED with $\lambda = 595\,\mathrm{nm}$ (integral calculated from $590\,\mathrm{nm}$ to $600\,\mathrm{nm}$). With a change from $16\,\mathrm{nm}$ from the open conformation to $11\,\mathrm{nm}$ in the closed conformation to the surface, the scattering intensity increases by 1.2%. The same calculation was done for the illumination with a halogen lamp and filters from $535\,\mathrm{nm}$ to $700\,\mathrm{nm}$ with the relative intensity change shown in figure A.3 d. Here the intensity change also amount to 1.2%. The calculated intensity change is similar to the recorded intensity changes of ca. 2%. It is possible that the recorded time series show signals from single proteins but were not dimers of plasmonic nano particles. Further investigation of this requires a passivated surface to which the protein can bind. Then the particle can be flushed in in a second step to bind to the protein. If then a signal is measurable, this could significantly improve yield and simplify the assembly.

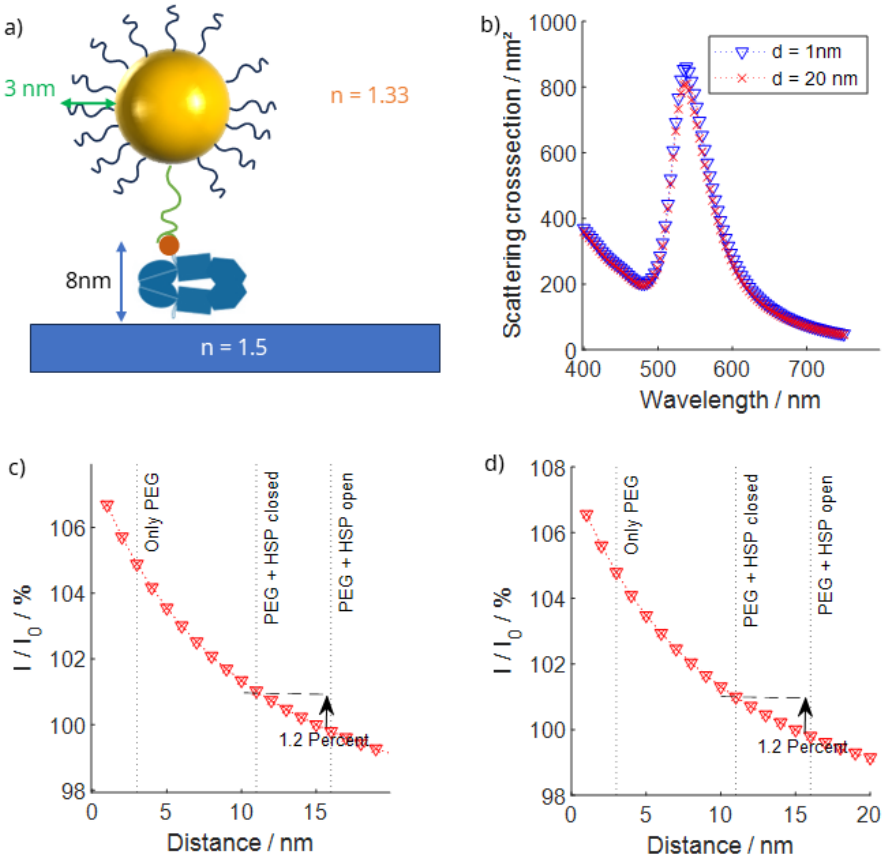

Figure A.3: BEM simulation of signal particle against surface. A: Sketch of the distances and refractive indexes in the simulation. The thickness of the PEG functionalization was set to three nanometers and the end to end distance of HSP90 rounded to eight nanometers. B: Scattering cross section simulated by BEM and solving of the Maxwell equations. Blue for a distance of $1\,\mathrm{nm}$ to the glass surface and red for $20\,\mathrm{nm}$. C: Relative change of intensity calculated from the integral of the scattering cross section against the distance to the surface. The integral was calculated from $590\,\mathrm{nm}$ to $600\,\mathrm{nm}$. D: Relative change of intensity calculated from the integral of the scattering cross section against the distance to the surface. The integral was calculated from $535\,\mathrm{nm}$ to $700\,\mathrm{nm}$. Dotted lines indicate layer thicknesses.

Appendix B

Solid phase synthesis

All HSP90 experiments were carried out in HEPES buffer containing MgCl KCl HEPES with pH 7.4

B.1 Solid phase synthesis protocol

Chemicals / Materials: Buffers All Buffer must be filtered before use!:

- HSP90-Buffer: 40 mM HEPES, 50 mM KCl, 10 mM MgCl2, pH=7,4
- PBS pH=7.4
- PBS pH=6.7

Particles:

- NP B1|200 JS (CTAC Stabilized)
- NP BBI Solutions (Citrate stabilized)

Proteins:

1. Streptavidin-aliquot 50 µL 1mg/mL stored at -20 °C
2. HSP90-aliquot: 5µL 75 µM stored at -80 °C

Others:

1. PEGylated and biotinylated (1%) glass slides
2. SMCC stored at 4°C
3. DMSO
4. TCEP 100 mM in 0.3 M NaOH

Prepare Solutions: SMCC: Prepare Solution of 20mg/mL SMCC in DMSO. Take 5 µL thereof and dilute with 250 µL PBS, filter through Syringefilter to remove crystals and dust. PEG Solutions: Prepare 10 mM PEG-solutions of HS-PEG-Biotin 3000 (b-PEG), HS-PEG-OMe 2000 (m-PEG) and HS-PEG-NH2 3000 (a-PEG)

- a-PEG: 30,227 µl/mg
- b-PEG: 30,976 µl/mg
- m-PEG: 51,316 µl/mg

Prepare PEG-mixtures (two times each) Default:

1. 87 µL m-PEG + 10 µL b-PEG + 3 µL a-PEG = MIX B
2. 85 µL m-PEG + 15 µL a-PEG = MIX A

Streptavidin: Dilute the Streptavidin aliquot (50µl) in 350 µl PBS 7,4 HSP90: Dilute the HSP90 Aliquot (2µl) in 528 µl PBS 7.4 and 4 µl TCEP. Incubate 10 min, dilute 10 µl in 990 µl PBS 7,4, and 10µl thereof in 990 µl PBS 7,4. Final concentration 0,24 nM. Particle functionalization: CTAC Particles:

- Take 200 µl and dilute with 200 µl mQ Water, centrifuge for 5 min @ 6000 RPM. Remove supernantant and disperse the pallet in 100 µL MIX A
- Incubate for 2h under sonification (20

Repeat for MIX A or use Citrate stabilized Particles Citrate Particles:

- Take 400 µL centrifuge for 5 min @ 6000 RPM. Remove supernantant and disperse the pallet in 100 µL MIX B
- Incubate for 2h under sonification (20% Power!)
- Centrifuge Particles for 5 min@6000 RPM, remove supernatant
- Washing with Water: redisperse in 400µl Water, hold Eppi shortly in Ultrasonicbath (20 sec @100% Power) .Repeat 2 Times. Disperse the Pallet in 100µl PEG MIX, incubate for 2h under sonification (20 power).
- Wash 2 times with water like described above.

After the final washing step: Particles from MIX B, dilute the pallet in 100µl PBS 7.4 , take 10µL thereof and dilute in 100µl PBS 7.4 this is the Biotin-Particle for the Experiment Particles form MIX A, wash 2 times with Water like above Dilute 30µL SMCC in DMSO in 400µl mQ Water and filter through syringe filter, dilute the Pallet in this solution and incubate 2 h Wash 4 times with mQ and centrifuge 3 min instead of 5. Resuspend the pallet in 50µl PBS 6.7

Dimer formation: Build flow cell consisting of one PEGylated and one biotinylated glass slide. Rinse the slides with water, blow dry with N2 and glue the slides together with parafilm.

- Flow in Streptavidin solution and incubate 10 min
- Rinse with PBS 7.4 for 5 min.
- Flow in the first Particle for 3 min.
- Flush with PBS 7.4 for 5 min to remove free Particles
- Flow in the SMCC in DMSO solution and incubate for 30 min
- Rinse with PBS 6.7 for 5 min
- Flow in HSP90 in Buffer and incubate 30 min
- Rinse with PBS 6.7 for 5 min
- TAKE SPECTRAL IMAGE! Exposuretime 5s
- Flow the second particle solution and let react for 30 min.
- Rinse with HEPES until all free particles are removed (use two tubes).
- TAKE SPECTRAL IMAGE
- TAKE SINGLE LINE IMAGE Exposuretime 0.1s
- START TIMESERIES

B.2 Example time series

Figure B.1 shows two example time series from the experiments Alena Kuzmina conducted with nanoparticles containing 100% amino groups synthesized via the MUA intermediate (refer to chapter 4 for details). Both time series show fluctuation between states (heatmaps) which stopped after incubation with AMP-PNP (below heatmap). The to time series shows more than two states in the last half hour of the time series and both time series various degrees of drift over the experimental duration.

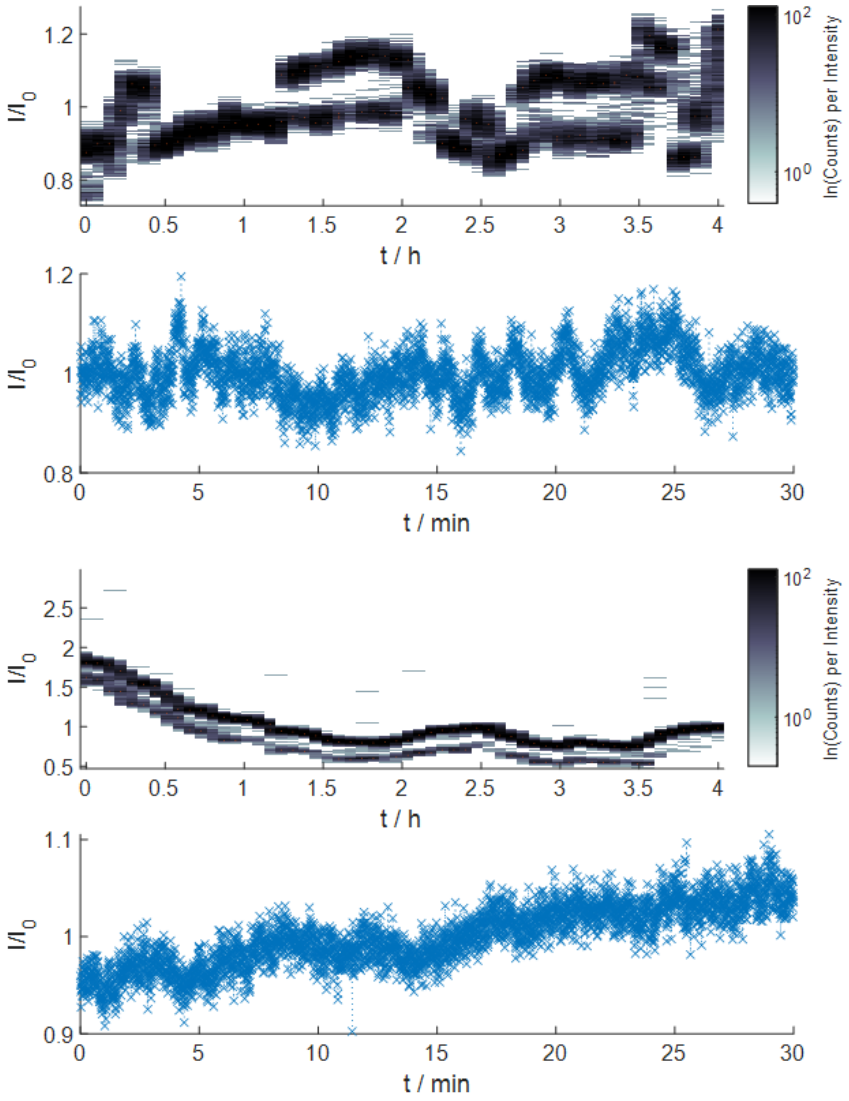

Figure B.1: Two example time series of four hours and time resolution of $0.5\,\mathrm{s}$. Top shows the time series as a heatmap, below the time series of the same nanoparticle after incubation with AMP-PNP. The previously seen fluctuation between two states is stopped as it is known for HSP90.

Appendix C

Passivation of glass surfaces

C.1 Silanization in toluene

The following protocol was used for the silanization of glass slides.
Toluene was dried with a molecular sieve for at least over night before use.
Cleaning of coverslips

- Place coverslips in a teflon holder and incubate in piranha (H_2SO_4 : H_2O_2 3:1) for $1\,\mathrm{h}$
- Transfer glasses in holder to water
- Wash with de-ionized water from squirt bottle three times
- Blow dry with stream of nitrogen

PEGylation

- Put coverslips in holder in the reaction vessel under Argon stream
- Fill up with dry toluene
- Add pre-dissolved PEG components in toluene (99:1 silane-PEG-OMe:silane-PEG-alkine) to achieve a final concentration of $0.25\,\mathrm{mmol\,L^{-1}}$
- Add two to three drops of triethyleamine
- Keep temperature at $80\,^{\circ}\mathrm{C}$ over night for reaction
- Flush coverslips with ethyl acetate from the squirt bottle, sonicate in ethyl acetate for $5\,\mathrm{min}$

- Flush coverslips with methanol from the squirt bottle, sonicate in methanol for $5\,\mathrm{min}$
- Flush with methanol from the squirt bottle
- Flush dry under nitrogen stream

Biotinylation - Click chemistry

- prepare reaction solution of $250\,\mu\mathrm{L}$ per coverslip which contains: $100\,\mathrm{mmol\,L^{-1}}$ TRIS (pH 9.5), $100\,\mathrm{mmol\,L^{-1}}$ ascorbic acid, $150\,\mu\mathrm{mol\,L^{-1}}$ biotine azide and $1\,\mathrm{mmol\,L^{-1}}$ copper sulfate
- add copper sulfate last as this starts the reaction prepare reaction chamber
- put a piece of tissue paper in a petri dish and moisturize it
- place parafilm with the paper side on the wet tissue click reaction
- place a drop of $250\,\mu\mathrm{L}$ reaction solution on the parafilm
- place slide on the drop, make sure the drop spreads to the full surface
- close the petri dish
- let react for $2\,\mathrm{h}$
- wash coverslips with buffer
- blow dry with stream of nitrogen

C.2 Passivation Protocol from the group of Thorsten Hugel

Coverslips **Pre-Cleaning**:

- Sonicate coverslips in fresh 2% Hellmanex (1-2x)
- Wash with H_2O
- Sonicate in fresh H_2O
- Sonicate in 50/50 Isopropanol/H_2O or 50/50 Ethanol/ H_2O
- Wash with H_2O
- Sonicate in fresh H_2O

(Optional) Piranha-Cleaning:

  - Slowly add H_2O_2 (30%) to H_2SO_4 in a ratio of 1:3 (do it on ice)
  - Put your slides/coverslips in the mixture
  - Put it in the oven at 60°C for 2h
  - Wash the coverslips with H_2O
  - Sonicate them in Hellmanex™(2
  - Sonicate them 2x in H_2O

RCA-Cleaning:

- Mix H_2O, NH_3 (30%) and H_2O_2 (30%) in a ratio of 5:1:1
- Put your slides/coverslips in the mixture
- Put it in the oven at 60°C for at least 2h
- Wash it properly with H_2O

Passivation:

- Wear disposable gloves whenever you have to touch the slides.
- Place two pipettes on top of wet paper tissues that are laid out flat.
- Put half of the coverslips onto the pipettes.
- Pipette methoxy-PEG-silane solution ($80\,\mu L$) onto them.
- Create 'sandwiches': put a second coverslip on top of the first one.
- Keep 'sandwiches' at RT for 2 h.
- Wash off unbound PEG under running ultrapure water.
- Dry slides with nitrogen gas. Store them dark and dry.

C.3 Passivation protocol provided from Biswajit Pradhan

Coverslip:

- Size : 24 mm x 60 mm, No.1.5 (thickness 170 μm), borosilicate. (Cat.-No.631-0147, VWR Intl).
- Place the coverslip in the teflon holder. (5 min)
- Rinse 1 time with KOH 1 M solution, and then sonicate for ≈ 30 min.
- Rinse 1 time with MilliQ water and let the cover slips immersed in water while Piranha etching the glass slides.

Slides cleaning II: Piranha etching (82 min/ 1.5 hrs)

- Take Hydrogen peroxide solution bottle from the fridge. (5 min)
- (Clean up the space inside of the Piranha hood, make space for the reaction). (1 min)
- (Put aluminum foil on the bottom for showing that you are working with Piranha). (1 min)
- Wash the glass slide holder and the beaker with tap water.
- Take sulfuric acid and bring it inside of the hood (For this, wear the additional turquoise color coat and take the thick black or red gloves beforehand).
- Place the glass slides in the 3-column holder.
- Pour $\approx$ 250 ml of sulfuric acid in the beaker.
- Pour $\approx$ 50 mL of Hydrogen peroxide solution in the beaker (or the amount till it reaches $>= 90\,\mathrm{C}$.). (... 10 min)
- Measure the temperature of the mixture. For this, use the thermometer and do not touch its middle part cause there is Piranha.
- Bring the Hydrogen peroxide bottle back to the fridge and Wait for the etching till the temperature reaches $>= 35\,\mathrm{C}$, which takes $\approx$ 30 min. (30 min)
- Take the holder out and transfer the glass slides to the small holder.
- Transfer the piranha into the piranha-trash. Bring the beaker + 3-column holder to the sink and pour tap water for a while so that all the leftover Piranha is diluted. (5 min)
- Pour MilliQ water into the small glass slide holder. Sonicate for $\approx$ 20 min. (20 min)
- Take methanol bottle next to the ultrasound sonicator (with thick gloves), rinse the glass slides with methanol 1 time and then pour methanol into the holder and sonicate for 10 min. Keep the beaker+ 3-column holder inside of the hood. (10 min)

Both cleaning (I and II) should be performed simultaneously and can be finished within 2 hours.

Silanization: 90 min + 120 min

- 30 min incubation of the slides in silane-reaction-solution = 1% silane + 5% glacial acetic acid + Methanol. (30 min) (2 mL silane, 10 mL glacial, 188 mL methanol)

- Rinse the slides with Methanol (at least twice) and then put them in the oven ($70\,^{\circ}\mathrm{C}$) for an hour. Few hours or overnight incubation is okay. (60 min)

Pegylation: 46 min, overnight waiting

- Put 800 µL of Borate pH 8 buffer in $-20\,^{\circ}\mathrm{C}$ freezer. Take it out before it freezes but remains ice cold ($\approx 0\,^{\circ}\mathrm{C}$).
- take mPEG-sva and biotinPEG-sva bottle from $-201\,^{\circ}\mathrm{C}$ freezer (keep the bottle in dark). Thaw them to come to room temp. (10 min)
- take 1.5 mL centrifuge tube. put 80 mg of mPEG (for 10 glass slides + cover slips). put 2 mg of biotinPEG. (2 min)
- Dissolve in 200 uL of DMSO.
- add 800 µL of Borate ($0\,^{\circ}\mathrm{C}$), mix it by pipetting (do it right before the PEGtylation, should be fresh). (2 min)
- Centrifuging the solution with max. speed for 10 s to remove bubbles. (1 min)
- Gently drop a solution over a microscope slide (1) (70uL of the solution for 40 mm coverslip, 90uL of the solution for 50 mm coverslip). Place a cover slip (2) on the top of it gently. Put again a drop of peg-solution and place a microscope slide (3). Repeat this process for the 10 slides. The top and bottom slide can be the coverslip as they are cheap and can be thrown away. This way both sides of the slides will be functionalized. (10 min)
- Put the stack of the slide in a humidifying box and store it at $4\,^{\circ}\mathrm{C}$ overnight.
- Next day morning, rinse each one with squid water, then dry with nitrogen.
- Put one quartz slide and one coverslip in amicon, blow N2, tighten the lid and wrap it with parafilm film. Store them at $-20\,^{\circ}\mathrm{C}$. (20 min)

C.4 Reaction conditions overview

C.5 Tested reaction conditions for passivation of glass

Table C.1: Overview over reaction conditions used in silanization of glass surfaces.

Silanization Agent	Solvent	Temperature	Time	pH	Notes	Source
3-aminopropyltriethoxysilane 10 % vol in solvent	Toluene water free 1 % diisopropylethylamine	80°C	1-24h	basic	Stiring,dyed after reaction an cleaning @110°C for 10 min	Benters, R.; Niemeyer, C. M.; Wöhrle, D. Dendrimer-Activated Solid Supports for Nucleic Acid and Protein Microarrays. ChemBioChem 2001, 2 (9), 686–694. DOI: 10.1002/1439-7633(20010903)2:9<686:AID-CBIC686>3.0.CO;2-S.
3-aminopropyltriethoxysilane 10 % vol in solvent	Toluene,1 % diisopropylethylamine 100ppm water	80 °C	1-24h	basic	Stiring, dyed after reaction an cleaning @110°C for 10 min	Benters, R.; Niemeyer, C. M.; Wöhrle, D. Dendrimer-Activated Solid Supports for Nucleic Acid and Protein Microarrays. ChemBioChem 2001, 2 (9), 686–694. DOI: 10.1002/1439-7633(20010903)2:9<686:AID-CBIC686>3.0.CO;2-S.
3-aminopropyltriethoxysilane 2 % vol in solvent	Ethanol 95%	RT	1-24 h	neutral	Stiring, dyed after reaction an cleaning @110°C	Benters, R.; Niemeyer, C. M.; Wöhrle, D. Dendrimer-Activated Solid Supports for Nucleic Acid and Protein Microarrays. ChemBioChem 2001, 2 (9), 686–694. DOI: 10.1002/1439-7633(20010903)2:9<686:AID-CBIC686>3.0.CO;2-S.
(3-mercaptopropyl)trimethoxysilane 50% vol	THF 0.4% HCl	RT	30 s	acidic	Spin coated, Dryed @150°C for 3h	Bertin, A.; Schlaad, H. Mild and Versatile (Bio-)Functionalization of Glass Surfaces via Thiol–Ene Photochemistry. Chem. Mater. 2009, 21 (24), 5698–5700. DOI:
3-(Mercaptopropyl)trimethoxysilane	None	100°C	30 min	-	Vacuum during reaction	Chen, J.-J.; Struk, K. N.; Brennan, A. B. Surface modification of silicate glass using 3-(mercaptopropyl)trimethoxysilane for thiol-ene polymerization. Langmuir : the ACS journal of surfaces and colloids 2011, 27 (22), 13754–13761. DOI: 10.1021/la202225g.
Tri(methoxy)silane- PEG (2 kDa)	Dry toluene + 25µM triethylamine	80°C	12 h	Basic	Nitrogen atmosphere	Schenk, F. C.; Boehm, H.; Spatz, J. P.; Wegner, S. V. Dual-functionalized nanostructured biointerfaces by click chemistry. Langmuir : the ACS journal of surfaces and colloids 2014, 30 (23), 6897–6905. DOI: 10.1021/la5007661.
Tri(ethoxy)silane-PEG (5kDa) 25 wt % in solvent	DMSO (dry)	90 °C	15 min	Neutral	-	Gidi, Y.; Bayram, S.; Ablenas, C. J.; Blum, A. S.; Cosa, G. Efficient One-Step PEG-Silane Passivation of Glass Surfaces for Single-Molecule Fluorescence Studies. ACS applied materials & interfaces 2018, 10 (46), 39505–39511. DOI: 10.1021/acsami.8b15796.
3-aminopropyltriethoxysilane 1 % vol in solvent	Toluene dry	RT	24 h	neutral	Inert condition in reaction vessel	Hasan, A.; Pattanayek, S. K.; Pandey, L. M. Effect of Functional Groups of Self-Assembled Monolayers on Protein Adsorption and Initial Cell Adhesion. ACS biomaterials science & engineering 2018, 4 (9), 3224–3233. DOI: 10.1021/acsbiomaterials.8b00795. Published Online: Aug. 22, 2018.
3-aminopropyltriethoxysilane 5 %	Isopropyl alcohol	60 °C	unspecified	neutral	5 % water added @ 60°C	Ercole, C.; Del Gallo, M.; Mosiello, L.; Baccella, S.; Lepidi, A. Escherichia coli detection in vegetable food by a potentiometric biosensor. Sensors and Actuators B: Chemical 2003, 91 (1-3), 163–168. DOI: 10.1016/S0925-4005(03)00083-2.
3-aminopropyltriethoxysilane 0.4%	Water	75°C	2 h	pH 3 (adjusted by HCl 0.1M)	-	Campbell, G. A.; Mutharasan, R. Detection of pathogen Escherichia coli O157:H7 using self-excited PZT-glass microcantilevers. Biosensors & bioelectronics 2005, 21 (3), 462–473. DOI: 10.1016/j.bios.2004.11.009. Published Online: Dec. 21, 2004.
3-aminopropyltriethoxysilane 1%	Methanol + 5% glacial acetic acid	RT	30 min	acidic	Flamed before reaction, backed 65°C 3h after incubation	Pradhan, B.; Engelhard, C.; van Mulken, S.; Miao, X.; Canters, G. W.; Orrit, M. Single electron transfer events and dynamical heterogeneity in the small protein azurin from Pseudomonas aeruginosa. Chem. Sci. 2019, 11 (3), 763–771. DOI: 10.1039/C9SC05405G. Published Online: Nov. 27, 2019.
Tri(methoxy)silane PEG 80mg/600µL solvent	10mM HCl	RT	2h	Acidic	-	provided by the group of Thorsten Hugel

Table C.2: Tested variations of the passivation protocol from the group of Thorsten Hugel. Plasma cleaner "old" refers to the plasma cleaner of the Sönnichsen group and "new" to the plasma cleaner of the Seiffert group.

	Cleaning				Surface Molecule				Solvent						
slide	Acid Pirranha	RCA	Plasma old	Plama new	Methoxy PEG (2kDa)	biotin PEG (3kDa)	Alkyl Silan	APTMS	EtOH	MeOH +5% Acetic acid	HCl	Oven	Concentration	Time & Temp.	Contact angle
1			x		x						x		80 mg / 600 µL	2 h, RT	31,7 °
2															35,4 °
3															34,6 °
1			x		x						x		8 mg / 600 µL	2 h, RT	30,4 °
2															30,3 °
3															30,2 °
1				x	x						x		80 mg / 600 µL	2 h, RT	34,2 °
2															35,1 °
3															34,4 °
1				x	x						x		8 mg / 600 µL	2 h, RT	30,0 °
2															29,3 °
3															32,1 °
1				x	x				x				8 mg / 600 µL	2 h, RT	17,4 °
2															14,4 °
3															27,4 °
1				x					x				8 mg / 600 µL		
2															
3															
1				x	5 kDA						x		80 mg / 600 µL		
2															
3															
1		X			X						X		80 mg / 600 µL	1,5h RT	
1		X			X						X	X	80 mg / 600 µL	1,5h RT	
1		X			X					X		X	80 mg / 600 µL	1,5h RT	
1		X			X					X			80 mg / 600 µL	1,5h RT	
1		X					X			X		X	80 mg / 600 µL	1,5h RT	
1		X						X		X		X	1%	1,5h RT	
1		X					X		X			X	2%	1,5h RT	
1	X	X						X	X			X	2%	1,5h RT	
1	X	X						X	X				2%	1,5h RT	

Appendix D

Batchsynthesis

For all reactions the nanoparticles with average diameter of $48\,\mathrm{nm}$ were used. Synthesis according to A.

D.1 Nanoparticle Functionalization

- Take 50 µL from the nanoparticle stock and centrifuge at 6000 RPM for 5 min
- Remove the supernatant and wash the nanoparticles with H2O (milli-Q)
- first washing step with 50 µL H_2O (milli-Q)
- In the meantime, prepare the PEG solution:
- 10 mM PEG-NH_2 in Hsp-buffer and 10 mM PEG-MeO in Hsp-buffer
- Mix 60% of PEG-NH_2 with 40% PEG-MeO for the functionalization
- Add 100 µL of the PEG mixture to one pellet of nanoparticles and shake it well
- Incubate the reaction at room temperature over night!

Prepare a lot of functionalized nanoparticles and store the PEGylated stock at -80°C for further use!

D.2 Batch Synthesis Protocol

- Take 20 µL of the PEGylated gold nanospheres (Au@PEG)

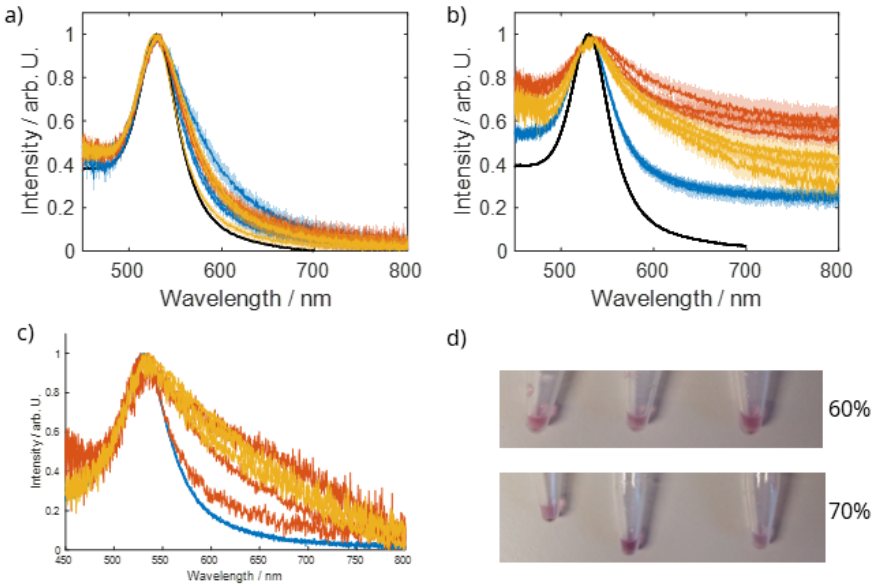

Figure D.1: Example ensembel spectra of the functionalized gold nanoparticles after the functionalization and washing. All samples show three spectra from individual samples. A: Nanoparticles functionalized with 60% HS-PEG-NH_2 in PBS pH 6.7. Black is a spectrum taken from the stock solution without functionalization, blue in the functionalization solution, orange after washing once and yellow on the day after washing. B: Nanoparticles functionalized with 60% HS-PEG-NH_2 in water. Black is a spectrum taken from the stock solution without functionalization, blue in the functionalization solution, orange after washing once and yellow on the day after washing. C: Nanoparticles functionalized with 70% HS-PEG-NH_2 with PBS pH 6.7. Blue in the functionalization solution, orange after washing once and yellow on the day after washing. D: Color images of the resuspended nanoparticles after washing. Top shows particles functionalized with 60% HS-PEG-NH_2, which retained their pinkish color. Bottom hows particles functionalized with 70% HS-PEG-NH_2, which changed their color to a pastel purple which indicates aggregation.

- Add 5 µL Tween20 to the nanoparticle dispersion and centrifuge (left one!) at 6000 RPM for 5 min; Remark: After the addition of TWEEN20 use the 'Tischzentrifuge' for better mixing!
- Remove the supernatant and wash the nanoparticles with Hsp90-buffer; Remark: Filter the Hsp90-buffer with a Whatman filter 0.02 µm before the use!
- 1. washing step with 100 µL Hsp90-buffer + 5 µL TWEEN20
- 2. washing step with 50 µL Hsp90-buffer + 5 µL TWEEN20
- Resuspend the nanoparticles in 50 µL Hsp90-buffer and add 5 µL SMCC (240.000:1 amount of substance SMCC to particle for our particle concentration); Remark: Put SMCC in the cap and 'fling' the particles into the SMCC droplet. Use the 'Tischzentrifuge' so that everything comes down!
- Incubate for 10 min at room temperature without shaking
- Add 5µL Tween20 after the incubation time and centrifuge (left one!) at 6000 RPM for 5 min
- Remove the supernatant and wash the nanoparticles with Hsp90-buffer
- 1. washing step with 50 µL Hsp90-buffer + 5 µL TWEEN20
- Resuspend the nanoparticles in 30 µL Hsp90-buffer
- Measure a spectrum @ the Jasco Spectrometer and calculate the nanoparticle concentration

Remark: Use the 70 µL quartz cuvette; Dilute 1µL nanoparticle dispersion in 70 µl Hsp90-buffer for the measurement;

- Take 20 µl nanoparticles and add the calculated amount of HSP90 from the Hsp90 stock solution (0.24 nM); Remark: Take the Hsp90 out of the freezer and wait till it reaches room temperature before the addition!
- If you use prepared NP with PEG-SMCC aliquots start here
- Take 1 aliquot Nanoparticles from freezer and melt the pallet.
- Add HSP90 0.24nM to the Particles (amount written on top of the aliquot)
- Mix well
- Incubate for 10 min at room temperature without shaking
- Finally dilute your sample to 500 µL with Hsp90-buffer; Remark: The volume of Hsp90-buffer depends on the nanoparticle concentration!
- The sample is ready to measure!

D.3 Control experiment without HSP90

For the developed batch synthesis we performed a control experiment in which we did not introduce HSP90. We kept all other parameters the same and added the same volume of buffer that would have been added according to the determined concentration of nanoparticles. We recorded one hour time series and incubated the nanoparticles with AMP-PNP. Figure D.2 a and b show the histogram of the determined degree of fluctuation before and after incubation with AMP-PNP. Sections c and d show the histogram of the degree of fluctuation for the reaction without HSP90. The degree of fluctuation in the time series is similar for locked HSP90 and without HSP90.

However there was also a noticeable difference between the degree in fluctuation before and after incubation with AMP-PNP even when no HSP90 was used. Additionally we found that four time series conformed to the set filter criterion of 30% of time showing fluctuation. Two of those are shown in figure D.3. One shows strong drift and is an example of a falsely identified time series by the filter. The other one shows distinct fluctuation between three states. This fluctuation disappeared after the incubation with AMP-PNP. Since there is no HSP90 present, the fluctuation cannot be caused by the protein and must be caused by another source. One hypothesis is that two particles are close together on the surface and their distance is changed by the diffusion of the particles. In the subsequent incubation one of the particles could get flushed away or the stream of solvent reorients them so they can stably stick to the surface. An experiment with a passivated surface should be part of future research to check in this phenomenon is caused by interaction with the surface. Since the degree of fluctuation between locked HSP90 and a reaction without HSP90 is similar and the degree of fluctuation with HSP90 is an order of magnitude higher, the recorded fluctuations of HSP90 are most likely not an artifact and truly caused by the protein.

D.4 Additional time series

D.5 Variations in signal strength of plasmon rulers.

In the experiments conducted, I saw that the intensity change between the recorded states varies. Figure D.8 shows a histogram with bin width of 1% (0.01) for the differences in the relative intensity. Lower relative intensity differences are more common than large ones. Is is also of note that no intensity changes of the expected 20% from the BEM simulations (Appendix A) are present. In the simulation I only considered the excitation along the longitudinal axis. The light in the microscope shows light polarization of ca. 15° (information from Sirin Celiksoy from discussions). Therefore the

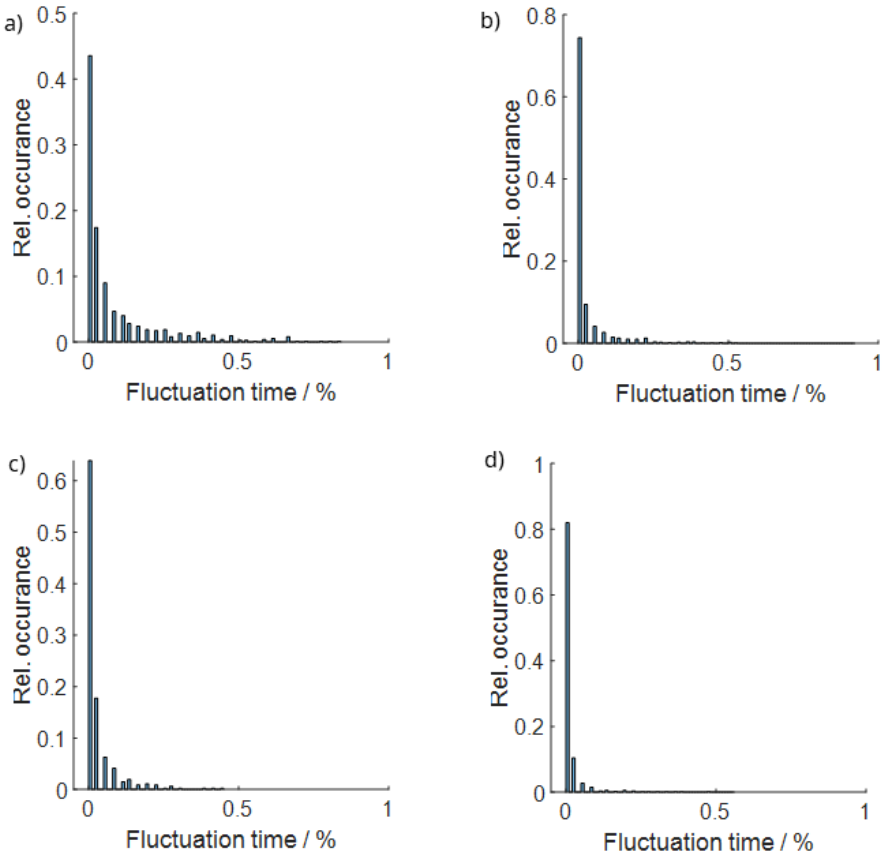

Figure D.2: Histogram of the determined fluctuation percentage. a) Fluctuation time of the time series from an experiment with HSP90. b) Fluctuation time of the particles after the incubation with AMP-PNP

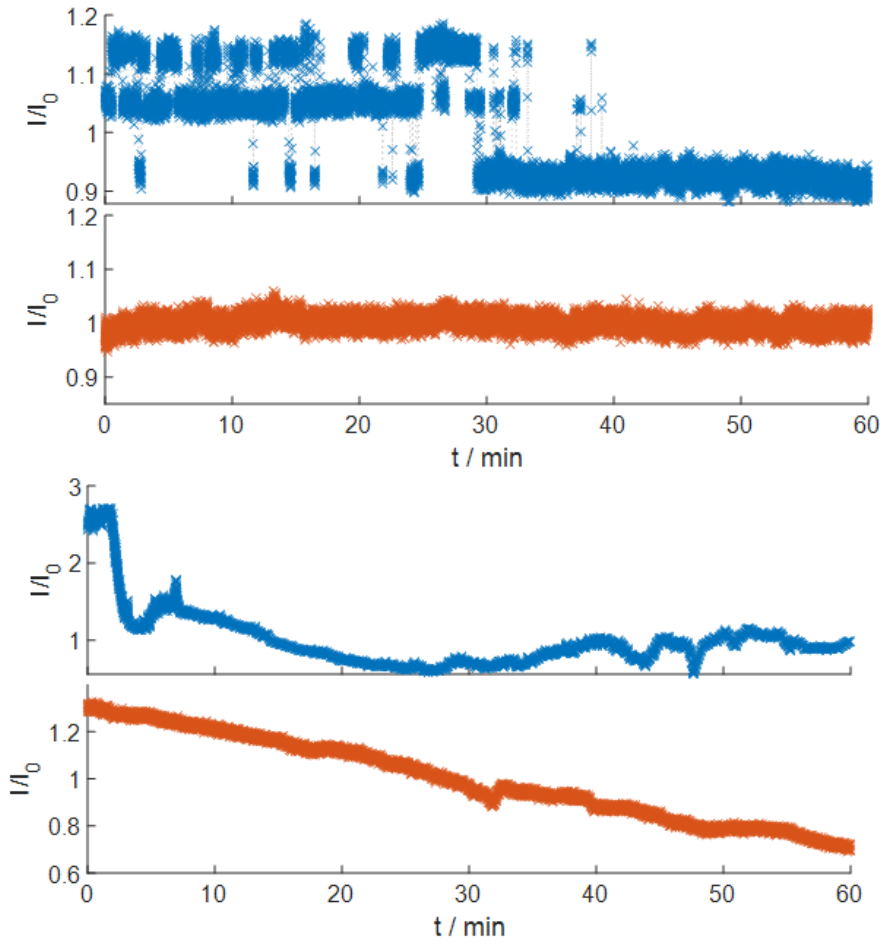

Figure D.3: Example time series from an experiment without HSP90. Time series were recorded with a time resolution of $0\,\mathrm{s}$ for one hour (blue). A time series of one hour was recorded after incubation with AMP-PNP (orange). One time series was falsely identified as showing fluctuation due to strong drift (bottom) and one shows distinct fluctuation between states (top).

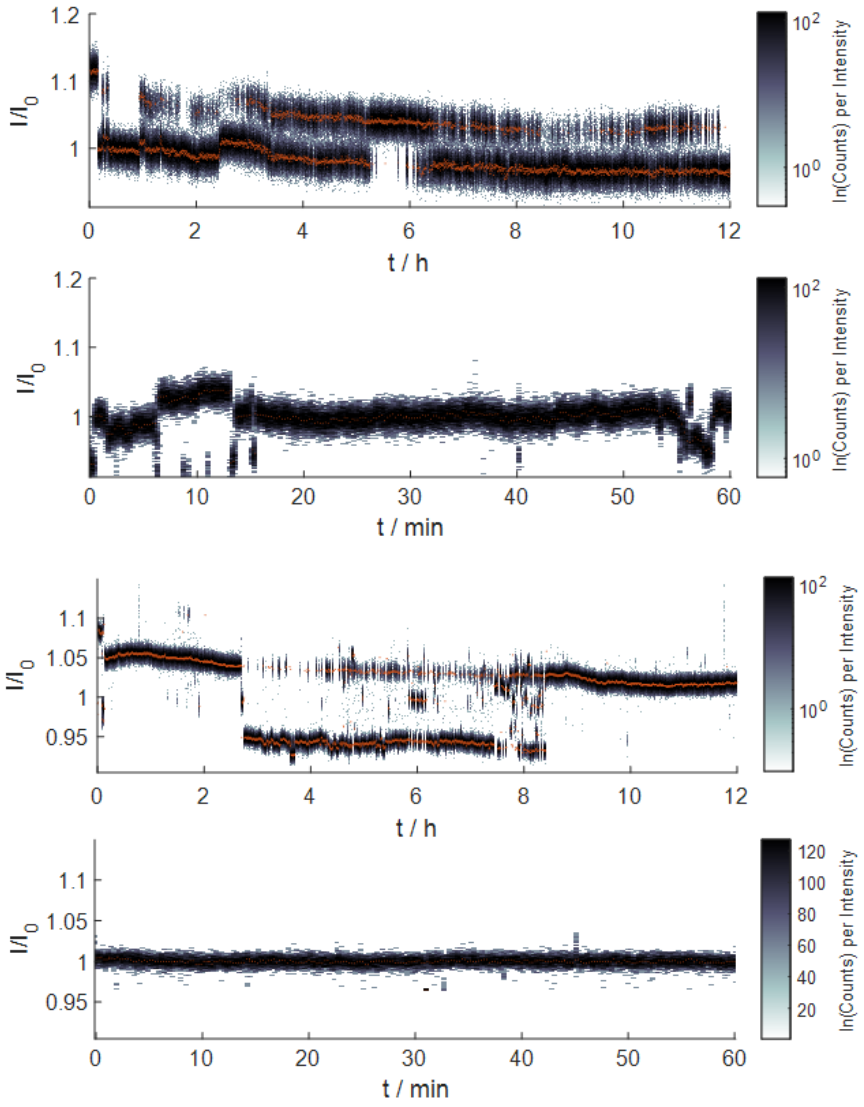

Figure D.4: Additional time series with two and three states of $12\,\mathrm{h}$ duration shown as heatmaps. After the incubation with AMP-PNP the fluctuation between states disappeared (shown below the corresponding time series).

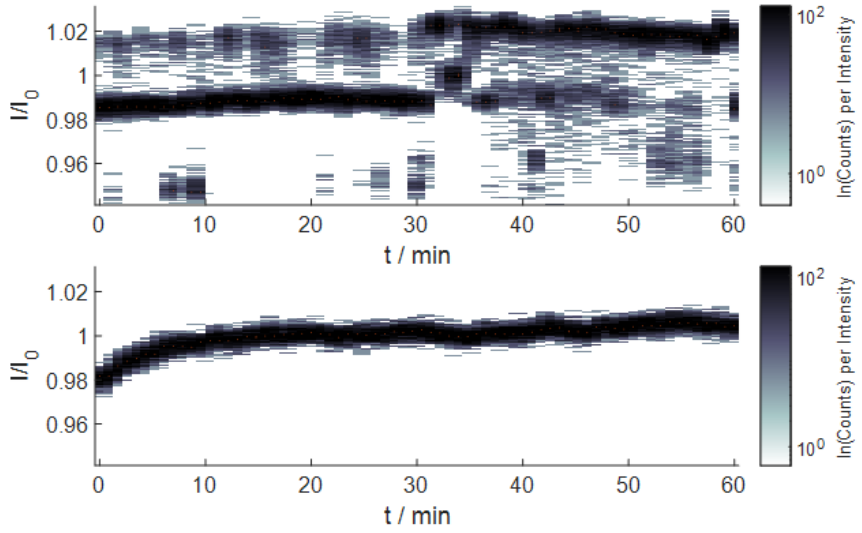

Figure D.5: Time series over one hour with three states (top). Fluctuation stopped after incubation with AMP-PNP (bottom). Both time series are shown as a heatmap.

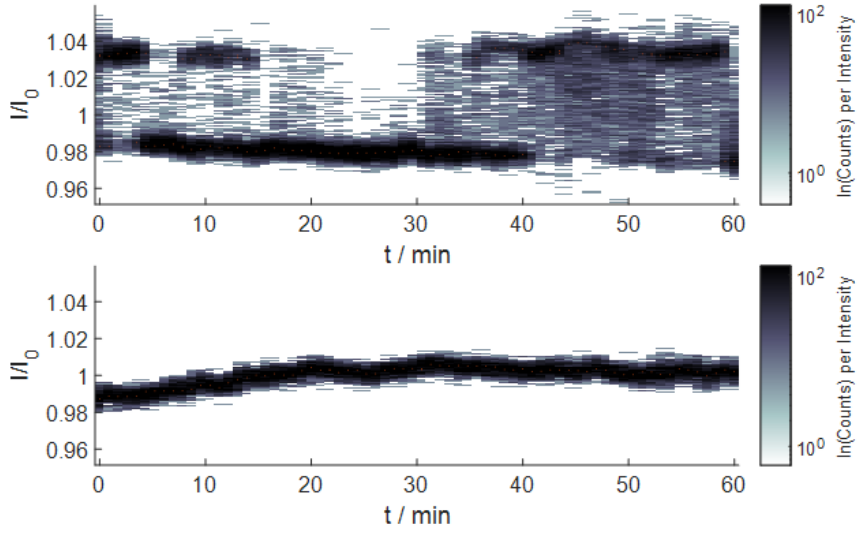

Figure D.6: Time series over one hour with two states (top). Fluctuation stopped after incubation with AMP-PNP (bottom).Both time series are shown as a heatmap.

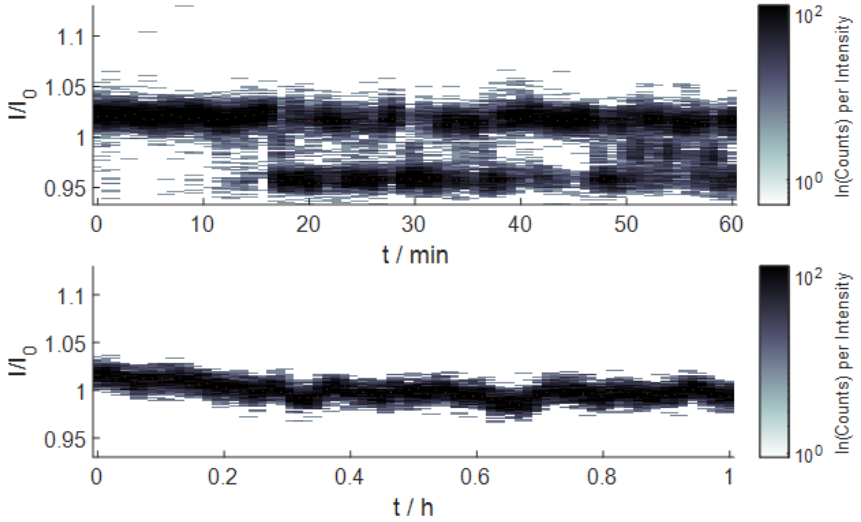

Figure D.7: Time series over one hour with two states (top). Fluctuation stopped after incubation with AMP-PNP (bottom).Both time series are shown as a heatmap.

orientation of the plasmon rulers also plays a role for the singal strength. Additionally I investigated the signal created from a single particles fluctuating against the glass surface (Appendix A). The simulated signal amount to ca. 1.5% change in the scattering intensity which closely matches population of state differences of ca. 2-3%. It is therefore also possible that single particles are bound to the surface by HSP90 and the fluctuation is recorded.

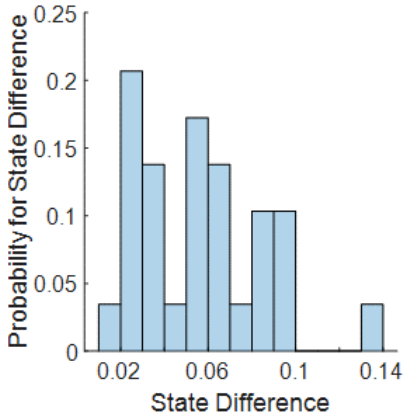

Figure D.8: Histogram of relative intensity changes between states in HSP90 time series.

Appendix E

Software improvements

E.1 Statefinder

There are cases where the statefinder algorithm does not recognize all present states in the time series. For multiple testes minimal stepheights and maximum number of states no match to the data could be found. Figure E.1 shows two examples of time series where the correct number of states was not identified. Those time series were excluded from further evaluation manually.

E.2 Code

The following code was used to generate the heatmaps shown in this thesis.

Listing E.1: Code to generate a Heatmap from a time series.

```
function [slid_hist, sp_x, mploc] = tsheatmap(ts,wl,bn)
%Input variables are the time series ts windowlength wl
    in number of data points and the number of bins for
    the intensity bn. Output are the counts per bin
    slid_hist and the locations of the maxima in the
    histograms of each section sp_x and mploc (x and y).
tsl = length(ts);
if nargin < 3
    bn = 256;
end
if nargin < 2
    wl = 1800;
end
%use global histogram for uniform bins in sliding
    histogram
```

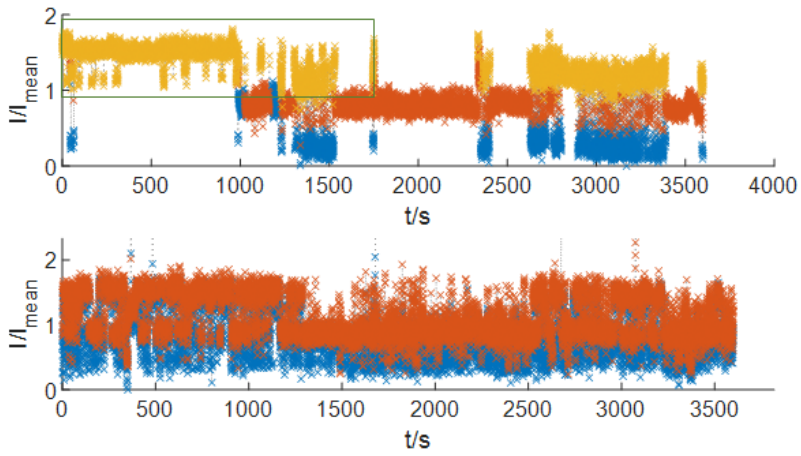

Figure E.1: Statefinder does sometimes not recognize all states. Top: time series has four visible state levels, the statefinder did only allocate three. Green box drawn to for guidance. Bottom: Time series has three visible state levels, but the statefinder only allocated two states to the experimental data. Both time series were normalized to the signal of the nearest non-fluctuating particle and then to its own average.

```
[~, edge] = histcounts(ts, bn);
edge2 = edge+(edge(1)-edge(2))/2;
edge2(end) = [];
sp_x=edge2;
%sliding histogram
stepsize = round(wl/2);
j=0;
%set slidhist to zeros for faster loop
slid_hist=zeros(round((tsl-wl)/stepsize),bn);
for i = 1:stepsize:tsl-wl
    j=j+1;
    slid_hist(j,:) = histcounts(ts(i:i+wl), edge);
%find peaks
[mpks{j},mploc{j}] = findpeaks(spline(edge2,smooth(
    slid_hist(j,:)),sp_x),'MinPeakProminence',10);
end
end
```

Listing E.2: Code plot the generated heatmap.

```
    function plotHeatmap(slid_hist,edge,mlocs,duration)
sl = int8(slid_hist./max(slid_hist(:))*256);
snorm = slid_hist./max(slid_hist(:));
```

```
[timevec, edgevec] = size(slid_hist);
figure()
imagesc(linspace(0,duration ,timevec),edge,sl')
cb = colorbar;
cb.Label.String  = 'ln(Counts) per Intensity (256 bins)';
set(gca,'YDir','normal')
set(gca,'ColorScale','log')
xlabel 'Time / h'
ylabel 'Intensity / abr. U.'
hold on
yvec = 1:edgevec;
xvec = linspace(0,duration,timevec);
for p = 1:timevec
plot(xvec(p),edge(mlocs{p}),'.', 'Color',[0.8500 0.3250
    0.0980] ,'MarkerSize',2)
end
hold off
end
```

Listing E.3: Code of the fluctuaion filter.

```

 function cbSplitHisto (h,~,~,splittime)
 %if not evaluated, do evaluation

    switch nargin % if no time for splits given, trigger
        input
        case 3
             prompt = 'Enter Timewindow for analysis in
                 minutes.';
            dlgtitle = 'Input Timewindow';
            answer = inputsdlg(prompt,dlgtitle);
            if isempty(answer{:})
            splittime = 2; %time for each split in
                minutes
            else
            splittime = str2double(answer);
            end
    end

%select which run to do evaluation for
 %if only one run is loaded default to that run

      runID = h.selRunID();

%get length of split in datapoint
```

```
23      splitlen = round(splittime * 60 * round(1/h.rd{runID
            }.expt),1,'significant');
24      nsplit = round(h.rd{runID}.nt/splitlen);
25     while mod(h.rd{runID}.nt,nsplit)~=0
26         nsplit = nsplit +1;
27     end
28      splitlen = h.rd{runID}.nt/nsplit;
29     w = waitbar(0,'Splitting Timeseries...');
30      for tsidx = h.rd{runID}.np:-1:1
31         if ~h.rd{runID}.yp_ok(tsidx)
32             h.preprocessSignal(runID, tsidx);
33            end
34            rsTS(:,:,tsidx) = reshape(h.rd{runID}.yp.Data(
                  tsidx).s,splitlen,[]);
35            for splitIdx = size(rsTS,2):-1:1
36                %loop over ts chunks to get histogram
37                [count, edge] = histcounts(rsTS(:,splitIdx
                      ,tsidx),'BinMethod', 'sqrt');
38                edge = edge+(edge(1)-edge(2))/2;
39                 edge(end) = [];
40                 %find peaks
41                 h.rd{runID}.split_ts.histcounts{splitIdx,
                       tsidx} = count;
42                 h.rd{runID}.split_ts.bincenters{splitIdx,
                       tsidx} = edge;
43                 [h.rd{runID}.split_ts.mpks{tsidx,splitIdx
                       },h.rd{runID}.split_ts.mploc{tsidx,
                       splitIdx},h.rd{runID}.split_ts.mpwidth
                       {tsidx,splitIdx}, h.rd{runID}.split_ts
                       .mpprom{tsidx,splitIdx}] = findpeaks(
                       smooth(count),edge,'MinPeakProminence'
                       ,10);
44                 h.rd{runID}.split_ts.npks(tsidx,splitIdx)
                        = length(h.rd{runID}.split_ts.mpks{
                       tsidx,splitIdx});
45             end
46      waitbar(1- tsidx /h.rd{runID}.np,w,'Splitting
            Timeseries...');
47     end
48     h.calcQualityFactor(runID);
49     h.calcStepDisance(runID);
50     h.calcSNR(runID);
51     close(w);
52     h.plotStateHistogram(runID);
```

In der Zeit einer Doktorarbeit kann man sich ziemlich alleine fühlen. Viele Frage, wenig Antworten. Unsicherheiten ob die eigenen Ideen klappen. Zweifel ob der eingeschlagene Weg der richtige war. Euch allen bin ich dankbar dass ich nicht alleine gewesen bin und ihr mich mit Rat, Tat und Zeit unterstützt habt.

[redacted], Danke für die vielen Freiheiten, die ich in der Gestaltung meiner Arbeit hatte. Danke für alle Hilfen, insbesondere bei den Vorträgen die ich gehalten hatte. Danke für die angeregten (bis hitzigen) Diskussionen zu meinen Ideen und außerhalb der Wissenschaft.

[redacted] Danke für die Zusammenarbeit und den Austausch bei der Passivierung. Die Gespräche über Studienverlauf, Aufbau von Übungen und Gestaltung der Lehre mit dir haben mir viel Spaß gemacht.

[redacted] Danke für die schöne Zeit die wir zusammen hatten. Angefangen im gemeinsamen Büro bis zu den vielen Diskussionen über Experimente und die Freunschaft die sich daraus entwickelt hat. Vielen Dank für die Zeit die du investiert hat in Erklärungen, Anleitung, Feedback...

[redacted] Danke dass du Teil des Projekts geworden bist. Deine Gedanken und Fähigkeiten im Labor haben so viel zu dem Projekt beigetragen. Sich im letzen Jahr das Büro zu teilen hat mir viel Freude bereitet.

[redacted] Danke die gemeinsame Zeit und Arbeit die du mit in das Projekt gesteckt hast. Deine Ideen und Anmerkungen fand ich in Diskussionen immer sehr hilfreich und wichtig, besonders weil du nicht gefangen in den bekannten Laborabläufen. Der Blick von außen war immer eine Bereicherung. Tausend Dank für die vielen Programmierungn die du für mich übernommen hast.

[redacted] Danke für die ganzen Experimente die du für mich übernommen hast. Danke für die netten Gespräche beim Mittagessen, das gemeinsme Rätseln und die Organisation von so vielen Dingen im Hintergrund.

[redacted] Ein weiser Mann sagte zu mir: "Du wirst nicht fertig. Du hörst einfach auf."... Tja das hat mit dazu beigetragen dass diese Arbeit tatsächlich ein Ende gefunden hat. Danke für deine Ideen, gemeinsames Fluchen und die schönen Abende bei Bier und Wein.

[redacted] Danke für die unzähligen morgendlichen Gerspräche. Danke für die geteilte Freude über Kleinigkeiten im Laboralltag, geteiltes Leid bei gescheiterten Experimente und deine Freundschaft.

[redacted] Thank you for the great excitement you brought towards my project and into group. Your ongoing curiosity to all the "german" events is wonderful and I'm am happy I could share some with you. Thank you for sharing parts of your culture with me and introducing me to "real" indian traditions and food. I am truly grateful for the coincidence that we met and became friends.

[redacted], ein riesiges Danke für die Zeit und Energie die ihr in ein fremdes Projekt investiert habt. Trotz aller Fehlschläge habt ihr euch in meine Arbeit eingebracht und versucht mit eurem Wissen zu helfen.

[redacted] Danke für die vielen Gespräche im Laufe des Projekts. Dein Input, Motivation und Hilfestellungen bei der Passivierung haben mir viel geholfen. Danke dass ich mit deiner Gruppe nach Todtmoos fahren durfte

[redacted] Danke für die Unterschtützung und Erklärungen zur Silanisierung von Glas.

[redacted] Vielen Dank für deine Hilfe mit den NMR Spektren und Ideen zum Nachweis der Reaktionen.

[redacted], vielen Dank dass wir uns von euch das Gerät zu Kontaktwinkelmessung spontan leihen durften.

[redacted] Vielen Dank dass wir euren Plasmacleaner nutzen durften.

[redacted], [redacted]. Nicht alles eurer Ergebnisse kommen in meiner Arbeit vor, trotzdem bin ich froh um jede Erkenntniss die aus euren Arbeiten gewonnen wurde. Danke für euren Einsatz im Labor und in Diskussionen. Ich hatte viel Freude bei der Arbeit mit euch.

[redacted] Vielen Dank für deine Zeit und Interesse an den Details die sonst wirklich wenige Menschen intessieren. Danke für dein Mitgefühl in schweren Zeiten und unvergleichliche Begeisterung für meine Forschung.

E.2. CODE

[redacted] Ihr habt in den letzten Jahren nicht daran gezweifelt dass ich es schaffen werde und wart stolz auf das was ich mache selbst wenn ich es nicht war. Danke!

[redacted] Danke dass du das mit mir durchgestanden hast. Bei allen Zweifeln warst du für mich da und hast mich wieder aufgebaut, hast an mich geglaubt als ich es nicht habe. Du hast die großen Freuden mit mir geteilt, meine Ideen mit mir diskutiert und mir geholfen meine teils wirren Gedanken zu sortieren. Ohne dich hätte ich vieles hiervon vielleicht nicht geschafft.